Title
Integrated Node-Pore Sensing Techniques for Label-Free Single-Cell Measurements

Author
Cotner, Kristen L.

Publication Date
2022

Peer reviewed|Thesis/dissertation

Integrated Node-Pore Sensing Techniques for Label-Free Single-Cell Measurements

by

Kristen Cotner

A dissertation submitted in partial satisfaction of the

requirements for the degree of

Joint Doctor of Philosophy
with University of California, San Francisco

in

Bioengineering

in the

Graduate Division

of the

University of California, Berkeley

Committee in charge:

Professor Lydia Sohn, Chair
Professor Chunlei Liu
Professor Tammy Chang, UCSF

Fall 2022

Integrated Node-Pore Sensing Techniques for Label-Free Single-Cell Measurements

Abstract

Integrated Node-Pore Sensing Techniques for Label-Free Single-Cell Measurements

by

Kristen Cotner

Doctor of Philosophy in Bioengineering

University of California, Berkeley

Professor Lydia Sohn, Chair

Microfluidic devices that can analyze single cells at high throughput are powerful tools in biomedical research, and many such technologies have been developed in recent years. Node-pore sensing (NPS) is one such platform, and NPS devices have been developed that measure a variety of both physical and molecular cell properties. The NPS platform benefits from being inherently label-free, meaning that cells do not need to be tagged with fluorescent or magnetic labels. Additionally, as NPS relies on an entirely electronic measurement, it is a robust system that is relatively low-cost to implement. These factors make NPS an attractive platform for biomedical research because it is accessible and easy to use while enabling multi-parameter single-cell measurements. This platform has already led to several new biological discoveries, although it still has some technical limitations.

This dissertation focuses on characterizing the NPS platform and extending its technical capabilities. First, we present a quantitative study demonstrating the user-friendliness and reliability of our custom NPS data processing software. Second, we describe the theoretical framework and experimental characterization of a novel method to achieve multichannel NPS measurements for the first time. Finally, we introduce a new NPS platform with the unique ability to combine single-cell label-free mechanical and biomolecular measurements. These advancements pave the way toward next-generation, fully integrated NPS devices that can provide new insight into biologically and clinically important questions.

To my parents and my grandparents

Contents

List of Figures

List of Tables

Acknowledgments

Although this dissertation lists only one author on the title page, none of my work would have been possible without the contributions and support of countless others. Thus, I now embark upon the time-honored tradition of trying to express in words the full extent of my gratitude to everyone who helped me reach this milestone.

I've been so fortunate to have Professor Lydia Sohn as my PhD advisor. I am inspired by your passion and drive, and your ideas and feedback have been invaluable at every stage of my research. Thank you for your unflagging positive encouragement, practical advice in the lab, and countless delicious homemade treats. I've learned and grown so much from working with you through all the highs and lows of grad school, and I certainly couldn't have made it through without your unwavering support.

My fellow Sohn Lab members, past and present, have been wonderful colleagues, teammates, mentors, and friends. Their contributions to my research are immeasurable, and it's been a joy and a privilege to work with and learn from this talented group. Thank you to everyone for your great ideas, your help in the lab, your valuable advice, and your ongoing friendship: Dr. Thomas Carey, Dr. Nahyun Cho, Dr. Roberto Falcón-Banchs, Dr. Sewoon Han, Dr. Junghyun Kim, Dr. Molly Kozminsky, Dr. Brian Li, Dr. Olivia Scheideler, Joy Chen, Stephanie Eberly, Sean Kitayama, Andre Lai, Nate Liu, Jessica Ortiz, and Rachel Rex. A special thank-you to the younger students I had the privilege of mentoring in the lab: Matt Bronars, Seraphina Joseph, Ashna Mangla, Alice Mo, and Everett Morton. Finally, I must acknowledge the most excellent cuddle contributions from our lab mascots, Mashi, Taco, and Bodie!

Of course, the scientific community that contributed to my graduate research extends beyond the Sohn Lab. I have been fortunate to work with outstanding collaborators from other labs both within and outside of Berkeley, including Professor Miki Lustig, Alan Dong, Professor Mark LaBarge, Dr. Stefan Hinz, Professor Grace O'Connell, Emily Lindberg, and Ellen van Rooij. Much of the work in this dissertation would not have been possible without their insights, expertise, and partnership. Additionally, the members of my qualifying exam committee and thesis committee provided invaluable guidance and feedback throughout my research: Professor Steve Conolly, Professor Aaron Streets, Professor George Johnson, Professor Bonnie Joe, Professor Chunlei Liu, and Professor Tammy Chang. Finally, I would like to thank the National Science Foundation, the National Institutes of Health, and the Siebel Scholars Foundation for providing funding that supported my graduate work.

The community within the Berkeley–UCSF Bioengineering graduate program is truly special and is what drew me to join this program in the first place. To the countless older students who passed on their advice and wisdom at every stage of grad school, I cannot thank you enough for helping me with everything from writing fellowship essays and choosing rotation labs in my first year, all the way through preparing for quals and even finding a job. Moreover, I've met life-long friends here, and I'll always treasure the memories we made—as well as the slightly embarrassing skit videos! Special shout-outs to Cohorts 2016 and 2015, my fellow Retreat Committee members, and the BioMEMS chat group. An additional big

thank-you to the program admins, Kristin, Sarah-Jane, Rocío, and Victoria, who helped us navigate the complications of our joint program and always provided good advice and fun conversations.

Thank you to my accountabilibuddies, Laura, Jaimie, Victoria, McDavid, Jimmy, and both Rachels, for helping me stay on-track with work and life during the pandemic. Thank you to my college friends, especially the C5&Friends Discord and the Course 20 Derp Squad, for keeping me well-informed about all the latest coding memes and providing much-needed reminders that there is life outside of grad school! To my fellow Masked Musicians, QinQin, Claire, and Jacqie, I am so grateful to you for regularly filling my house with lovely music and wonderful company. To my many hiking, camping, skiing, and climbing buddies—but especially to master trip-planner Zhang—thank you so much for making me go outside and get some vitamin D after too many hours in lab!

I've been blessed with unusually excellent housemates throughout grad school, in our humble abode known as "New New House" or "New House West." I'll never forget the delicious food, the late-night conversations, and the many entertaining adventures—including our Bay to Breakers run in superhero costumes, that time we dog-napped a pair of corgis (with the owner's permission!), and our ultimate triumph at Bobby G's trivia night. To all the official and honorary residents who shared this house with me, thanks for turning it into a home: Kathryn, David, Laura, Will, Aaron, Ana, Sophie, Tobias, Dan, Sami, Marie, Marc, Krista, Zhang, Ryan, Sean, and Stephanie. And of course, no one could ask for more steadfast and loving four-legged housemates than Aurora, Midas, and Dexter! Finally, an extra shout-out to my housemate Laura, who has also been my friend, adventure buddy, and partner in crime for 11 years. Thank you for bringing joy and laughter to every situation; grad school would not have been the same without you.

To Bennett, who has been there for me through thick and thin over the last five years—thank you for your kindness, patience, encouragement, and thoughtful advice. No matter what unexpected challenges we've encountered, you've been a truly remarkable source of support throughout it all. Thank you for everything, and for continuing to put up with me!

Finally, I wouldn't be here without my family. My grandparents, Mimi, Papa, Mamaw, and Papaw, were an important part of my life and raised wonderful, loving families that I'm lucky to be a part of. To Mom and Dad, thank you for raising me with the unconditional love and support that every child deserves. I am so grateful to you for instilling the value of education and providing me with the resources I needed to succeed, while allowing me to choose my own path. Most importantly, thank you for teaching me the importance of family, friendship, and kindness.

Statement of Co-Authorship & Prior Publication

This dissertation contains content adapted with permission from the following publications (as noted at the start of each relevant chapter):

T. R. Carey*, K. L. Cotner*, B. Li*, and L. L. Sohn, "Developments in label-free microfluidic methods for single-cell analysis and sorting", *Wiley Interdisciplinary Reviews: Nanomedicine and Nanobiotechnology*, no. March, e1529, 2018, ISSN: 19390041. DOI: 10.1002/wnan.1529. [Online]. Available: https://onlinelibrary.wiley.com/doi/full/10.1002/wnan.1529, *Equal contribution. [1]

B. Li*, K. L. Cotner*, N. K. Liu, S. Hinz, M. A. LaBarge, and L. L. Sohn, "Evaluating sources of technical variability in the mechano-node-pore sensing pipeline and their effect on the reproducibility of single-cell mechanical phenotyping", *PLOS ONE*, vol. 16, A. Han, Ed., e0258982, 10 Oct. 2021, ISSN: 1932-6203. DOI: 10.1371/JOURNAL.PONE.0258982. [Online]. Available: https://journals.plos.org/plosone/article?id=10.1371/journal.pone.0258982, *Equal contribution. [2]

Chapter 1

Introduction

A core concept in the development of modern biotechnologies is the ability to capture the full spectrum of heterogeneity present in biological samples. In both research and clinical laboratory environments, it is often not sufficient to take a bulk measurement of millions of cells. Not only are there dozens of cell types within the human body, but there are often a wide variety of states possible even within the same cell type. Moreover, it is often precisely this heterogeneity that gives rise to a biological phenomenon of interest—for example, when just one cell develops a cancerous mutation. For these reasons, new biotechnology platforms are most often focused on *single-cell* analysis, or the ability to perform a separate measurement on every cell within a sample.

The field of microfluidics—which focuses on creating and applying fluidic devices with micron-scale features—has enabled significant advances in single-cell measurement technologies in recent years. Microfluidic technologies enable researchers to create chips with small microchannels, through which hundreds or thousands of cells flow one at a time. This level of control allows very precise measurements to be accomplished at high throughput and has led to a plethora of new single-cell analysis platforms in the past two decades. Among the many single-cell microfluidic analysis strategies, electrical sensors are especially promising due to their versatility, robustness, and relatively low cost. Electronically integrated microfluidic devices have been used to screen and analyze single cells for a wide range of biomedical and clinical applications, including rapid blood counts, HIV and parasite detection, and point-of-care diagnostics.

In this dissertation, I focus on a particular microfluidic platform called node-pore sensing (NPS). This is a single-cell analysis technology based on a simple electrical measurement that benefits from the high throughput of microfluidics and the high accessibility of electronic sensing methods. This body of work is primarily concerned with characterizing and expanding the NPS platform to enable new capabilities that could lead to future discoveries.

- In Chapter 2, I will provide context for this dissertation by reviewing the state of the field in single-cell, label-free sensing technologies. I will highlight the major work in

recent years, provide a perspective on the pros and cons of each method, and identify promising areas for future development.

- In Chapter 3, I will focus on a core technology developed in the Sohn Lab called mechano-node-pore sensing (mechano-NPS), which measures the mechanical properties of cells. I will describe the motivation behind this type of measurement, known as mechanical phenotyping, and I will discuss areas where mechano-NPS has led to new insights in biology and cancer. I will then review the theoretical principles governing mechano-NPS and provide general methods for mechano-NPS device fabrication, data collection, and data analysis. Finally, I will present the results of a systematic study demonstrating that while the data processing software for mechano-NPS requires some user input and training, results obtained with this software are highly consistent and reproducible between users, even for novices.

- In Chapter 4, I will describe a novel method for improved throughput and versatility of the NPS platform that is based on, for the first time, simultaneous *multichannel* measurements. I will discuss the motivation for introducing multichannel capabilities and review the theory behind this novel method. I will provide a mathematical model for how this system behaves as it simultaneously measures cells in several parallel channels, and I will utilize computational simulation to evaluate the model's predictions.

- Having established the theoretical framework for this new multichannel NPS technology, I will demonstrate its experimental implementation in Chapter 5. I will present three new multichannel device designs based on this concept and demonstrate proof-of-concept results from each. I will describe the computational data analysis platform we developed that teases apart the signals from the separate channels and automatically extracts data from measured cells. Finally, I will present a quantitative study of the tradeoff between increasing numbers of channels and system performance.

- In Chapter 6, I will describe progress toward combining mechanical phenotyping with biomolecular screening in a new, integrated NPS platform. I will first review the motivation for developing this technology and provide context by describing prior work. I will then present an overview of the concepts behind our new platform and the underlying technologies we apply. Next, I will provide methods and preliminary results for a proof-of-concept integrated device design. Finally, I will discuss challenges and next steps in this project.

- I will conclude in Chapter 7 by reviewing the work presented in this dissertation and describing how we plan to apply these developments in NPS technology toward current and future projects.

In summary, this dissertation focuses on emerging technologies for label-free single-cell analysis with the NPS platform. We have conducted a quantitative user study of the mechano-NPS data processing software, we have established and characterized a novel method that enables multichannel NPS measurements for the first time, and we have developed a new NPS platform that combines mechanical and biomolecular measurements. These advancements will drive further technological development to extend NPS capabilities even further, creating more powerful single-cell analysis tools for biomedical research.

Chapter 2

Motivation & Prior Work

This chapter is adapted with permission in part from:

> T. R. Carey*, K. L. Cotner*, B. Li*, and L. L. Sohn, "Developments in label-free microfluidic methods for single-cell analysis and sorting", *Wiley Interdisciplinary Reviews: Nanomedicine and Nanobiotechnology*, no. March, e1529, 2018, ISSN: 19390041. DOI: 10.1002/wnan.1529. [Online]. Available: https://onlinelibrary.wiley.com/doi/full/10.1002/wnan.1529, *Equal contribution. [1]

In this chapter, we review microfluidics advances in the last two decades that have resulted in the development of many new tools for characterizing single cells. We discuss the rationale for analyzing biological samples at the single-cell level and the advantages of label-free platforms over those that require exogenous labels. We also review some of the most promising technologies of this type, including electronic sensors (*e.g.*, Coulter counters and electrical impedance cytometry) and devices that perform deformation analysis (*e.g.*, optical traps and deformation cytometry). This chapter serves to describe the state of the field in single-cell, label-free microfluidic analysis and establishes the foundation for the rest of the work in this dissertation.

2.1 Introduction

Tools for cell characterization are indispensable in the life sciences and in medicine, as they enable rapid identification of desired subpopulations and critical monitoring for clinical diagnostics. Recently, single-cell analysis has gained much attention, as such analysis could potentially transform personalized medicine. Knowledge of the heterogeneity of a patient's solid tumor at the single-cell level could, for instance, enable therapies that target multiple cell subtypes [3], thereby improving survival rates. Identifying rare circulating tumor cells in patient blood could determine prognosis and efficacy of treatment [4]. Current methods for single-cell analysis include flow cytometry and magnetic-activated cell sorting. However, both require (a) lengthy, resource-intensive sample preparation, leading to the potential loss

of key cells; (b) cell labeling, for which multiplexing is limited by spectral overlap of labels; and (c) a large population of cells. In the case of flow cytometry, dedicated technical support is often needed for instrument operation, and the instrument itself is sufficiently expensive to limit usage to core laboratories.

Beyond the difficulties discussed above, label-based methods for cell analysis may be hindered by even more fundamental issues. The use of labels inherently requires knowledge of the property or population that is being measured. It is impossible to search for new, undefined cell populations using only labels for known biomarkers. Perhaps an even more important consideration is that the biochemical process of a label binding a surface marker may alter the state of the cell, activating specific pathways. As discussed by [5], label-based tests in early drug development may be one of the contributing factors that lead to the high rates of failure in later stages.

Label-free microfluidic techniques, which do not require exogenous or endogenous labels, offer an alternative approach to single-cell analysis. These techniques—highlighted in Fig. 2.1—usually fall under two broad areas: electrical or optical. While the throughput of many microfluidic screening technologies is not yet competitive with that of flow cytometry, their promise in identifying specific cells or small subpopulations of cells (*i.e.*, circulating tumor cells or stem cells) makes them highly attractive to the biomedical research and clinical diagnostics communities. Below, we highlight just a few exciting label-free techniques and their biomedical and clinical applications.

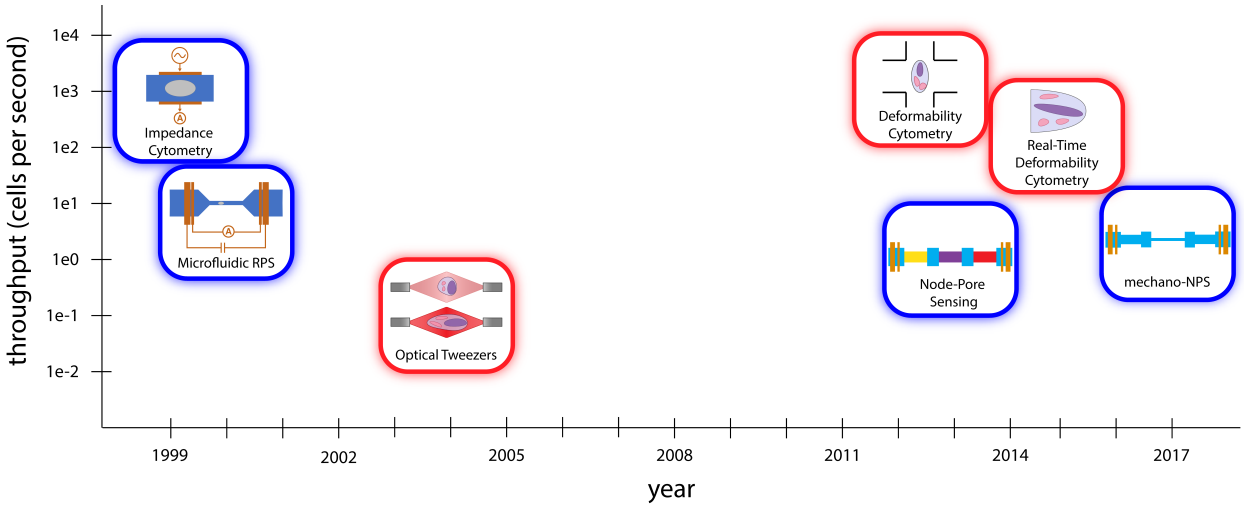

Figure 2.1: An overview of common microfluidic platforms for single-cell analysis developed over the last two decades. The methods shown are broadly categorized as electrical (blue) or optical (red). While some methods offer higher throughputs, other methods may provide more granular information about cells. The throughput values indicated are approximate and correspond to the first demonstration of that technology; current implementations of older technologies may have higher throughput values than those shown here. Adapted with permission from [1].

2.2 Electrical Analysis

Electronic sensors are an attractive choice for cell screening given the wide array of inexpensive, robust off-the-shelf electronic parts that are available. The cell's dielectric properties reflect the biophysical parameters of the membrane and cytoplasm, and electronic sensors are easily integrated into microfluidic systems to measure these properties. These types of systems have been used to assess membrane morphology, ion channel status, intracellular ion flow, and nuclear size, and subsequently, to identify physiological differences, track pathological changes, and discriminate cell subpopulations [6–8]. For example, systems that measure cellular dielectric properties have been used to detect parasite-infected red blood cells [8], distinguish tumor cells from mononuclear blood cells [9–11], and track the metastatic progression of tumor cells [12]. In this section, we focus on a few general types of impedance-based electronic sensors in development.

2.2.1 Resistive-Pulse Sensing

Resistive-pulse sensing (RPS), or the Coulter principle [13], is one of the oldest methods for automated cell counting and analysis. RPS is still the most widely used method for particle counting and remains the industry standard for complete blood counts (CBCs). In traditional Coulter counters, particles pass through an aperture in the presence of a constant applied voltage. As a particle transits the aperture, it partially blocks the current flow. This causes a transient current drop (*i.e.*, a current pulse) whose magnitude corresponds to the size of the particle and whose duration indicates the transit time across the aperture. Microfluidic implementations of RPS, in which particles transit a microchannel instead of an aperture (Fig. 2.2A), were first successfully demonstrated in the early 2000s using not only standard micromachining but also soft lithography [14]. These devices have been shown to be a robust platform for counting specific subpopulations in blood—from circulating tumor cells to HIV particles [15,16].

As recent advances have demonstrated, RPS can also be used to probe other cellular properties beyond size. Balakrishnan *et al.* [17] used a novel method, node-pore sensing (NPS), to screen for multiple cell surface markers (Fig. 2.2C). The sensing channel was coated with antibodies, and cells expressing surface markers that could specifically interact with these antibodies traversed the channel more slowly. To allow screening for multiple surface markers, the main microfluidic channel was divided into segments separated by wider regions called nodes. As the current density was greater in the segments than in the nodes, the current pulse was modulated, facilitating measurement of the cell's transit times through each individual segment. Each segment was coated with a different antibody, and at least one segment was coated with an isotype control. Balakrishnan *et al.* [17] demonstrated that this NPS device could be used to screen for five surface markers simultaneously, and in turn, identify leukemic blast subpopulations found in the bone marrow of acute myeloid leukemia patients.

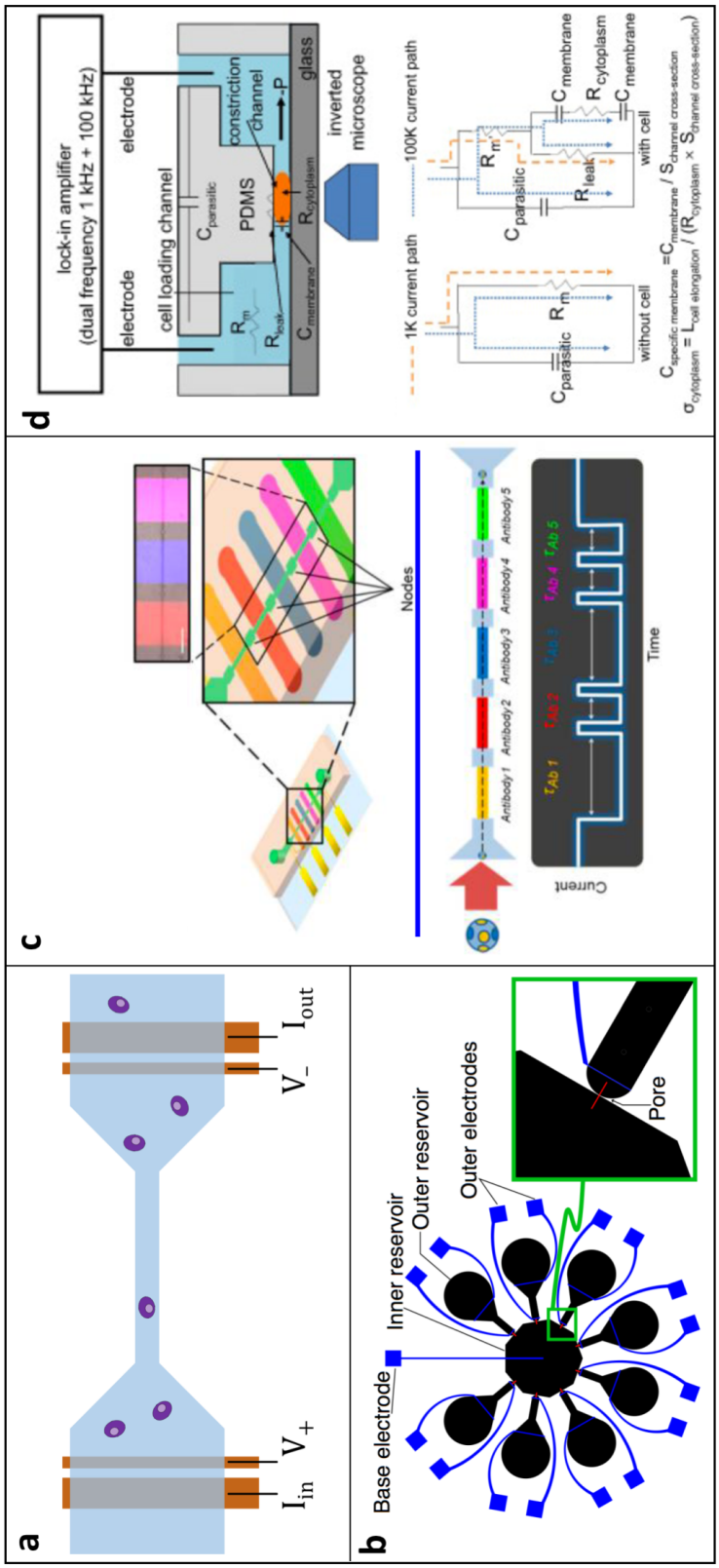

Figure 2.2: Examples of single-cell microfluidic devices based on electrical sensing. Reprinted with permission from [1]. (A) Typical implementation of microfluidic RPS. A fluidic channel (blue), typically a polydimethylsiloxane (PDMS) mold, is bonded to a substrate containing microfabricated electrodes (orange). A voltage is applied across the channel while the current is monitored. A cell's presence in the channel causes a drop in measured current. (B) Example of a multichannel RPS design using eight detection channels to improve throughput by multiplexing. Reprinted with permission from [14]. (C) Node-pore sensing (NPS), a variation of RPS, is used to measure five surface markers in one channel. Each section is functionalized with an antibody, and cells expressing the corresponding surface marker traverse that section more slowly. Adapted with permission from [17] (https://pubs.acs.org/doi/full/10.1021/ac504613b). Further permissions related to the material excerpted should be directed to the American Chemical Society. (D) Schematic and electrical model of a constriction channel design for microfluidic electrical impedance cytometry. Cells flow through the constriction channel while impedance and elongation are measured continuously. Two-frequency data at 1 kHz and 100 kHz allow calculation of specific membrane capacitance and cytoplasm conductivity. Adapted with permission from [18]; see [19].

More recently, a related technique called mechano-NPS was developed to measure the mechanical properties of cells. Mechano-NPS introduces a contraction segment whose width is much smaller than the diameter of a cell [20]. By analyzing the cell volume and transit time through the contraction segment, mechano-NPS can characterize cellular deformability, resistance to deformation, and recovery. Kim *et al.* showed that mechano-NPS could discriminate between malignant and nonmalignant breast and lung epithelial cells, as well as identify differences among pre- and postmenopausal primary human mammary epithelial cells.

Although microfluidic RPS devices characterize important cellular information, they do face tradeoffs in throughput, signal–noise ratio (SNR), and dynamic range. A common strategy to increase throughput without sacrificing SNR is to design a multiplexed RPS device with multiple measurement channels, as first described by Saleh [14] (Fig. 2.2B). A variety of devices based on this concept have been developed [21–23], but they require additional fabricated electrodes for each channel and are thus limited in scalability. Alternatively, phase-shift keying, or encoding data using changes in channel width, may be employed to improve performance. For example, specifically encoded channel geometries, coupled with signal processing strategies in postprocessing, can dramatically improve SNR and dynamic range while also allowing higher throughput by resolving coincidence events [24–26]. Optimal performance may be achieved by combining multiple strategies, such as utilizing specific NPS channel encoding [25,26] to enable coincidence detection while also incorporating code division multiplexing for multichannel design [27].

2.2.2 Cellular Impedance Analysis

A natural extension of the Coulter principle is to apply an alternating current (AC) signal to extract cellular capacitance. This concept was first demonstrated at the single-cell level by Sohn *et al.* [28], who designed a polydimethylsiloxane (PDMS) microfluidic device that could measure the DNA content of single cells based on total capacitance. Many specific cellular properties can be extracted by varying the frequency of the excitation signal: applying low-frequency signals ($<$1 MHz) yields information about cell size, while intermediate frequencies ($\sim$1–20 MHz) enable characterization of membrane properties such as capacitance, polarization, and ion-channel activity. In the high-frequency regime ($\sim$ GHz), subcellular structures such as cytoplasm and vacuoles may be characterized [29,30]. Impedance analysis can be implemented with the same standard microfabrication techniques as RPS, and its ability to characterize a wide range of cell properties enables its use for a variety of biological applications.

Techniques that measure the impedance response of cells at two or more frequencies may be called electrical impedance cytometry (EIC) or electrical impedance spectroscopy (EIS). Because papers in the literature do not use consistent terminology in the distinction between EIC and EIS, we will treat these terms as interchangeable. EIC/EIS can be used in conjunction with cell trapping and immobilization techniques to monitor cellular changes over time. EIC/EIS devices have been used to monitor cell viability, size, cell cycle state, membrane

properties, nuclear division, and cytokinesis [9–11,15] at the single-cell level. Another class of EIC/EIS techniques characterizes many cells as they flow through a microchannel. These devices have been applied to a variety of applications, including cancer detection and monitoring [11,12], blood cell classification [16,31–33], stem-cell differentiation [34], and parasite diagnosis [35,36].

Technological development continues to improve the capabilities of microfluidic EIC/EIS. For example, the constriction channel design for in-flow impedance analysis improves the sensitivity by ensuring a tight contact between the cells and electrodes (Fig. 2.2D) [11,12]. However, the throughput of this technique is still limited to ∼1 cell/s [18]. Haandbæk *et al.* [37] developed a resonator-enhanced EIC/EIS microchip that characterizes cells in flow at higher throughput (∼100 cells/s) while maintaining high sensitivity. The same group demonstrated another device that was able to analyze cells at very high frequencies (up to 500 MHz), which enabled the characterization of small subcellular structures such as organelles [38]. Sun *et al.* [39] developed the maximum length sequence (MLS) approach to EIC/EIS to achieve quasi-real-time impedance characterization across a spectrum of frequencies simultaneously. In this technique, cells are exposed to a pseudorandom white noise signal, which is composed of many frequencies mixed together. The MLS device could thus simultaneously probe the impedance response of single cells at 512 distinct frequencies in a window of ∼1 ms.

2.2.3 Outlook: Electrical Analysis

Electrical interfaces continue to be popular in microfluidic devices because of their robustness and ease of construction. Electrical properties of cells are tied to many important biophysical characteristics and are easily interrogated with electronic sensors that are compatible with microfluidic platforms. Many commercial technologies utilizing the techniques discussed in this section are already on the market, demonstrating that electrical devices for cellular analysis, in general, have great potential for commercialization. For example, the Millipore Scepter is a handheld tool that employs the Coulter principle for automated cell counting (Millipore Sigma, Burlington, MA), and Amphasys and xCELLigence both produce systems that employ impedance analysis for cell characterization and monitoring, respectively (ACEA Biosciences, San Diego, CA; Amphasys, Lucerne, Switzerland).

2.3 Optical Analysis of Cell Deformation

The visual observation of cells with a microscope has been advancing cell biology since van Leeuwenhoek's work in the 17th century. Today, imaging of single cells typically requires the use of a fluorescent label to highlight certain features, both intracellularly and extracellularly. Here, we discuss the use of label-free imaging for mechanical phenotyping, *i.e.*, measuring a cell's response to an applied force. Mechanical phenotyping can be a powerful parameter for diagnosing cancers where traditional biomarkers fall short. For example, in triple-negative breast cancer, the usual prognostic biomarkers are absent, making it difficult to choose an

effective treatment option without further extensive testing [40,41]. However, malignant cells from breast and bladder tissue have been shown to be less stiff than their healthy counterparts. These discoveries suggest that mechanical phenotyping might be a critical consideration in diagnosing subtypes of cancers and guiding clinical decision-making [42,43].

Until the 2000s, the mechanical properties of cells were difficult or extremely time-consuming to measure. Techniques such as micropipette aspiration and atomic force microscopy (AFM) were groundbreaking when they were first introduced, and although still used as gold standards, they are rapidly losing ground to higher-throughput assays [44,45]. Today, single-cell mechanical testing takes place in microfluidic devices that apply stress to individual cells and measure their response. In the devices discussed here, cells are imaged before and after the application of a controlled force to estimate their deformability.

2.3.1 Deformation Using Optical Traps

The optical stretcher was one of the first devices to use optical traps for mechanical testing of cells. Optical stretchers use two divergent laser beams pointed toward each other such that they intersect in the middle of a microchannel (Fig. 2.3A) [43,46]. Cells flow through the channel, perpendicular to the two beams, and are stably trapped at the midpoint between the two laser sources, which are tuned to a wavelength of 1064 nm to minimize cell damage. The photons colliding with the cell impart momentum to it, generating an appreciable net force. In the 1–10 mW range, this force anchors cells against the flow [43]. As the power increases up to 1 W, the two opposite ends of the cell are pushed away from the cell's center with a force around 200–500 pN, stretching the cell laterally (Fig. 2.3A) [43]. The stress applied by the laser beams deforms the cell into an ellipsoid, and the strain is measured by analyzing images of the cell captured with a bright-field microscope. Optical trapping was used in early studies to show that malignant breast cancer cells were more deformable than nonmalignant ones—an important finding that demonstrated the diagnostic potential of mechanical phenotyping [43,46].

While optical stretchers trap cells in the middle of a microchannel, Kolb *et al.* [49] aligned lasers to trap cells slightly off-center in a technique they called optofluidic rotation. Because cells are trapped off-center, the flow (1 nL/s) continuously applies a torque to one end of the cell, causing it to rotate at up to 15 rpm (Fig. 2.3B). By imaging cells with a bright-field or phase contrast microscope throughout a full rotation, one can visualize the cells' tomography and the position of intracellular structures in three dimensions (3D). Since optical traps can perform both optical stretching and optofluidic rotation, they have great potential for studying the tomography and 3D structures of cells undergoing deformation in just a few seconds. Because a cell is not a homogeneous material, and the applied forces are not isotropic, 3D spatial information might improve the measurement of anisotropic mechanical properties of cells. As many cells have a degree of spatial polarity, efforts to understand cell anisotropy might help refine mechanical phenotyping by including or controlling for differences in spatial directions.

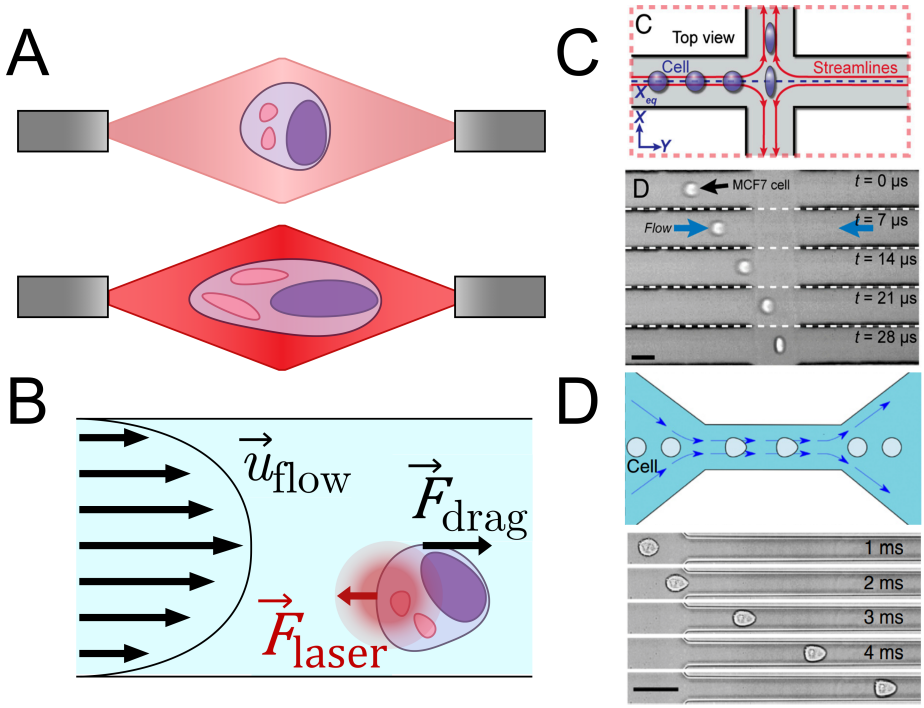

Figure 2.3: Examples of single-cell microfluidic devices based on optical analysis of cell deformation. Reprinted with permission from [1]. (A) Schematic of a cell deformed in a dual-beam optical trap. At low laser power (top), the cell is simply trapped. At higher laser power (bottom), photons colliding with the cell provide enough momentum to physically stretch the cell. (B) Free-body diagram describing optofluidic rotation. A dual-beam optical trap immobilizes a cell at a position offset from the center of the microchannel. The velocity profile applies a shear stress to one side of the cell, causing the cell to rotate around the axis of the laser beams. (C) Schematic of a deformability cytometry stretching chamber (top) and time-lapse of a cell in such a chamber (bottom) [47]. Cells enter an intersection of two high-speed flows from the left and right, and they are deformed and imaged before exiting through the outlets at the top and bottom. Adapted with permission from [47]. (D) Schematic of a real-time deformability cytometry constriction channel (top) and time-lapse of a cell in such a channel (bottom) [48]. Cells enter the narrow channel at high speed, where the shear rate is high enough to deform the cell into a bullet-like shape. Adapted with permission from [48].

A similar, but notable, class of microfluidic devices relies on optical chromatography [50]. This method exploits opposing hydrodynamic and optical forces to deform cells in "optical channels" and has been used to study erythrocyte elasticity [51], among other cellular processes and properties [52].

2.3.2 Hydrodynamic Deformation

Not all microfluidic mechanical phenotyping is performed with optical traps. In other devices, the flow itself can apply stresses to cells. In a technique known as deformability cytometry (DC), cells are accelerated into a stretching chamber, where the high-velocity flows (∼10–20 µL/s) from two different microchannels meet (Fig. 2.3C) [53]. The opposing fluidic flow deforms a cell into an ellipsoid before pushing it toward an outlet. Gossett *et al.* demonstrated the ability of DC to differentiate among populations of normal and stimulated peripheral blood mononuclear cells and granulocytes [53]. Traditionally, discriminating between these phenotypes required immunostaining for clusters of differentiation or enzyme-linked immunosorbent assays (ELISAs) to assay cytokine secretion. DC is able to quickly interrogate thousands of cells and measure distinguishable differences in population deformability.

While DC can analyze thousands of cells per second, it is difficult to capture images of cells moving through the device, as they persist in the stretching chamber for only a few microseconds [53]. As a result, a camera used for DC must be capable of acquiring images at over 100,000 frames per second (FPS); such cameras are often extremely expensive and require high-speed and high-density storage solutions to store and analyze data.

This particular drawback inspired Otto *et al.* [48] to improve on the designs of Gossett *et al.* and develop real-time deformability cytometry (RT-DC). In RT-DC, cells are deformed while in transit through a microchannel only slightly larger than the cell. The flow velocity is high enough such that the shear stress near the channel walls bends the cells into the shape of the flow velocity profile, which resembles a bullet (Fig. 2.3D) [54]. As in DC, cells in RT-DC are imaged with a high-speed camera, but because the flow velocity is considerably slower than in DC, a frame rate of around 1000 FPS is adequate. Cameras capable of imaging at this speed are more readily available than those needed for DC. The lower frame rate also means RT-DC generates much smaller datasets for comparable experiments, and as a result, deformation data can be analyzed in real time.

Like its predecessor, RT-DC has also been used to discriminate between leukocyte populations, a critical aspect of hematology [48]. Another application of interest is the isolation of skeletal stem cells (SSCs) from bone marrow, where the SSC marker Stro-1 lacks the specificity needed to isolate SSCs with high purity [55]. Xavier *et al.* used RT-DC to discriminate between myeloid leukocytes and SSCs by demonstrating that SSCs were dramatically larger and stiffer [48,55]. Thus, RT-DC can be used to identify and isolate different cell populations in a single sample based on deformability. This is particularly attractive if information from traditional biomarkers is difficult to acquire or inadequate for precise discrimination.

2.3.3 Outlook: Optical Analysis of Cell Deformation

Methods for performing mechanical testing on single cells have existed for years; AFM, for example, was introduced more than 30 years ago [44]. While this technique can acquire a single force curve in a few seconds, it can take an hour to generate a force map of an entire cell. By contrast, the microfluidics-based techniques discussed here enable much higher throughput. Optical stretchers, the first of these techniques, are capable of performing a whole-cell mechanical test in just a few seconds [56]. Although Lincoln *et al.* suggest that optical stretchers could be incorporated into flow cytometers to allow for deformability-based flow cytometry, modern flow cytometers operate at much faster rates, often analyzing thousands of cells per second [43]. Hydrodynamic methods such as DC or RT-DC would be more appropriate for incorporating deformability measurements into flow cytometry.

Although the flow velocity of RT-DC is considerably slower than that of DC, it can still analyze hundreds of cells per second [48]. This rate overlaps with the lower end of modern flow cytometers' range of operating speeds. The large volume of high-speed video generated by DC necessitates offline processing and would thus be difficult to integrate with flow cytometry. RT-DC, however, can acquire and display deformability data on a single consumer-grade computer in real time. For this reason, RT-DC would appear to be the best candidate for deformability-based flow cytometry and is primed for commercialization.

Nevertheless, older technologies have been commercialized already. LumaCyte's Radiance takes advantage of optical chromatography to analyze and sort single cells based on their response to a laser force (Lumacyte, Charlottesville, VA). Cytovale seeks to use DC to diagnose sepsis at an early stage by analyzing activated neutrophils (Cytovale, San Francisco, CA). We can expect additional commercial platforms in the future as RT-DC matures and new techniques are invented.

2.4 Conclusions

For analyzing single cells, microfluidic devices offer numerous advantages over traditional benchtop assays. The most obvious benefits, such as rapid prototyping and high assay throughput, allow users to accomplish more in less time. An equally powerful advantage is the ease of integrating microfluidic devices with other transducers and sensors, such as metal electrodes, piezoelectric materials, and microscopes. Creative researchers have leveraged this compatibility to develop many diverse microfluidic platforms for analyzing cells.

Single-cell, label-free microfluidic devices may soon be applied to assist clinical decision-making. Some cancers can be difficult to characterize based solely on protein expression because of high phenotypic heterogeneity or a complete lack of expression of traditional biomarkers [40,57]. Label-free microfluidics reduce the preparation time, reagents needed, and cost of conventional methods based on fluorescent or magnetic labels. Furthermore, these devices enable analysis of cell properties (*e.g.*, mechanical phenotype and dielectric

parameters) that cannot be characterized with traditional labels, and which could offer clinicians new information that will enable more precise diagnoses.

A valid criticism of the label-free, microfluidic single-cell analysis methods discussed here is that they are largely limited to measuring physical properties such as cell size, density, or deformability. However, each of these technologies has demonstrated some ability to correlate physical characteristics to pathologically relevant phenotypes. Furthermore, technological advances are enabling new applications of these techniques to evaluate other properties such as surface markers. Because microfluidic technologies are increasing in popularity, we are optimistic that label-free methods such as those described here might soon be as commonplace in clinical pathology laboratories as they are today in research laboratories.

The label-free microfluidic methods discussed here have been used to screen and analyze cells for a wide range of biomedical and clinical applications. Because of the versatility of label-free methods, the low-cost nature of microfluidics, and the rapid prototyping capabilities of modern microfabrication, we expect this class of technology to continue to be an area of high research interest going forward. New developments in this field will contribute to the ongoing paradigm shift in cell analysis and sorting technologies toward label-free microfluidic devices, enabling new capabilities in biomedical research tools and clinical diagnostics.

Chapter 3

Multi-Parameter Mechanical Screening with Mechano-Node-Pore Sensing

This chapter is adapted with permission in part from:

> B. Li*, K. L. Cotner*, N. K. Liu, S. Hinz, M. A. LaBarge, and L. L. Sohn, "Evaluating sources of technical variability in the mechano-node-pore sensing pipeline and their effect on the reproducibility of single-cell mechanical phenotyping", *PLOS ONE*, vol. 16, A. Han, Ed., e0258982, 10 Oct. 2021, ISSN: 1932-6203. DOI: 10.1371/JOURNAL.PONE.0258982. [Online]. Available: https://journals.plos.org/plosone/article?id=10.1371/journal.pone.0258982, *Equal contribution. [2]

While Chapter 2 provided an overview of the state of the field in single-cell microfluidic analysis platforms, this chapter will focus on one particular such technology: mechano-node-pore sensing (mechano-NPS). We will first discuss the motivation behind mechanical phenotyping, summarize the main technologies available to measure cellular mechanics, and describe how mechano-NPS fits within the field. We will then review the theoretical principles of mechano-NPS and describe generalized methods for device fabrication, experimental process, and data analysis. Finally, we will present the results of a systematic experiment evaluating the intra- and inter-user reliability of the mechano-NPS data processing software, which we examined for both experienced and novice users.

3.1 Background & Motivation

As discussed in the previous chapter, mechanical phenotyping is the process of measuring how a cell responds to a physical force, such as stretching or compression. The mechanical properties of cells have been implicated in a wide range of biologically and clinically relevant systems, especially in the development of cancer [40,41,43,58]. For example, more invasive

cells are shown to be softer than their benign counterparts [42,46,59,60]. Additionally, the viscoelastic components of cells have been implicated in the malignant progression for breast cancer cell lines [61], and cell recovery from deformation is thought to be important in migration and metastatic development [62].

AFM and micropipette aspiration are gold-standard methods for analyzing mechanical properties of cells. However, the throughput of these techniques is extremely low; published AFM studies [42,61,63] typically report ∼30 or fewer cells per condition, and micropipette aspirations take up to 10 min per cell [64]. For many applications, it may be infeasible to collect enough data using these techniques—for example, if a patient sample needs to be screened for a rare abnormal cell population among a background of many normal cells, or when capturing the full heterogeneity of an experimental condition that could then yield new insights into previously unknown subtypes of cells. As discussed in Section 2.3.2, a number of microfluidic methods have been developed in recent years that are capable of mechanical phenotyping with much higher throughput, including methods based on optical stretching [43,49] and hydrodynamic deformation [48,53]. In particular, hydrodynamic methods (also known as deformability cytometry) operate at hundreds to thousands of cells per second. However, both optical and hydrodynamic techniques are limited to measuring the aspect ratio of the cell as it is stretched or deformed; in other words, these methods only probe a single parameter of the elastic component of the cell's mechanical properties. Additionally, these techniques rely on hardware such as microscopes and high-speed video cameras that is high-cost, prone to failure, and not easy to scale or port to other locations. This reduces the accessibility of these techniques to new researchers both in terms of cost and of ease of use for a non-expert.

Mechano-NPS is a technology developed recently by Kim *et al.* [20] that fills a unique gap in the mechanophenotyping space. As it is based entirely on electronic sensing, the data acquisition hardware is primarily composed of relatively low-cost, easily accessible off-the-shelf electronic parts that a non-expert could directly assemble. Additionally, the sensing modality may be more robust than techniques that rely on high-speed microscopy imaging, as it is not sensitive to small changes in position and has almost no moving parts. While mechano-NPS does not have throughput as high as techniques such as deformability cytometry [48,53], users routinely acquire whole-cell data from hundreds of cells per hour. Moreover, one of the greatest advantages of this technique is its ability to simultaneously measure multiple cellular properties reflecting both the elastic and viscoelastic characteristics.

Mechano-NPS is a powerful platform because it combines the robustness and accessibility of electronic-based sensing with the ability to discern rich mechanical information about cells. Mechano-NPS has already led to important new biological discoveries: Kim *et al.* identified a major mechanical phenotype in primary human breast epithelial cells associated with aging, and also showed that normal cells have different mechanical properties compared to their descendants which had been progressively transformed (*i.e.*, induced to become more cancer-like) [20]. Li *et al.* used mechano-NPS to discover a mechanical biomarker that may correspond to drug resistance in acute promyelocytic leukemia [58]. Additionally, researchers are now developing a classification model based on machine learning with mechano-NPS data

that can identify epithelial cells from young women carrying high-risk germline mutations for breast cancer [65]. These discoveries relied on both the elastic and viscoelastic properties measured by mechano-NPS, as well as its high throughput (indeed, machine learning tasks famously require a large amount of training data). Overall, in just a few years, mechano-NPS has demonstrated its potential as a powerful new method to learn about cellular mechanics and their role in many biological systems.

As mechano-NPS is used by an ever-growing group of researchers across multiple labs and different institutions, we sought to understand the different sources of variability that could potentially lead to inconsistent results and to quantify the reliability and reproducibility of the platform. To this end, we demonstrated in [2] that there is high repeatability across the entire technology pipeline. We showed that device-device variability is limited to small effect sizes that are not biologically meaningful. We also conducted a unique study in which identical mechano-NPS experiments were performed by researchers at two different institutions using different hardware platforms, which showed that the mechanical phenotyping results obtained at the two locations were in good agreement. This is a crucial finding that provides high confidence in mechano-NPS results, even those obtained at different laboratories, and speaks to the platform's high potential for adoption by new research groups or even clinicians.

3.2 Theoretical Principles

Mechano-NPS is based on the underlying principle of RPS [13,14], which (as discussed in Section 2.2.1) is one of the most widely used methods for cell counting and sizing in microfluidics. Cells pass through a microfluidic channel while a constant voltage is applied, and the resulting current is measured continuously. When a cell enters the channel, it causes a transient current drop (*i.e.*, pulse) whose magnitude ΔI corresponds to the cell size and whose duration Δt indicates the transit time through the channel. The size of the cell can be determined by [14,66,67]:

$$\frac{\Delta I}{I} = \frac{D_{cell}^3}{D_{eff}^2 L}\left(\frac{1}{1-0.8\left({}^{D_{cell}}/_{D_{eff}}\right)^3}\right), \tag{3.1}$$

where I is the baseline current, D_{cell} is the cell diameter, D_{eff} is the effective diameter of the channel, and L is the length of the channel.

NPS [24] is an extension of the RPS concept in which the microchannel is divided into narrow segments (*i.e.*, pores) separated by wider nodes. When the cell passes through a segment, a current drop is observed as in traditional RPS; however, when the cell enters a node, the measured current returns to near-baseline level. Thus, as each cell transits the channel, it generates a distinct current pulse that consists of subpulses corresponding to the channel segments. The amplitude ΔI and duration Δt of each subpulse reflect cell size

and transit time, respectively, in the corresponding segment. The NPS channel geometry produces a unique, spatiotemporally encoded current signal, which leads to improvements in SNR and dynamic range over standard RPS devices [24]. Moreover, the cell size and transit time in each segment is measured independently by ΔI and Δt of the corresponding subpulse.

Kim *et al.* took advantage of the spatiotemporal encoding in the NPS channel geometry to develop a platform that could measure cells' response to mechanical force [20] (Fig. 3.1). First, the cell's initial size and speed are measured in one or more reference segments, where the cell is unconstrained. Then, the cell is forced through a contraction segment whose width is narrower than that of the cell, causing the cell to deform. Finally, the cell passes through several recovery segments, where it is allowed to return to its original size. By comparing the contraction subpulse to the reference subpulse, the cell's response to the compressive force is measured, thereby gleaning information about the cell's elastic properties. Likewise, information about the cell's viscoelastic properties can be obtained by comparing the recovery subpulse to the reference subpulses. Detailed calculations for specific mechanical parameters measured by mechano-NPS are provided below.

As the cell transits the contraction segment, it undergoes a constant compressive strain whose magnitude ε depends on the cell's original diameter D_{cell} and the contraction segment width w_c: $\varepsilon = {}^{(D_{cell}-w_c)}/_{D_{cell}}$. The cell's overall resistance to deformation is reflected in its transit time Δt_c through this contraction segment. To account for the effect of D_{cell} on the magnitude of the applied strain (and thus on Δt_c), the whole-cell deformability index ($wCDI$) is defined as a dimensionless parameter that is inversely related to elastic modulus and cortical tension [20]:

$$wCDI = \left(\frac{L_c}{U_{flow}h}\right)\left(\frac{D_{cell}}{\Delta t_c}\right), \tag{3.2}$$

where L_c is the length of the contraction segment, U_{flow} is the cell velocity in the reference segment, and h is the channel height.

Additionally, the magnitude ΔI_c of the current drop as the cell passes through the contraction segment is related to the deformed cell volume V_{deform} by ${}^{\Delta I_c}/_{I} \sim {}^{V_{deform}}/_{V_c}$, where V_c is the volume of the contraction segment [66]. Assuming the cell undergoes isometric deformation in two dimensions, the major radius L_{deform} of the resulting oblate spheroid is given by $V_{deform} = \frac{\pi}{6} w_c (L_{deform})^2$, where w_c is the width of the contraction segment. The transverse deformation of the cell in the contraction segment can thus be calculated as $\delta_{deform} = {}^{L_{deform}}/_{D_{cell}}$ [26].

Finally, the cell size is monitored in subsequent recovery segments to assess how quickly it returns to its original shape. $D_{cell,r}$ in each recovery segment is calculated based on ΔI in the corresponding subpulse, and the cell's recovery speed can be quantified based on how long $D_{cell,r}$ takes to return to the original value D_{cell}. In the case of a device with three recovery pores, as in [20] (Fig. 3.1B, Version #1), cells could be classified into up to four

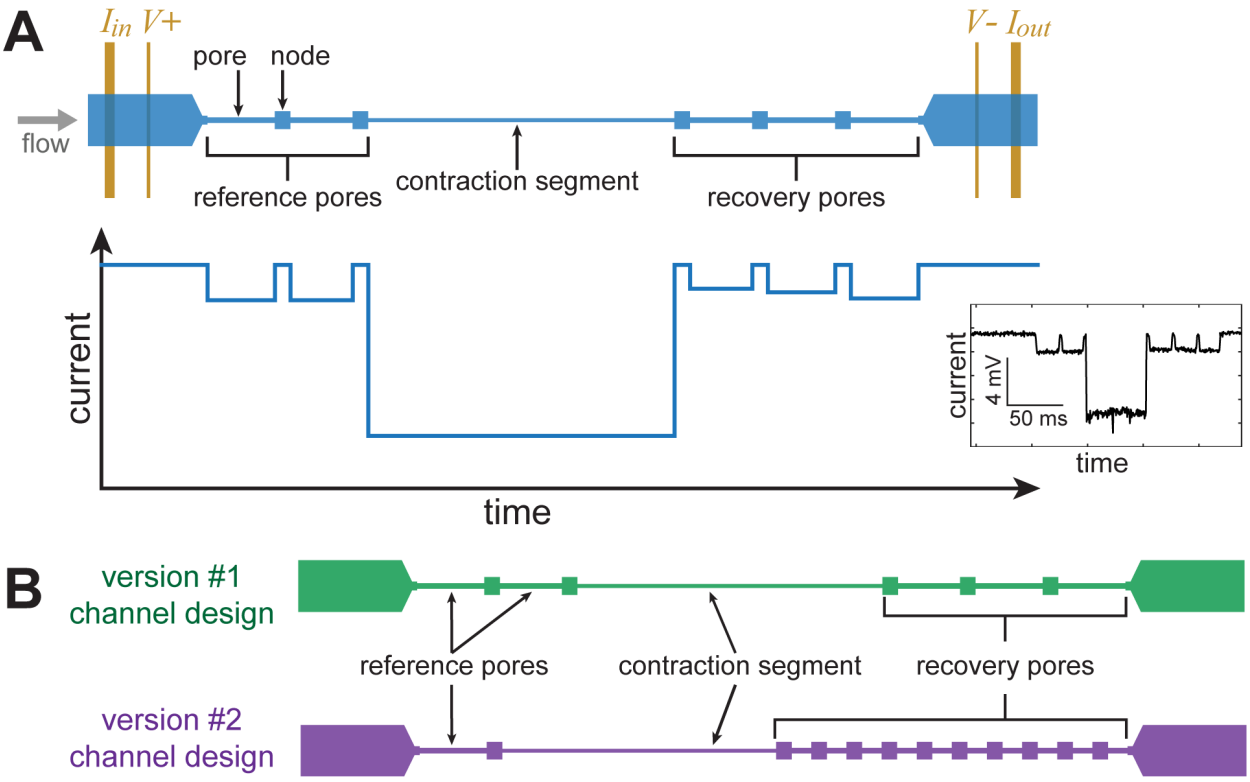

Figure 3.1: Overview of mechano-NPS operating principle and device design. Adapted with permission from [2]. (A) Top-down schematic view of a mechano-NPS device (top), with corresponding expected electric current pulse (bottom) caused by a single cell transiting the microfluidic channel. A potential is applied across the channel, causing a drop in measured current when a cell enters a narrow segment of the microchannel (pore). Inset: An actual current pulse caused by a cell traversing the channel. (B) Top-down schematic views of two different versions of mechano-NPS channel designs. Version #1 corresponds to the diagram and current pulse shown in Fig. 3.1A. Version #2 corresponds to the design used to generate raw test data for the experiment described in Section 3.4.

different levels of recovery speed: if $D_{cell,r}$ is already $\approx D_{cell}$ in the first recovery segment, the cell is considered to have instant recovery; if $D_{cell,r}$ does not recover until the second or third recovery segment, the cell is considered to have transient-fast or transient-slow recovery, respectively; and if $D_{cell,r}$ is still not recovered to its original level by the last recovery segment, it is considered to have prolonged recovery time.

Li *et al.* advanced mechano-NPS by including many shorter recovery segments instead of just a few longer ones [58] (Fig. 3.1B, Version #2). This design allowed them to measure the cell's recovery speed with greater precision by fitting a continuous recovery time constant τ using the Kelvin-Voigt model for viscoelastic materials. This model predicts how cell strain will relax over time after being released from the contraction segment:

$$\varepsilon(t) = \varepsilon_0 \, exp\,(^{-t}/_{\tau}) + \varepsilon_{\infty}, \tag{3.3}$$

where $\varepsilon(t)$ gives the strain at time t after being released from the contraction segment, ε_0 gives the strain at the time of release, τ is the cell's recovery time constant, and ε_{∞} is the cell's steady-state (recovered) strain. Here, "strain" indicates the cell size/shape relative to its relaxed, unstressed shape—in other words, "strain" can be measured by the apparent cell size as determined by ΔI in the corresponding NPS subpulse.

3.3 Methods

3.3.1 Device Fabrication

An overview of the fabrication process for most NPS and mechano-NPS devices is shown in Fig. 3.2–3.4. Briefly, a negative master mold of NPS microchannels is fabricated from SU-8 epoxy using photolithography; PDMS channels are then created from the mold using soft lithography (Fig. 3.2). Electrodes are patterned on a glass substrate using photolithography and electron-gun deposition (Fig. 3.3). Finally, the PDMS channels and substrate with prefabricated electrodes are bonded together via oxygen plasma treatment (Fig. 3.4). Each of these processes are described in more detail below.

Microfluidic channel structures are fabricated in PDMS using soft lithography (Fig. 3.2). First, a negative-relief master mold is fabricated by patterning SU-8 epoxy photoresist on a polished silicon substrate through photolithography. Specific SU-8 resist, spin speed, exposure energy, development time, and baking steps depend on the desired channel height. The datasheet provided by the resist manufacturer (Kayaku Advanced Materials) provides protocols that are a starting point, but parameters should be adjusted as needed to achieve the desired channel height. Specific protocols used for experiments in this dissertation are listed in the corresponding methods sections. After the negative-relief master mold is created, PDMS is mixed at a 9:1 ratio by weight of pre-polymer base to curing agent and degassed for ∼30 min or longer. The PDMS is poured onto the master mold and cured at 85 °C for 2 h. Finally, molded PDMS slabs are excised, and inlet and outlet ports are cored using a biopsy

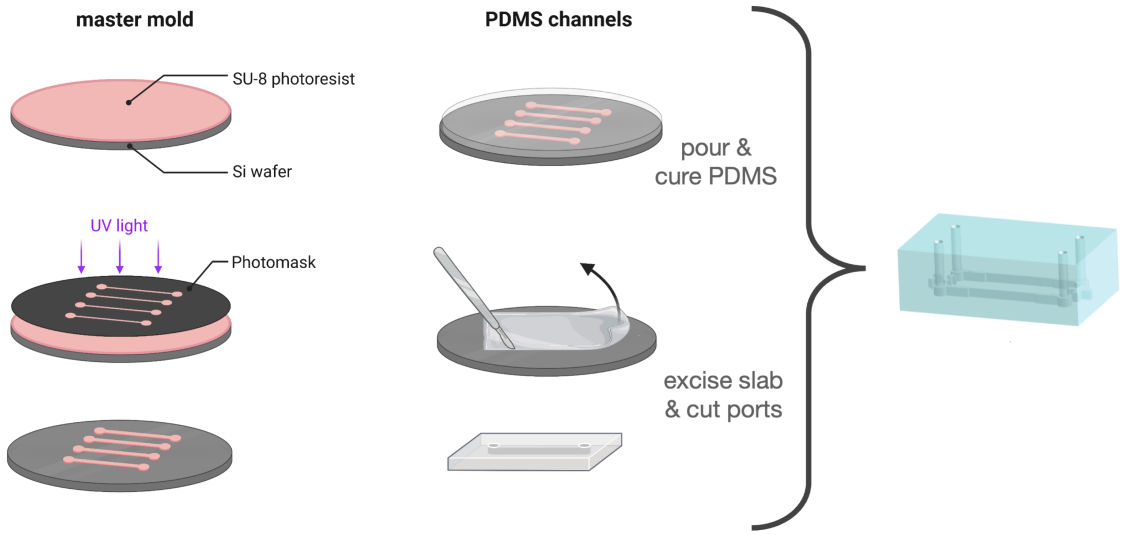

Figure 3.2: PDMS fabrication process for NPS and mechano-NPS devices. Left: A negative-relief master mold is fabricated through SU-8 photolithography on a silicon substrate. Center: PDMS is poured over the master mold and cured. PDMS slabs containing embedded channels are then excised, and inlet and outlet ports are created. Adapted in part from "PDMS Microfluidic Chip Fabrication" by BioRender.com (2022, retrieved from https://app.biorender.com/biorender-templates).

punch. For extremely sensitive measurements, device-device variation may be minimized by utilizing PDMS slabs cast from the same position on silicon substrate.

Electrodes are patterned on a glass substrate using standard photolithography (Fig. 3.3). Shipley 1813 photoresist is spun onto a glass substrate at 3000 rpm and baked at 100 °C for 90 s. The resist-coated substrate is UV-exposed to a transparency mask at 320 mJ/cm^2 and immersed in MF-321 developer for ∼30 s with gentle agitation. The resist-coated substrate is rinsed with deionized (DI) water (18 MΩ). A trilayer of metal (100 Å Ti, 250 Å Pt, 250 Å Au) is deposited by electron-gun evaporation, and photoresist liftoff is performed by immersing the substrate in acetone for ∼1 h, followed by further rinsing with acetone as needed. Finally, the gold layer is removed from the section of the electrodes that crosses the microchannel using Gold Etchant TFA, thereby exposing the platinum electrodes and preventing cellular adhesion during experiments.

Before bonding, the PDMS slab is cleaned with scotch tape; it may also be rinsed briefly with isopropanol and DI water. The glass substrate with prefabricated electrodes is cleaned by rinsing with acetone, isopropanol, and methanol. The glass substrate and PDMS are exposed to oxygen plasma (60 Pa, 30 W, 2 min), then aligned and mated (Fig. 3.4). Complete bonding is achieved by a brief baking step (*e.g.*, 5 min at 125 °C). For best practice, it is important to wait at least several hours after bonding and before performing experiments

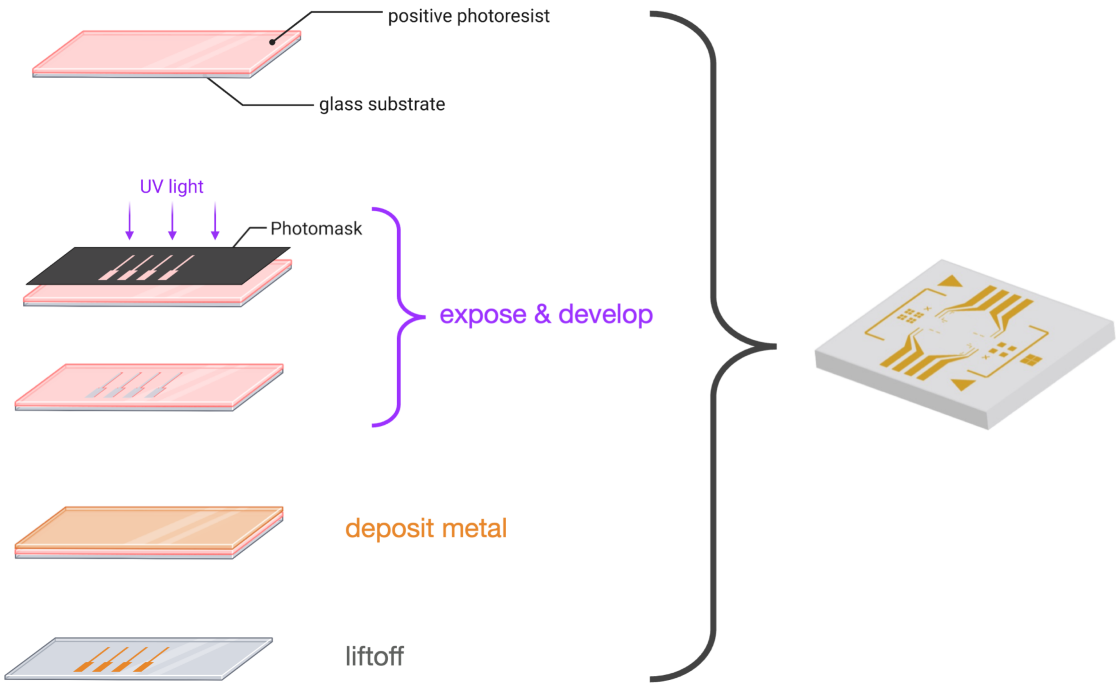

Figure 3.3: Electrode fabrication process for NPS and mechano-NPS devices. Electrodes are fabricated by patterning Shipley-1813 positive photoresist onto a glass substrate through photolithography, followed by electron-gun evaporation to create Ti/Pt/Au electrodes. Finally, liftoff is performed to reveal the patterned electrodes. Created in part with BioRender.com.

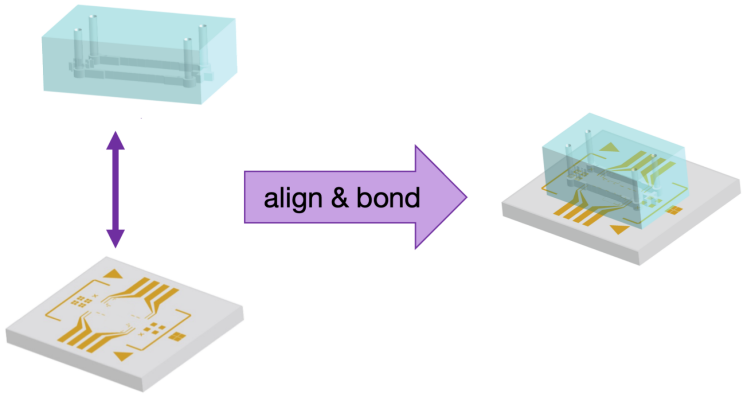

Figure 3.4: Bonding process for NPS and mechano-NPS devices. The PDMS slab and glass substrate with the prefabricated electrodes are exposed to oxygen plasma and are subsequently aligned and bonded to create the final device.

to ensure that the bonding process is completed, especially when high driving pressures are needed (*e.g.*, for mechano-NPS experiments).

To assist with aligning the PDMS slabs to the glass substrate, ∼20 µL of a 2:1 mixture of methanol to DI water may be deposited onto the glass substrate after plasma treatment and before mating with the PDMS. This provides a temporary buffer between the PDMS and the glass, allowing the alignment to be adjusted before bonding is finalized. When the alignment is acceptable, the device should be baked on a hot plate to evaporate the methanol-water mixture (*e.g.*, 2 h at 85 °C).

3.3.2 Experimental Process

Cells should be cultured according to standard practices for the cell type. Before NPS measurements are performed, cells should be passaged according to standard practices (*e.g.*, trypsinization to dissociate adherent cell lines), rinsed with 1X phosphate-buffered saline (PBS), and diluted to a final working concentration of $\sim 300\text{–}500 \times 10^3$ cells/mL in a solution of 2 % fetal bovine serum (FBS) in PBS. (The addition of FBS helps reduce cell clumping and cell adhesion to the PDMS microchannel walls.) If desired, the cell suspension may be passed through an appropriately-sized cell strainer (*e.g.*, 30 µm to filter MCF-7 cells) to remove large clumps of cells. The prepared cell solution should be kept on ice until NPS measurements are performed.

NPS measurements are performed as described in [20,24,68]. The cell suspension is injected into the device inlet and driven through the channel using a non-pulsatile pressure source. The appropriate driving pressure depends on the fluidic resistance of the device and may need to be tuned for each new device design and/or experiment type. Typical driving pressures for mechano-NPS experiments range from 70 mbar to 210 mbar (mechano-NPS device designs have a higher fluidic resistance than other NPS devices due to the contraction segment). It is best practice to test each experimental condition using at least three different NPS devices, due to possible device-device variability (as discussed by [2]).

A standard four-terminal measurement is performed to measure the electrical current across the device while a constant voltage (usually ∼1–5 V) is applied. For experiments described in Chapters 3–5, we use the NPS data acquisition platform previously described [24,68]. Briefly, a custom printed circuit board (as shown in [20]) interfaces with the NPS device and performs the four-terminal measurement. The measured current is amplified by a current-to-voltage converter (DL Instruments) and recorded using a commercial data acquisition device (National Instruments). Custom MATLAB data acquisition software, which is compatible with National Instruments data acquisition devices, is publicly available at `https://github.com/sohnlab/node-pore-sensing-public` [69].

Device Calibration

In order to calculate cell size via Eq. 3.1, the device's effective diameter D_{eff} must be determined experimentally. As described by Kim *et al.* [20], this can be accomplished by

taking reference measurements with commercial polystyrene beads of known size. As the beads should be a comparable size to the cells of interest, a "reference device" must be used where the contraction segment is replaced with a pore of the same width as the reference pores and the same length as the original contraction segment. Calibration should be performed for each new negative-relief master mold that is fabricated.

Calibration data should be collected by taking NPS measurements of the commercial polystyrene beads in the same way as cells are measured. The same experimental settings (*e.g.*, applied voltage and preamplifier sensitivity) should be used for calibration experiments as cell measurements. Polystyrene beads are often more prone to clogging than cells are, so it is common to supplement the PBS solution with a surfactant such as 1.5 % Tween to reduce adhesion. Additionally, it may be necessary to dilute the beads to a lower concentration than cells.

An alternative option for generating reference measurements (described in [68]) is to measure a sample of cells using a commercial RPS cell sizing device (*e.g.*, Millipore Sigma Scepter 2.0 Handheld Automatic Cell Counter), and to measure a sample of cells from the same population using NPS. Since the cells are able to squeeze through the contraction segment, no separate "reference device" design is needed.

In either case, the reference data should be analyzed as described in Section 3.3.3 to extract subpulse amplitude data for the measured beads or cells (specifically, subpulse amplitudes from the reference pores should be used). Then, using Eq. 3.1, a value for D_{eff} should be fitted such that the mean calculated diameter of the reference data matches the known mean diameter (as provided by the bead manufacturer or as measured by the commercial RPS device).

3.3.3 Data Analysis

Raw current data is preprocessed by low-pass filtering (*e.g.*, by applying a moving-average filter or by applying a cutoff in the frequency domain) to remove high-frequency noise. The baseline drift is removed, either by linear detrending on the time scale of a single cell transit pulse, or by a more sophisticated fitting method such as asymmetric least-squares [70]. The baseline current must be known in order to calculate ΔI, and in turn, D_{cell}, $wCDI$, and δ_{deform} (as described in Section 3.2). Cell pulses are detected and subpulse information is extracted by applying an edge detection algorithm as described by [20] (see Fig. 3.5). Briefly, the approximate first derivative of the signal is calculated, and the subpulses are identified by the local minima and maxima in this "derivative signal" caused by the cell entering and exiting each pore, respectively. The amplitude ΔI and width Δt are then calculated for each subpulse (average value and elapsed time, respectively). Cell properties are calculated from these values as described in Section 3.2.

The process of extracting cell pulse data as described above can be tedious and time-consuming to perform manually, as there may be many cell pulses that must be discarded (*e.g.*, when cell measurements overlap). Furthermore, the peaks in the derivative signal corresponding to the subpulses can be difficult to detect against the background noise. In

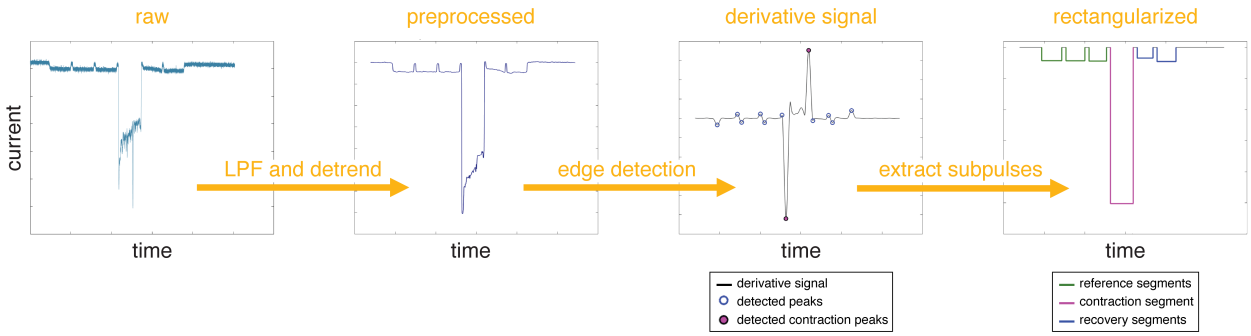

Figure 3.5: Data processing method for mechano-NPS. Data is first preprocessed by low-pass filtering (LPF) and baseline removal (detrend), followed by detection of cell events and subpulses by identifying peaks in the approximate first-order derivative (derivative signal). Finally, the time duration and average value are extracted from each subpulse, as visualized by the rectangularized pulse.

order to address these issues, Li *et al.* [2] developed a MATLAB command-line interface (CLI) program that performs initial pulse detection automatically, and then asks for user input to check the results for each cell and adjust processing parameters as needed. This new, semi-automatic software improves the speed of mechano-NPS data analysis roughly ten-fold over the original software [2].

Software for this improved CLI-based data processing method is available publicly at `https://github.com/sohnlab/mechanoNPS_Li-et-al-2020` [71], and a newer version is also available at `https://github.com/sohnlab/NPS-analysis-JOVE` [72]. An overview of the pipeline for using this software is presented in Fig. 3.6, and detailed instructions are provided in Section 3.5. Briefly, the software performs an initial scan of the data to generate a list of potential cell pulses, and asks the user to evaluate each one. Two user inputs are required: first, the user must decide to save the cell pulse or to discard it as invalid; then, for saved cell pulses, the user must adjust two processing thresholds as needed to generate the appropriate rectangularized pulse.

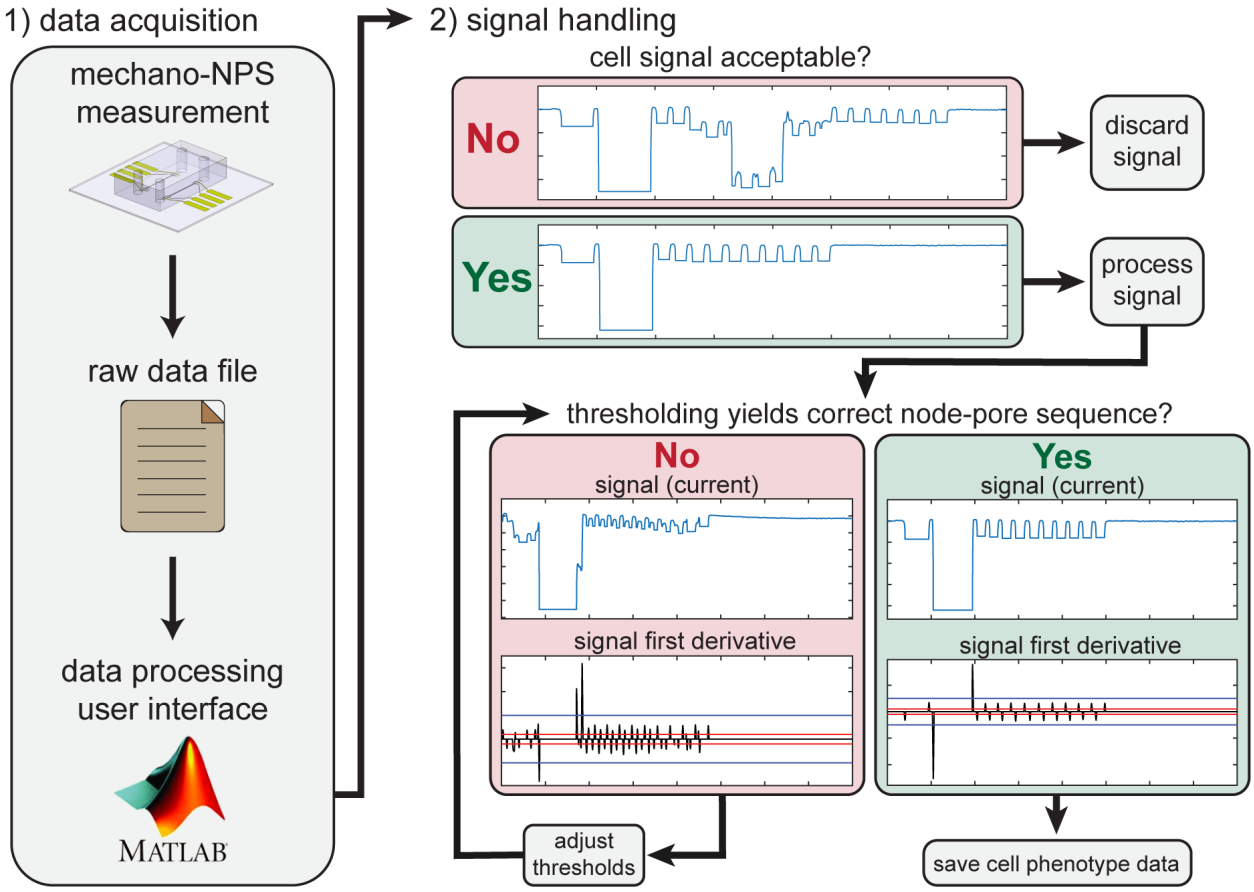

Figure 3.6: Overview of mechano-NPS data analysis software. The flow of user input to the software involves two steps: First, the user must identify valid signals corresponding to cell measurements and exclude non-valid pulses. Subsequently, the user must set processing thresholds to the appropriate levels for each valid cell. Adapted with permission from [2].

3.4 Reproducibility of the Mechano-Node-Pore Sensing Data Analysis Software

Understanding that user input to the custom mechano-NPS data processing software described in Section 3.3.3 has a major impact on the data extracted from an experiment, we sought to quantify the variability introduced through the pipeline's semi-manual nature [58,71] (Fig. 3.6). We focused on answering three questions: 1) How consistent is one user's results obtained with the software, upon repeated analysis of the same data? 2) How much do results vary between different users analyzing the same data set? 3) How does user expertise with this software package affect the ability to produce consistent results? We conducted a systematic study to not only address these questions, but also determine

the reliability of this data-processing method in context with device-device variability and experimental differences due to location and hardware instrumentation [2].

3.4.1 Methods

Device Design and Fabrication

The mechano-NPS device used to collect the raw data in this study is the same design used in [58], comprising one reference pore, one contraction segment, and ten short recovery pores (Fig. 3.1B, Version #2). The pore width in the reference and recovery pores was 13 µm, while the contraction segment width was 7 µm (targeting an average applied strain of 0.35). The reference pore was 800 µm long, the contraction segment was 2000 µm long, and each recovery pore was 290 µm long. The nodes were each 85 µm wide × 50 µm long. Devices were fabricated as described in Section 3.3.1. The master mold was fabricated in SU-8 3010 epoxy photoresist, and the final channel height was 12.9 µm.

Raw Data Collection

Raw mechano-NPS data was collected by measuring AP-1060 cells (DSMZ ACC 593, a gift from Dr. S. Kogan, University of California, San Francisco, CA, U.S.A.). The cells were cultured according to standard methods (see [2]). Two cell samples were treated with the microfilament-disrupting agent Latrunculin A (LatA) at 2 µM for 30 min, and three cell samples were left untreated. See [2] for details on cell culture and treatment methods used to collect the raw data.

Each cell sample was measured with mechano-NPS as described in Section 3.3.2. After passaging the cells according to standard methods [2], the cells were washed with 1X PBS and resuspended at 3×10^5 cells/mL in 1X PBS with 2 % FBS. The cell suspension was injected into the mechano-NPS channel with a driving pressure of 80 mbar. A four-terminal measurement was performed as described in Section 3.3.2 to acquire the raw current data that we used to conduct our software reliability study.

Intra- and Inter-User Reliability study

We recruited five subjects who are microfluidics researchers with varying degrees of familiarity with mechano-NPS and surveyed them about their familiarity with the mechano-NPS data processing software. Subjects 1–2 identified as experienced users of the software, while Subjects 3–5 identified as novice users of the software. We then provided all subjects with a copy of the mechano-NPS data processing software from [71], along with a 30-minute training video on how to use it. All subjects were tasked with performing data processing on five blinded mechano-NPS raw data sets using the custom software. These data sets comprised five measurements (A–E) of AP-1060 cells (Fig. 3.7–3.8), as described above. Data sets A–C were obtained from measuring the untreated cell samples, while data sets D–E were obtained from measuring the cell samples treated with LatA. Additionally, each subject performed

analysis on each data set three different times in order to test intra-user reliability. Overall, we examined both intra- and inter-user reliability using the results from experienced and novice users of the software.

This human subjects study was conducted under an IRB-approved protocol (UC Berkeley Committee for Protection of Human Subjects, Protocol ID: 2020-11-13822), and all subjects provided written informed consent prior to taking part in the study.

3.4.2 Results

As described in Section 3.3.3, the CLI-based data processing software asks for two user input decisions for each potential cell measurement (Fig. 3.6): first, whether to save the pulse or to discard it as invalid, and second, to confirm or adjust two thresholds that affect the recorded cell phenotype measurements (see Section 3.5 for additional details). Since these data sets were obtained using a device design like that of [58] (as depicted in Fig. 3.1B, Version #2), the measurement of cell recovery from deformation is given by the continuous recovery time constant τ. The number of cells identified by a single user from a single raw data file ranged from 49–82.

Consistency of Saved and Discarded Pulses

We first analyzed the consistency of each user's decisions to save or discard cell measurements. We calculated percent-agreement and performed Fleiss's kappa analysis on the decision to save or skip each cell. The intra-user agreement analysis (Fig. 3.9A) showed that all subjects exhibited a high degree of self-consistency in their decisions to save or discard cell measurements. The experienced software users were designated as showing "perfect agreement" according to Landis & Koch's interpretation of the Fleiss's kappa values [73], while the novice users demonstrated "substantial" or "moderate" agreement. For all users, the null hypothesis was rejected in Fleiss's kappa analysis, indicating that the observed agreement was not accidental. The inter-user Fleiss's kappa analysis (Fig. 3.9B) showed that the over-

Figure 3.7 ***(following page)*****:** Intra- and inter-user comparison of results obtained using the mechano-NPS data processing pipeline. Processed data obtained from measurements of AP-1060 cells. Data sets A–C were obtained from measuring untreated cells, while data sets D–E were obtained from measuring cells treated with LatA. Plots show $wCDI$ (A) and recovery time constant τ (B) results, respectively. Processed data is shown from each of the five subjects across three replicate data processing tasks. Data is presented as originally returned after the data processing task was completed (*i.e.*, before erroneous measurements were excluded). Sample medians are represented by black dots; sample interquartile ranges are represented by thick lines; outliers are represented by filled circles and are defined as 1.5 times the inter-quartile range. Extreme values are represented as filled circles placed above or below the dashed lines and are defined as >2 or <0 for both $wCDI$ and τ. Number of cells found in each observation ranged from 49–82. Reprinted with permission from [2].

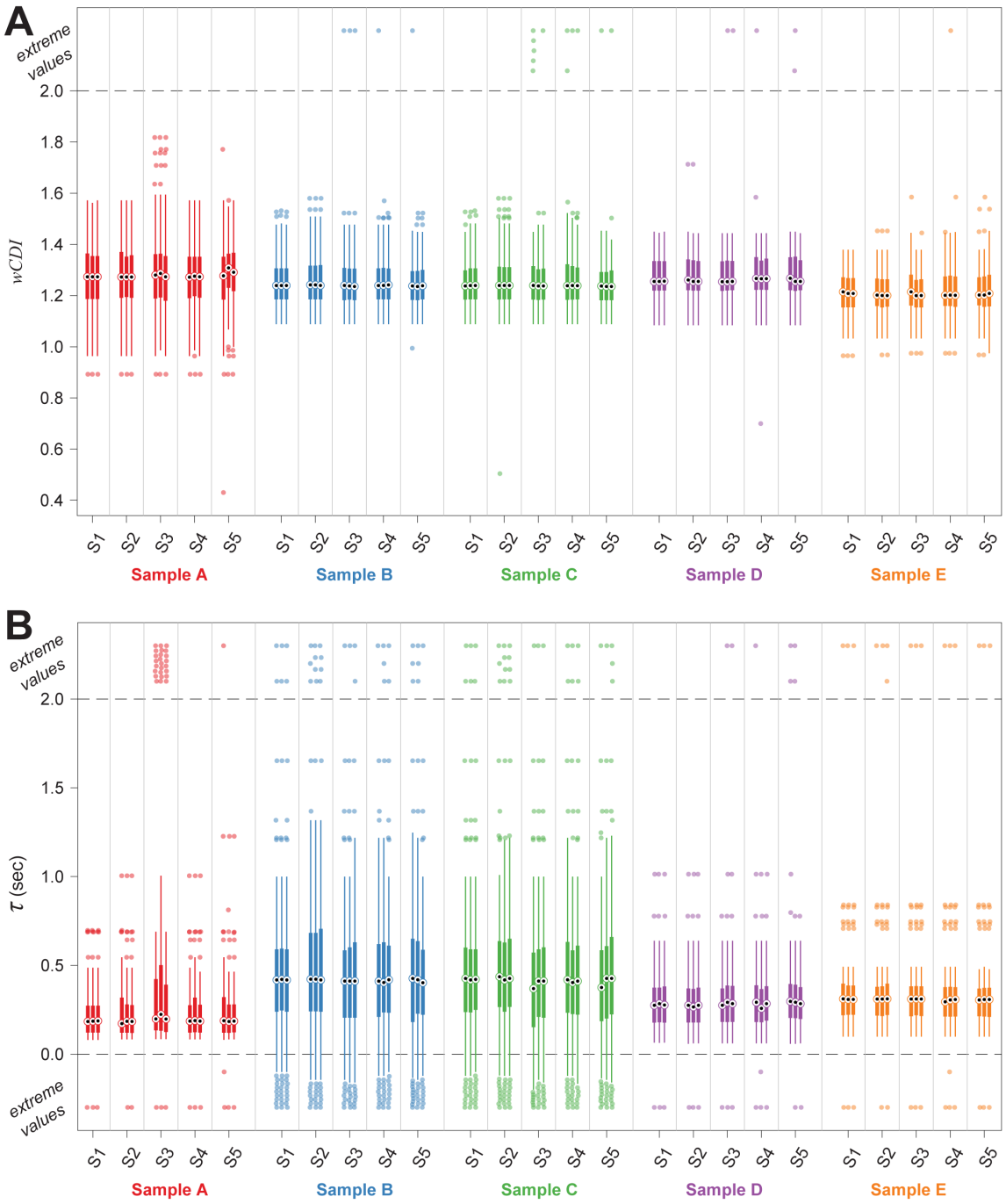
A
extreme values
2.0
1.8
1.6
1.4
1.2
1.0
0.8
0.6
0.4
wCDI
S1 S2 S3 S4 S5
Sample A
Sample B
Sample C
Sample D
Sample E
B
extreme values
2.0
1.5
1.0
0.5
0.0
extreme values
τ (sec)

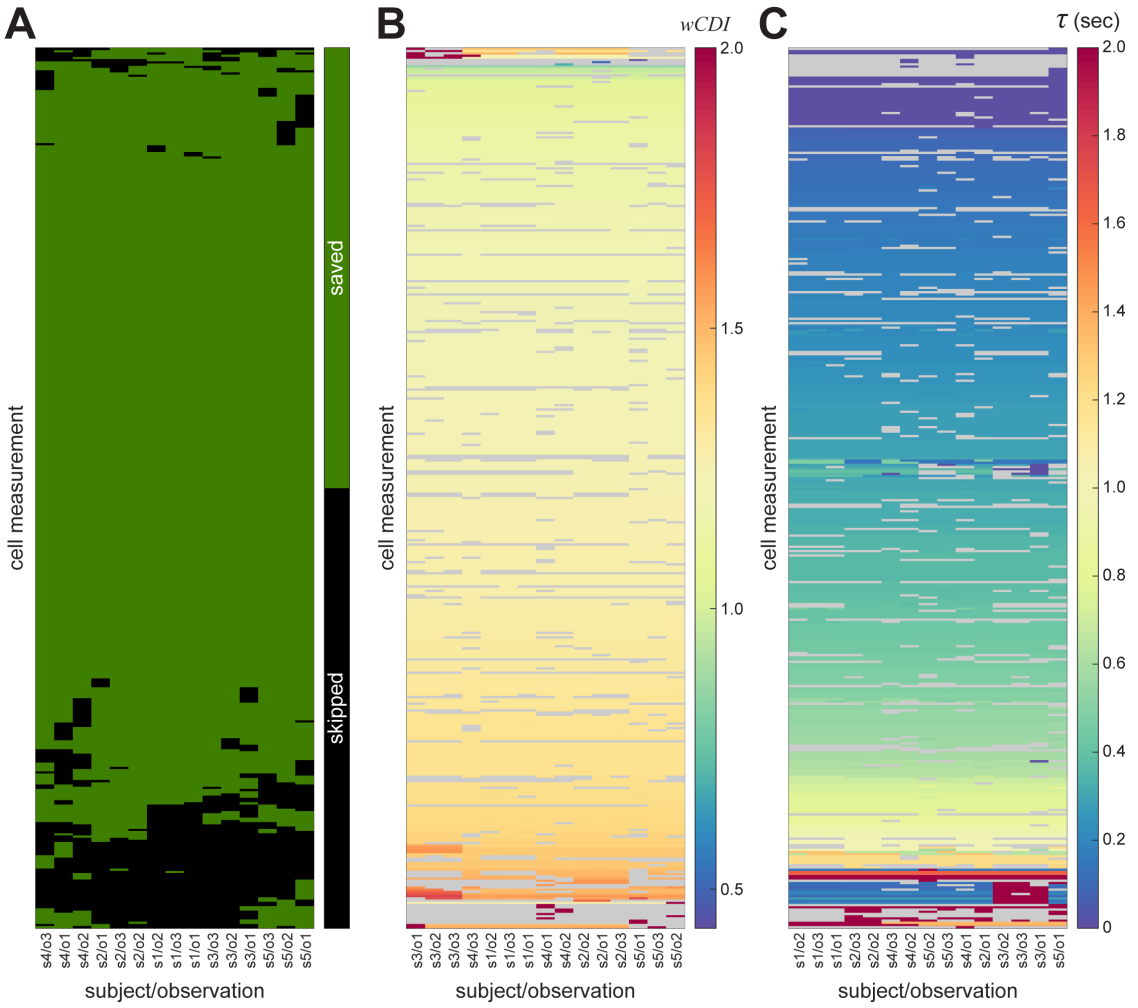

Figure 3.8: Repeated analysis of raw data files using the mechano-NPS data processing software by multiple users. Five subjects analyzed raw mechano-NPS data taken from AP-1060 cells; each subject processed the raw data files three different times using the mechano-NPS data processing software. Heat maps show unique cell measurements as rows, and each subject's repeated observations using the software as columns. Heat maps were generated using MATLAB R2020a with hierarchical clustering of rows and columns by Euclidean distance. The color scales show, for each observation, whether the cell measurement was saved or skipped (A), the measured $wCDI$ value (B), and the measured recovery time constant (τ) value (C). Data is presented as originally returned after the data processing task was completed (*i.e.*, before erroneous measurements were excluded). For (B) and (C), the color scale is limited to the non-extreme range of >0 and <2 for both $wCDI$ and τ. For (B) and (C), cell measurements that were skipped in the given observation are colored gray, and the missing values were imputed for clustering using k-nearest-neighbors. The total number of cells measured across all observations was 398. Reprinted with permission from [2].

all consistency between all subjects was moderately high (∼80 % agreement above chance), and "fair agreement" was observed. Pairwise analysis of the agreement between subjects revealed that the experienced users and one novice user (Subject 3) had a high degree of agreement with each other. Subjects 1–3 showed "moderate" or "substantial" agreement with each other, while all other subjects showed "fair agreement" with each other. For all comparisons, the null hypothesis was rejected. Importantly, Fleiss may be an overly conservative measure of agreement because it considers the possibility that users may assign labels randomly, which is unlikely in this data processing task. Moreover, this analysis cannot account for agreement on cells that were skipped in all observations, so the probability of encountering a cell that should be saved (and thus, the probability of agreeing to save a cell by chance) is highly overestimated in the Fleiss calculation. For these reasons, we also calculated the raw percent-agreement value, which directly quantifies the percentage of times that the observations agreed on whether to save or skip a cell. For all intra- and inter-user analyses, the raw percent-agreement was ∼85 % or higher, and the two experienced users and Subject 3 showed >90 % raw agreement among themselves.

Consistency in Observed Phenotypes

We then analyzed the consistency of the observed quantitative cell phenotypes, which can be affected by the thresholds set by the user. We focused on analyzing the parameters $wCDI$ and τ, since these were the parameters of interest in the original experiment [58]. For each of these two mechanical phenotyping variables, we calculated the percentage of cells where an equivalent value was found in each observation, and we also calculated the intra-class correlation (ICC) to quantify the correlation in the measured values between observations. The

Figure 3.9 ***(following page)*****:** Intra- and inter-user reliability analysis of the mechano-NPS data processing pipeline. Reliability analysis results obtained from the data presented in Fig. 3.7. "(e)" and "(n)" designate experienced and novice users, respectively. Number of cells found in each observation ranged from 49–82. Reprinted with permission from [2]. Intra- (A) and inter-user (B) agreement analysis examines the consistency of users' decisions to save or discard cell measurements. "% agreement" quantifies the percentage of potential cell events in which all observations agreed on whether to save or discard the event. Fleiss's kappa analysis was also performed to determine the "kappa" value as well as the "% agreement above chance." "Landis & Koch 1997" indicates the interpretation of the kappa value according to [73]. For all comparisons, Fleiss's kappa analysis rejected the null hypothesis that the observed agreement was accidental ($p < 10 \times 10^{-10}$). (C) Intra- and inter-user concordance analysis examines the consistency of the observed quantitative cell phenotypes for each of the two phenotype variables: $wCDI$ and recovery time constant τ. "% agreement" quantifies the percentage of cell events in which all observations found the same phenotype value, within tolerance. We also calculated the intra-class correlation (ICC) value, which quantifies the degree of correlation among the observations. For all comparisons, ICC analysis rejected that the null hypothesis that $ICC = 0$ ($p < 10 \times 10^{-10}$).

A

	% agreement	kappa	% agreement above chance	Landis & Koch 1997
S1 (e)	97.9	0.934	98.3	Perfect agreement
S2 (e)	96.1	0.853	97.0	Perfect agreement
S3 (n)	91.4	0.771	93.6	Substantial agreement
S4 (n)	84.7	0.562	88.4	Moderate agreement
S5 (n)	86.4	0.579	89.3	Moderate agreement

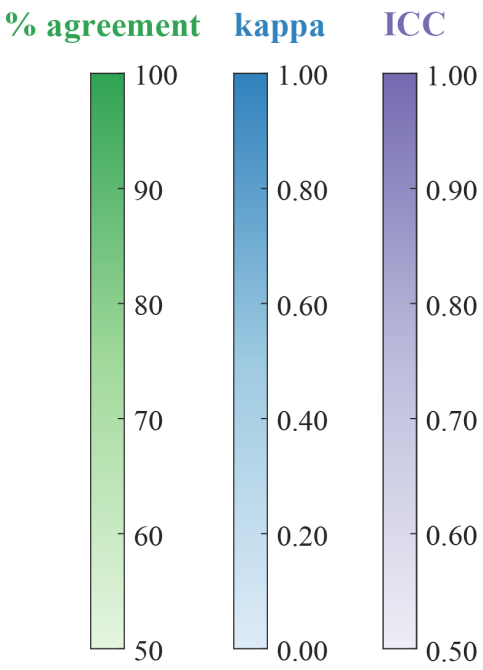

B

	% agreement	kappa	% agreement above chance	Landis & Koch 1997
S1-S2 (e-e)	92.9	0.595	89.2	Moderate agreement
S1-S3 (e-n)	93.8	0.630	87.9	Substantial agreement
S1-S4 (e-n)	86.2	0.306	75.6	Fair agreement
S1-S5 (e-n)	86.1	0.301	75.9	Fair agreement
S2-S3 (e-n)	91.0	0.493	84.2	Moderate agreement
S2-S4 (e-n)	87.4	0.298	76.4	Fair agreement
S2-S5 (e-n)	86.6	0.292	76.6	Fair agreement
S3-S4 (n-n)	87.8	0.397	76.4	Fair agreement
S3-S5 (n-n)	87.9	0.362	75.4	Fair agreement
S4-S5 (n-n)	86.4	0.270	70.4	Fair agreement
overall	86.6	0.389	78.8	Fair agreement

C

wCDI: % agreement					
	S1 (e)	S2 (e)	S3 (n)	S4 (n)	S5 (n)
S1 (e)	88.9	75.8	78.8	74.9	62.4
S2 (e)		88.9	81.9	81.8	68.8
S3 (n)			88.7	85.1	71.2
S4 (n)				79.5	67.8
S5 (n)					66.4
overall inter-user			57.2		

wCDI: ICC					
	S1 (e)	S2 (e)	S3 (n)	S4 (n)	S5 (n)
S1 (e)	1.00	1.00	0.96	1.00	1.00
S2 (e)		1.00	0.97	1.00	1.00
S3 (n)			1.00	0.97	0.97
S4 (n)				1.00	1.00
S5 (n)					1.00
overall inter-user			0.99		

τ: % agreement					
	S1 (e)	S2 (e)	S3 (n)	S4 (n)	S5 (n)
S1 (e)	84.8	73.3	75.6	71.1	58.6
S2 (e)		88.3	80.8	79.9	65.6
S3 (n)			88.7	84.6	67.4
S4 (n)				79.5	64.4
S5 (n)					61.7
overall inter-user			54.6		

τ: ICC					
	S1 (e)	S2 (e)	S3 (n)	S4 (n)	S5 (n)
S1 (e)	0.99	0.98	0.82	0.91	0.90
S2 (e)		0.92	0.92	0.97	0.95
S3 (n)			1.00	0.95	0.99
S4 (n)				0.95	0.97
S5 (n)					0.96
overall inter-user			0.94		

intra-user analysis (Fig. 3.9C, along the diagonals) showed that all subjects found equivalent values for both variables a majority of the time; most of the users found equivalent values for both variables ∼80 % of the time or more, although one of the novice users (Subject 5) only found equivalent values for the variables ∼60–70 % of the time. However, the intra-user correlation of values was very high for all subjects ($ICC > 0.9$), demonstrating a very high degree of self-consistency in both variables. The inter-user analysis (Fig. 3.9C) was similar to the intra-user analysis, showing that subjects found equivalent values with each other for both $wCDI$ and τ a majority of the time. We again found that the two experienced users and one of the novice users (Subject 3) showed a higher degree of consistency among themselves than with the other two novice users according to the percent-agreement analysis. However, the ICC analysis showed a very high degree of correlation in both variables among all users ($ICC > 0.9$ in all but one comparison). For all intra- and inter-user analyses, the null hypothesis that $ICC = 0$ was rejected for both $wCDI$ and τ.

Statistical Analysis

Statistical outliers, defined as more than 3 median absolute deviations from the sample median, were included in all statistical tests. Erroneous measurements were identified based on cell velocity by first excluding statistical outliers and then setting a cutoff of ±4 median absolute deviations from the sample median velocity in either the reference pore or contraction segment. Erroneous measurements were excluded from all statistical tests and analyses unless otherwise stated.

Intra- and inter-user reliability analysis was performed on cell phenotype data resulting from each data processing observation of the same five raw data files. For all analyses of a given comparison, only cells that were saved in any observation within the comparison group were considered. The percent-agreement was calculated according to the decision to save or discard each observed cell, thus quantifying how often the observations agreed on whether to save or discard a cell (erroneous measurements were not excluded from this analysis). Fleiss's kappa analysis was also performed according to the decision to save or discard each cell (using an implementation by Shah, 2020 in MATLAB R2020a), with the significance criterion of $\alpha = 0.05$ referring to the threshold beyond which the agreement is statistically significantly better than chance (erroneous measurements were not excluded from this analysis) [74,75]. Confidence intervals and p-values for Fleiss's kappa analysis are reported in Table 3.1. ICC analysis was performed on the data for $wCDI$ and recovery time constant using the `irrNA` implementation in RStudio version 1.2 [76,77], using a 2-way mixed-effects model to evaluate single-rater absolute agreement, with the null hypothesis that $ICC = 0$ evaluated at $\alpha = 0.05$. Table 3.2 reports confidence intervals and p-values for ICC analysis, as well as the effect of excluding erroneous measurements in this analysis. Additionally, percent-agreement was calculated on the data for wCDI and recovery time constant, calculating the percent of cell events in which all observations found an equivalent value for the measured phenotype. Measured values were considered equivalent if the difference was within a tolerance of 1×10^{-10} multiplied by the minimum absolute value observed for the

measured phenotype. Table 3.3 reports tolerance values used as well as the effect of excluding erroneous measurements on this analysis.

3.4.3 Discussion

Overall, the agreement and correlation analyses demonstrate that the semi-manual mechano-NPS data processing platform enables reproducible results. Users demonstrate consistent results upon repeated analysis of the same data set, and different users find results that are consistent with each other. Although experienced users do show a higher degree of consistency than novice users, novice users of this software are still able to achieve reliable results right away. This finding is critical for ensuring that the mechano-NPS platform, and its associated data processing pipeline, are reproducible even when adopted by new and inexperienced users.

3.4.4 Conclusions

Having quantified the expectation for technical variability due to device and hardware variation in [2], we also demonstrated highly reproducible results from our semi-manual data-processing software. We also showed that novice users are able to adopt the software and obtain reliable results immediately. Thus, we have demonstrated that mechano-NPS is a highly reproducible mechanical phenotyping platform across the entire technology pipeline, from device fabrication and experimental process through data analysis. As new researchers and laboratories continue to adopt this technology, we can be confident that results obtained by different users—even novice users—will be highly consistent and reliable.

Comparison	Subject(s)	kappa	lower bound	upper bound	p
intra-user	subject1	0.934	0.919	0.949	0
	subject2	0.853	0.837	0.868	0
	subject3	0.771	0.756	0.786	0
	subject4	0.562	0.547	0.578	0
	subject5	0.579	0.564	0.594	0
inter-user	sub1-sub2	0.595	0.573	0.616	0
	sub1-sub3	0.630	0.610	0.651	0
	sub1-sub4	0.306	0.288	0.325	0
	sub1-sub5	0.301	0.282	0.320	0
	sub2-sub3	0.493	0.474	0.513	0
	sub2-sub4	0.298	0.280	0.316	0
	sub2-sub5	0.292	0.274	0.310	0
	sub3-sub4	0.397	0.380	0.415	0
	sub3-sub5	0.362	0.344	0.380	0
	sub4-sub5	0.270	0.252	0.287	1.11e–15
	overall	0.389	0.383	0.394	0

Table 3.1: Fleiss's kappa analysis for the mechano-NPS data processing pipeline. Five subjects analyzed raw mechano-NPS data taken from AP-1060 cells; each subject processed each of the five blinded raw data files three different times using the mechano-NPS data processing software. The resulting list of cell measurements was analyzed using Fleiss's kappa to quantify the inter- and intra-user agreement on whether to save or skip a given cell measurement. The kappa value is reported along with lower and upper bounds for the $95\,\%$ confidence interval. A p-value less than 0.05 indicates a rejection of the null hypothesis that the observed agreement is accidental. This analysis was performed on all cell measurements, including those identified as erroneous. Number of cells found in each observation ranged from 49–82. Reprinted with permission from [2].

			including all measurements				*excluding erroneous measurements*			
		Subject(s)	***ICC***	**lower bound**	**upper bound**	***p***	***ICC***	**lower bound**	**upper bound**	***p***
$wCDI$	intra-user	subject1	1.00	1.00	1.00	0	1.00	1.00	1.00	0
		subject2	1.00	1.00	1.00	0	1.00	1.00	1.00	0
		subject3	0.46	0.40	0.52	0	1.00	1.00	1.00	0
		subject4	-0.02	-0.08	0.05	0.673	1.00	1.00	1.00	0
		subject5	1.00	1.00	1.00	0	1.00	0.99	1.00	0
	inter-user	sub1-sub2	1.00	1.00	1.00	0	1.00	1.00	1.00	0
		sub1-sub3	-0.01	-0.12	0.09	0.596	0.96	0.95	0.97	0
		sub1-sub4	0.16	0.05	0.26	0.002	1.00	0.97	1.00	0
		sub1-sub5	0.00	-0.11	0.11	0.473	1.00	1.00	1.00	0
		sub2-sub3	-0.03	-0.13	0.08	0.684	0.97	0.96	0.98	0
		sub2-sub4	0.18	0.08	0.28	4.20e-4	1.00	1.00	1.00	0
		sub2-sub5	0.02	-0.09	0.13	0.368	1.00	1.00	1.00	0
		sub3-sub4	-0.02	-0.13	0.08	0.674	0.97	0.97	0.98	0
		sub3-sub5	0.70	0.64	0.75	0	0.97	0.96	0.97	0
		sub4-sub5	0.01	-0.10	0.11	0.459	1.00	1.00	1.00	0
		overall	0.10	0.06	0.14	1.01e-7	0.99	0.98	0.99	0
τ	intra-user	subject1	0.99	0.98	0.99	0	0.99	0.98	0.99	0
		subject2	0.92	0.90	0.93	0	0.92	0.90	0.93	0
		subject3	1.00	1.00	1.00	0	1.00	1.00	1.00	0
		subject4	0.99	0.99	0.99	0	0.95	0.94	0.96	0
		subject5	0.96	0.95	0.97	0	0.96	0.95	0.97	0
	inter-user	sub1-sub2	0.98	0.97	0.98	0	0.98	0.97	0.98	0
		sub1-sub3	0.83	0.79	0.86	0	0.82	0.79	0.86	0
		sub1-sub4	0.99	0.98	0.99	0	0.91	0.89	0.92	0
		sub1-sub5	0.90	0.88	0.92	0	0.90	0.88	0.92	0
		sub2-sub3	0.92	0.90	0.94	0	0.92	0.90	0.94	0
		sub2-sub4	0.99	0.99	1.00	0	0.97	0.96	0.97	0
		sub2-sub5	0.95	0.94	0.96	0	0.95	0.94	0.96	0
		sub3-sub4	0.99	0.99	0.99	0	0.95	0.94	0.96	0
		sub3-sub5	0.99	0.98	0.99	0	0.99	0.98	0.99	0
		sub4-sub5	0.99	0.99	0.99	0	0.97	0.97	0.98	0
		overall	0.98	0.97	0.98	0	0.94	0.93	0.95	0

Table 3.2: Intra-class correlation of cell phenotype values using the mechano-NPS data processing pipeline. All subjects' resulting measurements of the two cell phenotype values, $wCDI$ and recovery time constant τ, were analyzed to quantify the inter- and intra-user consistency of the observed values. The intra-class correlation value (ICC) is reported along with lower and upper bounds for the $95\,\%$ confidence interval. A p-value less than 0.05 indicates a rejection of the null hypothesis that $ICC = 0$. This analysis was performed both including and excluding the cell measurements that were identified as erroneous. Number of cells found in each observation ranged from 49–82. Reprinted with permission from [2].

Variable	Tolerance	Comparison	Subject(s)	% agreement, including all measurements	% agreement, excluding erroneous measurements
$wCDI$	4.30e–11	intra-user	subject1	88.9	88.9
			subject2	88.6	88.9
			subject3	87.7	88.7
			subject4	77.8	79.5
			subject5	65.1	66.4
		inter-user	sub1-sub2	75.5	75.8
			sub1-sub3	78.8	78.8
			sub1-sub4	73.3	74.9
			sub1-sub5	61.1	62.4
			sub2-sub3	81.7	81.9
			sub2-sub4	79.9	81.8
			sub2-sub5	67.3	68.8
			sub3-sub4	82.8	85.1
			sub3-sub5	69.3	71.2
			sub4-sub5	65.1	67.8
			overall	54.8	57.2
τ	5.80e–9	intra-user	subject1	84.8	84.8
			subject2	88.1	88.3
			subject3	87.7	88.7
			subject4	77.8	79.5
			subject5	60.5	61.7
		inter-user	sub1-sub2	73.1	73.3
			sub1-sub3	75.6	75.6
			sub1-sub4	69.6	71.1
			sub1-sub5	57.4	58.6
			sub2-sub3	80.6	80.8
			sub2-sub4	78.1	79.9
			sub2-sub5	64.1	65.6
			sub3-sub4	82.2	84.6
			sub3-sub5	65.5	67.4
			sub4-sub5	61.8	64.4
			overall	52.3	54.6

Table 3.3: Percentage of equivalent measured cell phenotype values using the mechano-NPS data processing pipeline. All subjects' resulting measurements of $wCDI$ and τ were analyzed to quantify the percentage of cell events ("%-agreement") in which an equivalent phenotype value was found in all observations, within the reported tolerance. This analysis was performed both including and excluding the cell measurements that were identified as erroneous. Number of cells found in each observation ranged from 49–82. Reprinted with permission from [2].

3.5 Supplemental Information

Custom MATLAB Software for Mechano-NPS Data Processing

Our semi-automatic CLI-based software for mechano-NPS data processing is available publicly at https://github.com/sohnlab/mechanoNPS_Li-et-al-2020 [71], and a newer version is also available at https://github.com/sohnlab/NPS-analysis-JOVE [72].

First, the software will perform preprocessing as described in Section 3.3.3, and an initial scan of the raw data file will be performed to identify potential cell pulses. This initial detection is based on applying user-supplied thresholds to the derivative signal. Two different thresholds are used: one to identify peaks corresponding to a cell entering or exiting reference or recovery pores, and a second (higher) threshold to identify peaks corresponding to a cell entering or exiting the contraction segment. (The distinction between detected pore peaks and detected contraction segment peaks is highlighted in the example shown in Fig. 3.5.) The initial set of user-supplied thresholds should be adjusted depending on the cell type, device design, and experimental parameters, but can be estimated by examining the derivative signal to find the usual height of peaks corresponding to cell pulses. As an example, for AP-1060 cells, we used thresholds of 2×10^{-4} and 1×10^{-3} for the pores and the contraction segment, respectively (thresholds are given in terms of $\Delta I/I$) [2].

After the initial scan, the software generates a list of potential cell pulses, and asks the user to evaluate each one. The CLI asks for user input at two different stages for each potential cell measurement (Fig. 3.6): First, the user must decide whether to save the cell pulse or to discard it if it is invalid. If the user decides to save the cell, they are then asked to confirm the two thresholds or to adjust them as needed until a valid rectangularized cell pulse is generated. When all cell pulses have been confirmed and threshold levels finalized, the software calculates the mechanical phenotyping parameters (D_{cell}, $wCDI$, δ_{deform}, and recovery time) for each cell as described in Section 3.2.

Chapter 4

Multichannel Node-Pore Sensing: Theory & Modeling

Chapters 2 and 3 have shown that NPS is a powerful platform for single-cell label-free phenotyping, as it combines the robustness of electronic sensing with the ability to measure a wide variety of cell phenotypes. However, while other RPS-based technologies have demonstrated increased throughput and versatility through multiplexing, NPS has thus far been limited to only single-channel measurements.

In this chapter, we describe a new method for multiplexing RPS measurements that takes advantage of the unique channel geometries in NPS. We first discuss the general motivation for multiplexing and review other strategies for multichannel RPS. We then describe our strategy for NPS-based multiplexing and discuss theoretical considerations for its implementation. Finally, we derive a mathematical model for cell measurements in our multichannel system and perform computational modeling to evaluate its validity. In Chapter 5, we will demonstrate the experimental implementation of this new multichannel NPS platform and characterize its performance.

4.1 Background & Motivation

Resistive-pulse sensing

As discussed in Section 2.2.1, RPS is a gold-standard method for counting and sizing cells, bacteria, and viruses [15,16]. RPS is utilized in a wide range of settings—from the hospital central laboratory where it is used to perform a rapid complete blood count, to the research laboratory where it is integrated in commercial flow cytometers for cell population analysis. RPS is particularly attractive for microfluidic cellular analysis in the research environment because it can perform single-cell measurements with relatively high throughput, can be implemented with off-the-shelf electronic parts, and is inherently label-free—reducing the time and cost of sample preparation.

As discussed in Chapters 2 and 3, in a microfluidic RPS device, cells suspended in an electrolyte solution are driven through a narrow channel while the electrical resistance is monitored. When a cell transits the channel, it causes a temporary increase in the measured resistance (*i.e.*, a resistive pulse) whose amplitude and duration indicate the cell size and transit time, respectively. The magnitude of the resistive pulse ($\Delta R/R$) is related to the volume ratio of the cell to the channel ($V_{cell}/V_{channel}$); thus, the optimal SNR and sensitivity are achieved when the volume of the channel is minimized.

Multichannel Resistive-Pulse Sensing

To maximize SNR, microfluidic RPS devices often utilize narrow channels; however, this leads to high fluidic resistance, which limits throughput. Throughput may be increased by using a higher driving pressure or a wider channel; however, the former may result in undesirable high shear stress on the cells, while the latter reduces SNR and sensitivity. Additionally, either method compresses the signal from each cell into a shorter window of time, as it transits the channel faster. This may reduce the accuracy in estimating cell size and transit time because there are fewer datapoints that can be averaged to calculate the signal amplitude and width. Moreover, some RPS-based microfluidic platforms [17,20,78] rely on accurate measurement of the cell's transit time to quantify additional cell properties—in these platforms, increased flow speed is undesirable because the cell must spend sufficient time in the channel to measure an effect.

Because of the disadvantages that arise from increasing flow speed to achieve higher throughput, Saleh [14] proposed multiplexing (*i.e.*, driving cells through several channels that are all measured simultaneously) as an alternative method to increase throughput. His original design utilized a base electrode connected to a central reservoir, with eight channels that were each monitored by a two-terminal RPS measurement (Fig. 2.2B). A variety of similar multi-aperture RPS devices were subsequently developed [79,80], but in these platforms, the number of electrode terminals increases linearly with the number of channels to be measured. The application of signal processing techniques such as frequency division multiplexing [21] and code-division multiplexing [81–83] has led to multichannel RPS designs that require fewer electrode terminals, but the acquisition hardware required for these designs is still more complex than the single resistance measurement needed for standard RPS devices.

Our goal was to develop a fundamentally different method for multiplexing RPS. Specifically, our strategy was to utilize a *single four-terminal measurement to monitor all channels simultaneously.* This would facilitate immediate multiplexing capability in any single-channel RPS platform, without the need for hardware or software modification in the data acquisition system. Additionally, such a method could be combined with multi-aperture RPS platforms such as those described in [14,79,80].

4.2 Our Approach: Multichannel Node-Pore Sensing

4.2.1 Multiplexing Through Node-Pore Channel Geometry

To measure multiple parallel channels with a single RPS measurement, a method is needed to deconvolve the signals from the individual channels. When different cell signals overlap in time (*i.e.*, coincidence events), they need to be separated in order to measure the amplitude and transit time of each. Thus, to take advantage of the higher throughput that results from multiplexing, it is necessary to resolve these coincidence events. Additionally, in some cases it may be important to determine which channel a given cell transited—*e.g.*, if the cells were sorted prior to RPS measurements, if different conditions are measured in different channels, or if the different channels have different properties.

Here, we describe a novel multiplexing strategy that addresses these requirements by taking advantage of the unique pulse sequences generated by NPS. Our method is inspired by that of Kellman *et al.* [26], who used NPS encoding, matched-filter detection (MFD), and successive interference cancellation (SIC) to perform automatic event detection and deconvolution of coincidence events in a single-channel device. Specifically, we have designed a multichannel NPS platform in which each channel is encoded with a different sequence of nodes and pores. The MFD algorithm is expanded to simultaneously search for and detect multiple possible sequences from the multiple encoded channels. Our method is advantageous over other multiplexing strategies [14,21,79–83] because of the simplicity of using a single four-terminal measurement. The number of electrodes needed does not increase with an increasing number of parallel channels; moreover, our method can be applied to any single-channel RPS platform without modifying the data acquisition system.

4.2.2 Platform Design

As shown in Fig. 4.1A, the specific sequence of nodes and pores encoded in an NPS channel results in a characteristic expected resistance signal corresponding to the geometry. Kellman *et al.* [26] introduced the strategy of encoding the NPS channel such that the expected signal corresponds to specific sequences known as Barker codes [84]. Each of the nine Barker codes exhibits optimal autocorrelation peak-to-sidelobe ratio (PSLR), making these codes ideal candidates for use in correlation-based detection algorithms such as MFD and SIC. By encoding single-channel NPS devices with these codes, Kellman *et al.* [26] achieved automatic cell pulse detection as well as the resolution of coincidence events, or instances where multiple cell transit events overlap in time.

Here, we apply a similar principle to create a device in which multiple NPS channels are each encoded with a specific sequence, and a single electrical resistance measurement is applied across all channels in parallel (Fig. 4.1B). In this case, MFD and SIC signal processing can still resolve coincidence events from cells in the same channel—but crucially, coincidence events from cells in separate channels can also be resolved.

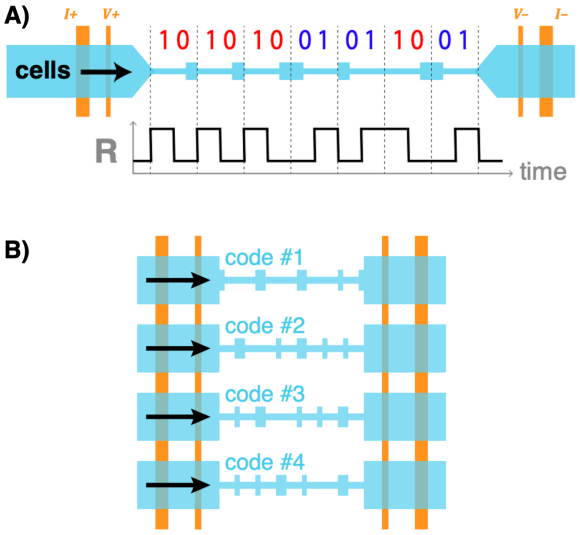

Figure 4.1: Concepts. A) Example of an NPS channel encoded with the Manchester-encoded Barker-7 sequence, and the expected resistance pulse generated by a cell transiting the channel. B) General device schematic (top-down). Four parallel NPS channels (blue) are encoded with specific sequences, while a four-terminal electrical impedance measurement is applied across all channels (electrodes in orange). Cells are suspended in an electrolyte solution and driven through the channels with a non-pulsatile pressure source (black arrows indicate flow).

Although there are an extremely limited number of Barker codes, our proposed multiplexing strategy is compatible with many different families of codes commonly utilized in digital communications (*e.g.*, [85–87]). Using alternate code families would allow each channel within the device to be encoded with a unique sequence, as shown in Fig. 4.1B, thereby making the cell's channel of origin discernible based on the shape of the signal generated when it transits the channel.

4.3 Theoretical Considerations

4.3.1 Cell Size Calculation in a Multichannel Device

In a single-channel RPS device, the cell diameter d_{cell} can be determined from the measured change in resistance ΔR compared to the baseline resistance R as follows [14,66,67]:

$$\frac{\Delta R}{R} \approx \left(\frac{d_{cell}}{L_{ch}{D_e}^2}\right)\left(\frac{1}{1-0.8\left(\frac{d_{cell}}{D_e}^3\right)}\right), \tag{4.1}$$

where L_{ch} is the channel length and D_e is the channel's effective diameter. For a multichannel RPS device with n parallel channels, we model the expected single-channel resistance of each of the parallel channels by applying Eq. 4.1 within each channel, such that $\left.\frac{\Delta R}{R}\right|_k$ gives the

change in the nth channel's resistance relative to its baseline resistance R_n due to the presence of the kth cell. We model the expected total resistance of the device $R_{measure}$ as a parallel combination of the total resistance in each of the parallel channels:

$$R_{measure} \approx \left(R_1 + R_1 \frac{\Delta R}{R}\bigg|_1 \right) \Big\| \cdots \Big\| \left(R_n + R_n \frac{\Delta R}{R}\bigg|_k \right). \tag{4.2}$$

In order to estimate cell sizes from $R_{measure}$ based on this mathematical model, each channel's baseline resistance must be known. Since it is impossible to directly measure the baseline resistance of each parallel channel in this single-measurement system, the device must be designed such that all channels have the same baseline resistance. We accomplish this by encoding all channels with bipolar sequences of equal length, which we translate into node-pore geometries through Manchester encoding [88]. By applying Manchester encoding to a bipolar code of length n, a unipolar code is generated comprising n ones and n zeros. As shown in Fig. 4.1, the ones and zeros of the unipolar code correspond to pores and nodes, respectively, in the channel. Thus, the Manchester-encoded channel's baseline resistance will be equal to $(n\,R_{node}) + (n\,R_{pore})$. Since codes of equal length are applied to all channels, and the same node and pore dimensions are used throughout (implying equal values for R_{node} and R_{pore}), all channels will have the same baseline resistance. Thus, each channel's baseline resistance can be calculated directly from the overall measured baseline resistance $R_{baseline}$ according to $R_n = n\,R_{baseline}$.

Given that R_n is known for all channels based on the measured resistance, Eq. 4.2 represents a "forward model" that predicts the measured resistance across a multichannel RPS device given a set of cells with known single-channel pulse amplitudes $\frac{\Delta R}{R}\big|_k$. Thus, to calculate cell size based on a multichannel measurement, we substitute this nonlinear forward model for the simple linear forward model in the cell detection algorithm utilized by [26]. The data processing software will fit $\frac{\Delta R}{R}\big|_k$ for each detected cell, and Eq. 4.1 can then be used to calculate the cell's diameter.

4.3.2 SNR Tradeoff with Increased Multiplexing

Because $\Delta R/R \sim V_{cell}/V_{total}$, we expect that each additional parallel channel will cause a significant reduction in the SNR, and in turn, a reduction in the device's sensitivity. To quantify this tradeoff between increased throughput and reduced sensitivity, we modeled the predicted relationship between SNR, cell size, and number of parallel channels. We performed this analysis in the domain of electrical current (rather than resistance) because our NPS data acquisition system applies a constant voltage across the device while measuring the current.

SNR is defined as the ratio of squared amplitude to noise variance. In RPS, the signal amplitude depends on the cell size, device geometry, and baseline resistance. Thus, to model the signal amplitude, we applied Eq. 4.1 along with the approximation that $\Delta R/R \approx$

$\Delta I/I$ [67], yielding:

$$\Delta I \;\approx\; I_b \left(\frac{k_1 \; {d_{cell}}^3}{1 - k_2 \; {d_{cell}}^3} \right), \tag{4.3}$$

where ΔI is the current-pulse amplitude, I_b is the single-channel baseline current, and k_1 and k_2 are constants that depend on the channel dimensions. Even with multiple parallel channels, the observed total measured current-pulse amplitude will be equal to the single-channel current-pulse amplitude ΔI given by Eq. 4.3, since currents in parallel channels add. Specifically, when one cell is present in a device with n parallel channels,

$$I_{measured} = (I_{b,1} - \Delta I) \;+\; I_{b,2} \;+\; \cdots \;+\; I_{b,n}, \tag{4.4}$$

where $I_{measured}$ is the overall measured current across all parallel channels, $I_{b,n}$ is the nth channel's baseline current, and ΔI indicates the magnitude of the current drop within the single channel that contains the cell (given by Eq. 4.3). Since all the parallel channels have an equal baseline current (*i.e.*, an equal baseline resistance, as discussed above), then $I_{b,n}$ is equal to the overall measured baseline current $I_{b,tot}$ divided by n, and Eq. 4.4 simplifies to $I_{measured} = I_{b,tot} - \Delta I$.

To model the noise variance, we examined past data from NPS devices of varying geometries and observed that the standard deviation of the current noise scales approximately linearly with the total internal volume of the device (data not shown). Since all of the channels will have equal volumes due to the considerations discussed in Section 4.3.1 with regard to baseline resistance, the total volume of the device will scale linearly with the number of channels. Therefore, we modeled the noise as $\sigma(I) \;\approx\; k_3 + k_4\, n$, where k_3 and k_4 are constants.

Thus, the resulting model for SNR as a function of cell diameter and number of parallel channels reduces to:

$$SNR = \left[\frac{\Delta I}{\sigma(I)} \right]^2 \approx \left[\left(\frac{k_1 \; {d_{cell}}^3}{1 - k_2 \; {d_{cell}}^3} \right) \left(\frac{I_{b,1}}{k_3 + k_4\, n} \right) \right]^2. \tag{4.5}$$

For a given device geometry, k_2, k_3, k_4, and $I_{b,1}$ will be constant—no matter the number of channels. Ergo, this model predicts that the SNR for a given channel geometry and cell size scales with $1/\,(1 + k\, n)^2$, where k is a constant. We will compare this model to experimental data in Chapter 5.

4.4 Computational Modeling

Having derived a mathematical model for the relationship between cell size and measured resistance in a multichannel RPS system, we tested its validity through computational modeling. We simulated the resistance that would be measured when one or more cells of different sizes transit through a four-channel device, and we compared the simulated results with our theoretical predictions.

4.4.1 Methods

Finite-element simulations were performed using Comsol Multiphysics (Version 5.3a). A model was created with four parallel channels (Fig. 4.2A), each encoded with the Barker-7 sequence (Fig. 4.1A). Cells were modeled as spheres with electrical conductivity $\sigma = 1 \times 10^{-10}$ S/m and relative permittivity $\epsilon_r = 2.55$. PBS was defined as a liquid with $\sigma = 1.75$ S/m and $\epsilon_r = 80$. A tetrahedral mesh was generated using a minimum element size of 0.01 µm and a maximum element size of 230 µm.

RPS measurements were simulated using the Comsol AC/DC Module. The outer electrodes were modeled as constant-voltage terminals with 1 V at the first electrode and 0 V at the last electrode. The inner electrodes were modeled as floating terminals. The voltage and current were measured at each terminal, and the resistance across the device was calculated using Ohm's Law.

The device was simulated using a range of configurations with cell(s) placed in the middle of one or more channels. Each configuration was simulated with the cell diameter(s) ranging from 1–19 µm. The simulated resistance for a given combination of cell sizes was calculated by averaging the simulated device resistance across each possible arrangement of the cells within the four channels.

4.4.2 Results and Discussion

We compared the results of our simulation to our mathematical model that describes the relationship between cell sizes present and total measured resistance (Section 4.3.1). We first considered the case of a single cell present in just one of channels. For all single-cell configurations, we calculated the cell size that would be extracted based on our mathematical model (Eq. 4.1–4.2), where $R_{measure}$ was the simulated resistance. As shown in Fig. 4.2C, we found good agreement ($R^2 = 0.9996$) between the predicted size and the true size of the simulated cell.

We also evaluated the magnitude of error in the predicted resistance according to our mathematical model compared to the simulated resistance for all single- and multi-cell configurations (Fig. 4.2D). Some configurations do exhibit a high degree of relative error in the model for ΔR when small cells are present. For example, errors >45% occur in some cases when cell(s) <7 µm are present, and errors >10% occur in some cases when cell(s) <9 µm are present. However, if we only consider configurations in which all cells are at least 10 µm in diameter, the error for nearly all configurations is <5% (and the median errors are all <2%). The correlation between smaller cell sizes and larger model error may partially be a result of the limitations of finite-element modeling with small feature sizes, and/or to the limitations of Eq. 4.1 when the cell is very small compared to the channel.

In practical use cases, as discussed in Section 4.1, RPS devices are usually designed to minimize the channel volume. Thus, the pore width is chosen to be as narrow as possible without constricting the cells. Specifically, a device with our simulated dimensions (pore width 20 µm) would typically be used for measuring cell populations with expected diame-

ters well above 10 µm. Therefore, for the expected use cases, our simulations exhibit good agreement with our mathematical model and confirm its validity for estimating cell sizes in a multichannel RPS configuration.

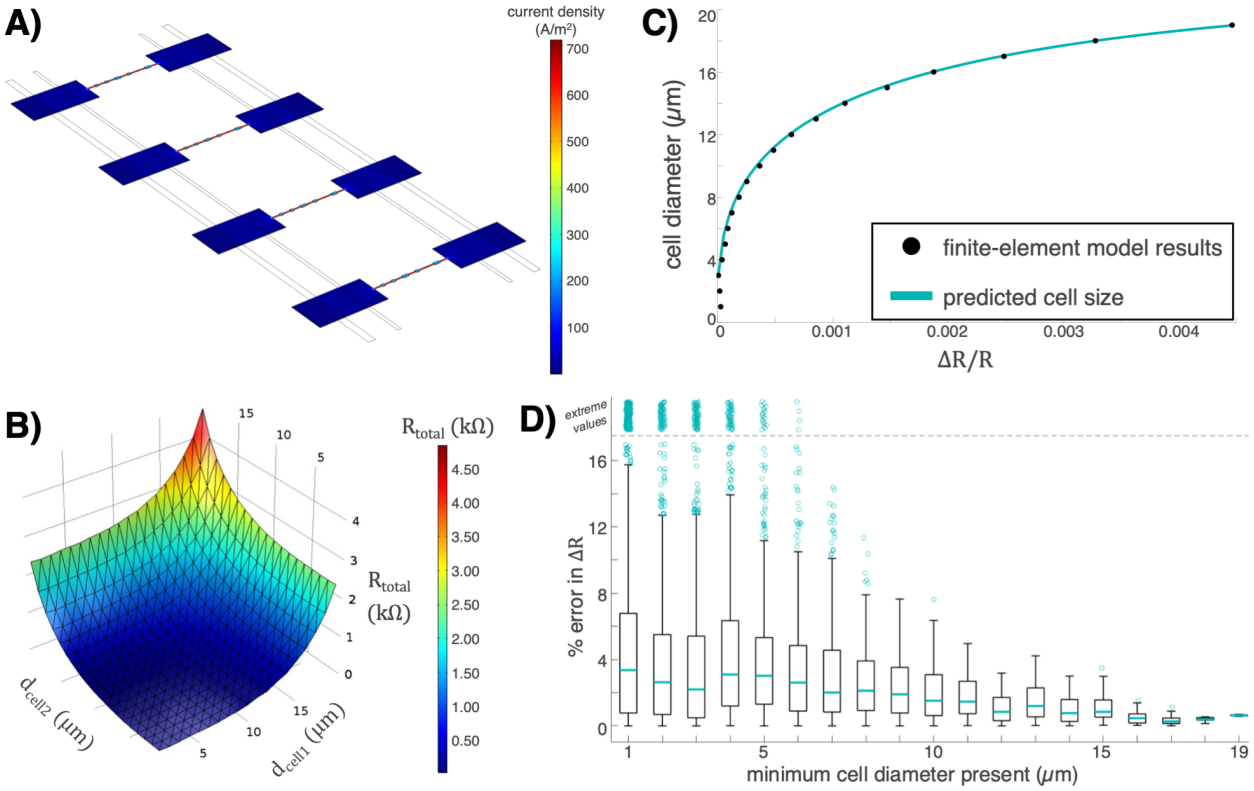

Figure 4.2: Finite-element simulations. A finite-element model of a four-channel device, in which each channel was encoded with the Barker-7 sequence, was computed with configurations ranging from 0–4 cells across a range of diameters to simulate the measured resistance. A) The simulated four-channel device. Simulated current density is shown (in the middle plane of the channel) when no cells are present. B) Simulated resistance when two cells are present in different channels, across a range of cell sizes. C) Simulation data (black circles) for single-cell configurations, showing the diameter of the modeled cell and the simulated $\Delta R/R$. Teal curve shows the predicted cell size based on the measured resistance according to our mathematical model. $R^2 = 0.9996$ for the predicted cell sizes compared to the simulation results. D) Error magnitudes in the predicted resistance based on our mathematical model compared to the simulation results, for all model configurations. Datapoints are grouped according to the size of the smallest cell present in the configuration. Medians are represented by teal lines; interquartile ranges are represented by black boxes; outliers are represented by teal circles and are defined as 1.5 times the interquartile range. Extreme values are represented as teal circles placed above the dashed line and are defined as values greater than $45\,\%$.

4.5 Conclusions

In this chapter, we have described a novel method for multiplexed RPS that takes advantage of the spatiotemporal encoding in the NPS channel geometry. This approach is unique among other strategies for multichannel RPS in that it does not require additional electrodes to measure more than one channel and requires no modification to the data acquisition hardware used for standard single-channel RPS measurements. This makes our multiplexing method widely accessible to any facility already equipped with standard RPS instrumentation.

As we have described, our platform design encodes each channel with specific geometries that enable an algorithm based on MFD and SIC to detect multiple cell pulses and deconvolve coincidence events. We have developed a mathematical model to relate the size of cells present in each channel to the total measured resistance. This model can be applied in the event detection algorithm to fit equivalent single-channel pulse amplitudes for each detected cell, from which the cell size can be calculated. Additionally, we used our mathematical model to derive a prediction for the tradeoff in SNR as the number of parallel channels increases for this multichannel platform. Finally, we used finite-element simulations to evaluate the accuracy of our mathematical model as it applies to calculating cell size based on the total measured resistance.

Chapter 5

Multichannel Node-Pore Sensing: Implementation & Characterization

In Chapter 4, we established the theoretical basis for a novel method of multiplexed RPS that is based on NPS, and we derived a mathematical model for how this system would perform. In this chapter, we implement and validate three new device designs based on these principles, thereby demonstrating multichannel NPS measurements for the first time. We apply the mathematical model derived in Chapter 4 to improve our automatic cell detection algorithm and to provide accurate calculations of cell diameters in this multichannel platform. We also experimentally quantify the tradeoff between SNR and number of parallel channels and compare these results to our theoretical predictions in Chapter 4.

5.1 Introduction

As discussed in Chapter 4, we developed the framework for an NPS-based platform that is capable of performing simultaneous measurements in multiple parallel channels. As described in Section 4.2, we took advantage of the unique pulse sequences generated by NPS devices to encode specific sequences within each channel's geometry. Furthermore, we described how this encoding could enable automatic event detection and deconvolution of coincidence events through MFD and SIC, and we proposed that differentiation between channels could be accomplished by encoding different channels with different sequences. Our approach is advantageous over other multiplexing strategies because it does not require additional electrodes to measure more than one channel and can be used with any existing single-channel RPS data acquisition platform, including the existing NPS data acquisition hardware that has been implemented in multiple laboratories to date [2].

5.2 Three Novel Designs for Multichannel Node-Pore-Sensing

Previously, Kellman *et al.* [26] utilized a single-channel NPS device encoded with a Barker sequence [84] and applied MFD and SIC signal processing to resolve coincidence events in that channel. Here, we apply this same principle to multichannel NPS. We encode each channel with a specific code and apply a similar computational strategy to resolve coincidence events within the same channel (as before), but also between separate channels. Fig. 4.1A depicts how the channel geometry corresponds to the resulting resistance signal. Fig. 5.1A shows a schematic of the generalized device design.

The Barker sequences with which Kellman's channels were encoded [26] are ideal for MFD-based detection because they have ideal autocorrelation PSLR. For our multichannel platform, however, we wanted the ability to distinguish which channel each detected cell passed through. This requires each channel to be encoded with a different sequence, such that the cell's channel of origin can be determined based on the specific shape of its resistance signal. Barker sequences would be insufficient in this case because there are only nine known Barker sequences, and there is only one Barker sequence for a given length (for code lengths greater than four) [84]. Thus, we initially explored the idea of encoding some channels with a Barker sequence and other channels with its inverse (*i.e.*, with 1's and 0's swapped). This would provide some specificity about each cell's channel of origin, but it would not allow us to distinguish between more than two channels or groups of channels. Therefore, we also explored encoding the channels with codes other than Barker sequences. Using larger code families would enable us to create a device with more than two channels. Specifically, each channel would be encoded with a unique code, thereby allowing us to determine the exact channel a cell transited.

Based on these ideas, we designed three different devices, each with four parallel encoded channels (Fig. 5.1). In our first design, "B7-reg", we applied the Barker sequence of length 7 to all channels. Following the strategy used in [26], we converted the binary Barker sequence to a unipolar signal that could be encoded in the NPS signal through Manchester encoding [88] (we denote the Manchester-encoded Barker-7 sequence as "MB7"). In our second design, "B7-inv", we applied the MB7 code to two of the four channels, and its inverse ("MB7inv") to the other two channels. In our final design, "four-codes", we applied four unique length-7 Manchester codes ("codes A–D"), which we chose through combinatorial optimization (described in Section 5.4.1). All codes used in these designs are listed in Fig. 5.1C. Each unipolar code was translated into a sequence of nodes and pores by representing each "1" as a pore of length 180 µm and width 20 µm, and each "0" as a node of length 60 µm and width 60 µm (Fig. 4.1A). We predicted that the B7-reg design would demonstrate the most accurate event detection performance due to the ideal properties of the Barker sequence. On the other hand, we predicted that the increased number of encoded sequences in the four-codes design would increase the cross-correlation between channels, thereby leading to a higher probability of false or misclassified event detections.

A)

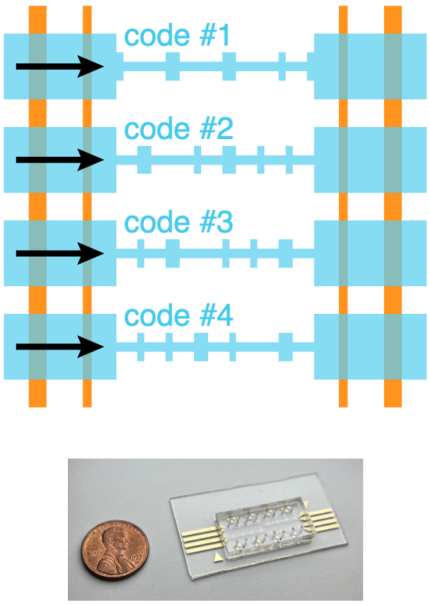

B)

	B7-reg	B7-inv	four-codes
code #1	MB7	MB7	code A
code #2	MB7	MB7	code B
code #3	MB7	MB7-inv	code C
code #4	MB7	MB7-inv	code D

C)

name	code
MB7	1 0 1 0 1 0 0 1 0 1 1 0 0 1
MB7-inv	0 1 0 1 0 1 1 0 1 0 0 1 1 0
code A	0 1 1 0 0 1 1 0 0 1 1 0 1 0
code B	1 0 0 1 1 0 1 0 0 1 0 1 0 1
code C	1 0 1 0 0 1 1 0 1 0 1 0 0 1
code D	1 0 1 0 1 0 0 1 0 1 1 0 0 1

Figure 5.1: Multichannel device designs. A) Top: General device schematic (top-down). Four parallel NPS channels (blue) are encoded with specific sequences, while a four-terminal electrical impedance measurement is applied across all channels (electrodes in orange). Cells are suspended in an electrolyte solution and driven through the channels with a non-pulsatile pressure source (black arrows indicate flow). Bottom: Photo of a completed microfluidic chip containing two devices side-by-side. B) Codes used in each of the channels for each device design. C) List of codes used in NPS channels.

5.3 Experimental Methods

5.3.1 Device Fabrication

Devices were fabricated as described in Section 3.3.1. Briefly, platinum electrodes and gold contact pads were prefabricated onto a glass substrate using standard photolithography and electron-gun evaporation. A negative-relief master mold for the microchannel structures was fabricated using SU-8 3010 epoxy photoresist and standard photolithography (spin speed 1200 rpm, exposure energy 280 $\mathrm{mJ/cm^2}$); the resulting feature height was 20.34 ± 0.08 µm. PDMS channel structures were then molded from the negative-relief master and bonded to the glass substrate with the prefabricated electrodes via oxygen plasma treatment.

5.3.2 Cell Culture

MDA-MB-231 cells (ATCC) were cultured in a 1:1 ratio of DMEM:RPMI-1640 with 10 % FBS and 1X Penicillin-Streptomycin. Cell culture was maintained at 37 °C in 5 % CO_2, and cells were routinely passaged once they reached 80 % confluence. To passage, cells were dissociated by incubation in 0.25 % trypsin/EDTA for 5 min at 37 °C, followed by trypsin neutralization with culture media at a ratio of 2:1 by volume. The cells were then centrifuged at 0.2 rcf for 5 min and re-seeded at a ratio of 1:4 or 1:2. For all experiments, cells were used before passage 20.

5.3.3 NPS Measurements

Cells were dissociated via trypsin treatment as described above, washed with 1X PBS, and then suspended at a concentration of 3–5 $\times$ 10^5 cells/mL in 1X PBS supplemented with 2 % FBS. The cell suspension was subsequently filtered using a 30 µm strainer to remove large clumps of cells. For cell-size reference measurements, the cells were sampled using a Scepter 2.0 Handheld Automatic Cell Counter (Millipore Sigma) with a 60 µm tip.

NPS measurements were performed as previously described [24], and as detailed in Section 3.3.2. Briefly, the cell suspension was injected into the inlet of each channel, and a non-pulsatile pressure of 15 mbar (Elveflow, Fluigent) was applied to drive cells through each channel. A four-terminal measurement was performed to monitor the electrical current across the device while a constant voltage (3–4 V) was applied. The resulting current was amplified by a current-to-voltage converter and measured by a commercial data acquisition device (National Instruments). The data was acquired using custom MATLAB software [69].

The effective channel diameter D_e for each device was estimated empirically by measuring a sample of cells using both the NPS device and the Millipore Scepter for reference. After processing data for this calibration sample as described below, the value of D_e was chosen to match the peak value of the NPS-measured cell size distribution with the reference size distribution.

5.4 Computational Methods

To automatically detect cell events and deconvolve the signal from parallel channels, we designed and implemented a detection algorithm based on MFD and SIC. Although based on the same framework as [26], our algorithm differs in two notable ways. First, we added support for simultaneous detection of multiple encoded sequences. Second, we implemented a parametric forward model (detailed in Section 4.3) to capture the nonlinear behavior caused by the resistance signals from each channel combining in parallel. An overview of our data processing pipeline is described in Sections 5.4.2–5.4.4, and the detailed algorithm is provided in Section 5.7.2.

5.4.1 Code Generation for Four-Codes Device Design

Because the mixture of signals from the different channels are separated using MFD, which is a cross-correlation-based detector, one figure of merit for predicting the performance of a code set is the maximum side-lobe, or maximum off-center cross-correlation between all pairs of codes in the set. Previous methods such as [81] utilized Gold codes [85] for their ability to generate large families of nearly-orthogonal codes, with low autocorrelation and cross-correlation side-lobes. However, Gold codes, as well as other nearly-orthogonal codes used in digital communications (*e.g.*, Kasami codes [86]) are cyclic codes, which assume periodic cross-correlation [87]. In our case, we desired a set of codes with good *aperiodic* cross-correlations. To produce such a set, we employed a combinatorial optimization method (detailed in Section 5.7.1). In short, we generated all possible codes of length 7, computed the maximum zero-mean aperiodic cross-correlation between all code pairs, and identified the optimal set of four codes.

5.4.2 Overview of Data Processing

Custom MATLAB software was used to analyze all NPS data [89] (Fig. 5.2). The acquired resistance data was preprocessed to remove noise, fit to a baseline resistance signal, and then partitioned into short "frames" for independent analysis. A filter bank, comprising a variety of signal templates across a range of transit times for all encoded sequences in the device design, was also generated. This filter bank was then applied in an algorithm based on MFD and SIC to detect cell transit events within each data frame and to subsequently estimate the parameters of each event. Based on these parameters, each cell's transit time and size were determined.

5.4.3 Data Preprocessing

The recorded current signal was first transformed into a resistance signal by applying Ohm's Law. Low-pass filtering was then applied to remove high-frequency noise. The time-varying baseline resistance was estimated using a weighted least-squares method with a second-difference smoothing penalty, adapted from [70]. Weights were determined using an envelope estimator detailed in Section 5.7.2. The output of this window estimator also identified sections of data as either "possible-cells" (*i.e.*, cell transit events may be present) or as "noise-only" (*i.e.*, no cells are present in that section).

To increase the efficiency of the SIC-based event detection algorithm, the resistance signal was divided into short frames that were each analyzed independently. Using the output of the envelope estimator, the software performed this segmentation while ensuring that each potential transit event was fully encompassed within a single frame (*i.e.*, no frame contained partial transit events).

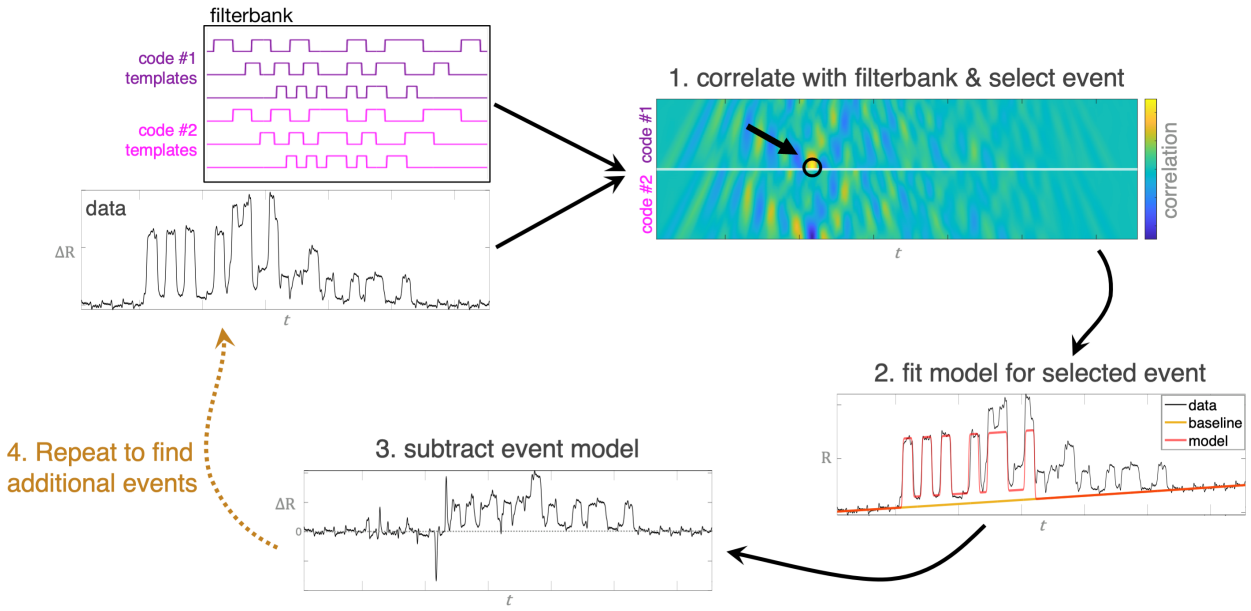

Figure 5.2: Data processing pipeline using MFD and SIC. A filter bank is generated containing templates for each code present in the device; each template is scaled to a range of possible transit times. Each scaled template within the filter bank is correlated with the preprocessed data to generate a correlation map (1), and a candidate event is identified. The location of the candidate event within the filter bank identifies the event's code, estimated transit time, and estimated time of occurrence. The forward model is then applied to generate a fitted model for the candidate event (2). When the fitted model is subtracted from the original data (3), the event detection and model fitting process can be repeated (4).

5.4.4 Event Detection and Parameter Estimation

We employed an algorithm based on MFD (Fig. 5.2) to automatically detect cell transit events and estimate their parameters (including code identity, pulse amplitude, and transit time). This strategy deconvolves the signals from each parallel channel and resolves coincidence events within the same channel and across multiple channels. The general structure of the pipeline follows a greedy SIC algorithm similar to that used in [26], but with significant modifications, most notably to the data-fitting subroutine used during the SIC step. Additionally, we added support for simultaneous detection of multiple encoded sequences and developed a parametric forward model to handle nonlinear parallel resistance combinations.

First, a filter bank is generated containing zero-mean versions of signal templates (based on the designed codes utilized in each channel), scaled to a range of transit times. Then, each frame is analyzed independently using the algorithm described below to detect cell transit events. (Event detection was not performed on frames previously identified as "noise-only.")

As shown in Fig. 5.2, the frame's resistance signal is passed through the pre-generated filter bank, and a candidate cell pulse is identified based on the resulting correlations. Pa-

rameters for all events detected so far (*e.g.*, amplitude) are estimated by applying a forward model and fitting it to the data as closely as possible. This fitted model is subtracted from the resistance signal to cancel out the pulse's contribution from any other potentially overlapping events. This allows the remaining residual data to be passed through the filter bank again, and the process is repeated to find the next pulse until no more valid events are found.

In a typical SIC process, in the model-fitting step (step #2 in Fig. 5.2), only a simple linear model is fit to estimate the pulse amplitude. This strategy speeds up computation time, but results in poorer model fit because only a course estimate is known for the pulse's center time and transit time. Poor model fit during SIC results in poor signal cancellation when the model is subtracted from the rest of data, and we observed that this mismatch often resulted in incorrect or false event detections. Thus, we implemented a more sophisticated parametric forward model that better reflects the NPS data, which resulted in noticeable improvements in the performance of this event detection algorithm (as demonstrated in Fig. 5.3). The details of our modified SIC algorithm, along with details of the pulse parameters estimated by the forward model fit, are described in Section 5.7.2.

When the SIC process is complete and no more cell pulses remain within the data frame, a final model fit is performed to jointly estimate the parameters of all detected pulses. This step utilizes the same nonlinear forward model as our modified SIC process. Importantly, this model inherently accounts for the parallel combination of the resistance signals from each channel by applying Eq. 4.2, and the single-channel pulse amplitude ΔR_k is fitted for each event. Thus, for each detected event, the single-channel $\left.\frac{\Delta R}{R}\right|_k$ due to the presence of the cell is inferred, and Eq. 4.1 can be directly applied to calculate the cell's diameter.

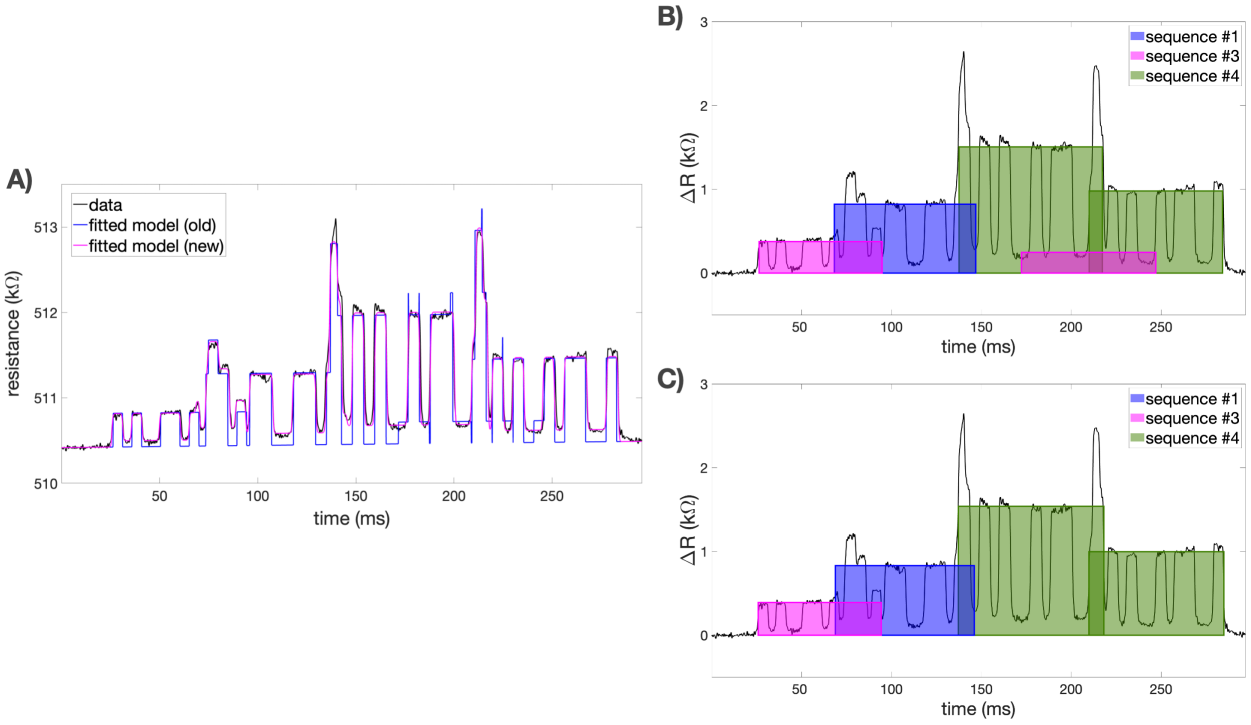

Figure 5.3: Comparison of SIC pulse detection performance between a simple forward model fit and our updated, fully parametric model. A representative frame of data taken from a four-codes device was processed with our pulse detection and estimation algorithm, but with different forward models. We tested the performance with 1) a simple linear model that only attempts to fit the pulse height, and 2) our fully parametric nonlinear model, and we evaluated the results. A) The final fitted results after pulse detection estimation with our SIC algorithm. The simple (old) model fit is show in blue, and exhibits significantly more mismatch with the data compared to the full (new) model, shown in pink. B) The final pulse detections from running the algorithm with the simple (old) model. Rectangles indicate locations where a pulse was detected, and their dimensions indicate the fitted amplitude and transit time. In this case, a false pulse (right-most pink rectangle) was detected due to poor model fit during SIC. C) The final pulse detections from running the algorithm with our full (new) model. The falsely-identified pulse from B) was not detected with this updated forward model.

5.5 Results & Discussion

5.5.1 Proof-of-Concept with Three Device Designs

Fig. 5.4B shows the distribution of measured cell diameters in each of the three device designs, separated by the detected code. Results from all designs show good agreement with the expected cell diameter of ∼15 µm (Table 5.1). As shown, the B7-reg and B7-inv designs cannot identify exactly which channel the cell passed through, while the four-codes design can identify each cell's channel by the detected code. However, the increased number of encoded sequences in the four-codes design does increase the cross-correlations between channels, which could lead to a higher probability of false or misclassified cell detections. It's possible that this potentially higher error rate could account for the increased standard deviation in detected cell diameters for the four-codes design compared to the other designs (see Table 5.1), but further experiments are needed to fully investigate this result.

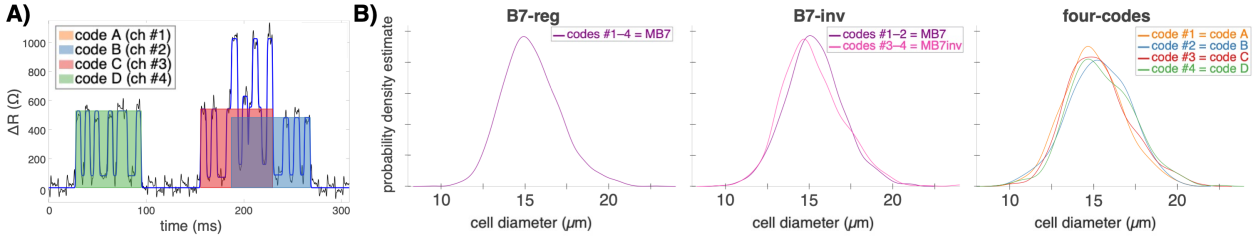

Figure 5.4: Proof-of-concept experiment. A) Examples of detected cell pulses from a four-codes device. Data (black) shows measured resistance pulse amplitude, and the fitted model for all detected events is shown in blue. Rectangles show cell events detected by the data analysis software; width indicates cell transit time, height indicates pulse amplitude, and color indicates the code. B) Probability density estimates of measured cell diameters in each device design. Cell data is grouped by the detected code (*i.e.*, which channel the cell passed through). $n = 1302$ for each device type.

device type	**mean cell diameter** (µm)	**standard deviation** (µm)
B7-reg	15.35	1.77
B7-inv	15.27	1.78
four-codes	15.34	1.89

Table 5.1: Summary of cell diameters measured in each device type.

5.5.2 Evaluating the Tradeoff in Signal-Noise Ratio with Increased Multiplexing

To experimentally evaluate the tradeoff in SNR with increasing numbers of channels, we measured cells using B7-reg devices with one or more parallel channels. While cells transited through one of the channels, a solution with no cells flowed through all other channels. We performed data processing to detect cell transit events, and we calculated the diameter and SNR for each detected cell, where SNR is defined as the ratio of squared amplitude to noise variance in the preprocessed current signal. The noise variance for each cell event was estimated using a 10 s window (excluding data points where cell events were detected).

According to the mathematical model described in Section 4.3.2 and given that all parallel channels are identical, we modeled SNR as a function of cell diameter using the following equation, which is obtained by simplifying Eq. 4.5:

$$SNR = \frac{(\Delta I)^2}{\sigma^2(I)} \approx \left(\frac{k_1 \; {d_{cell}}^3}{1 - k_2 \; {d_{cell}}^3} \right)^2 , \tag{5.1}$$

where ΔI and $\sigma^2(I)$ are the pulse amplitude and noise variance in the preprocessed current signal, d_{cell} is the diameter of the cell, k_1 is a constant that varies with the number of channels, and k_2 is a constant that is independent of the number of channels.

For each channel configuration tested, a nonlinear fit was performed with Eq. 5.1 to determine k_1. A single value for k_2 (5.8257×10^{-5}) was fitted empirically across all conditions. The data and fitted curves are shown in Fig. 5.5A. As expected, the SNR for a given cell size decreases with increasing numbers of parallel channels.

To examine the relationship between SNR and the number of channels, we compared the ${k_1}^2$ values (proportional to SNR in our model) as n increased from 1–4 (Fig. 5.5B). Since our model predicted $k_1 \sim 1/(1 + b\,n^2)$, we fit a curve of this form to our results and found fair agreement with the observed data ($b = 4.606$, $R^2 = 0.9536$). The experimental results do present a lower value of k_1 for the four-channel configuration than predicted by the curve, indicating a lower SNR than would be expected based on the other conditions. However, a lower preamplifier sensitivity setting was required in this condition in order to avoid data clipping, so we hypothesize that noise introduced by the preamplifier depends on the sensitivity setting and was a confounding factor in this condition.

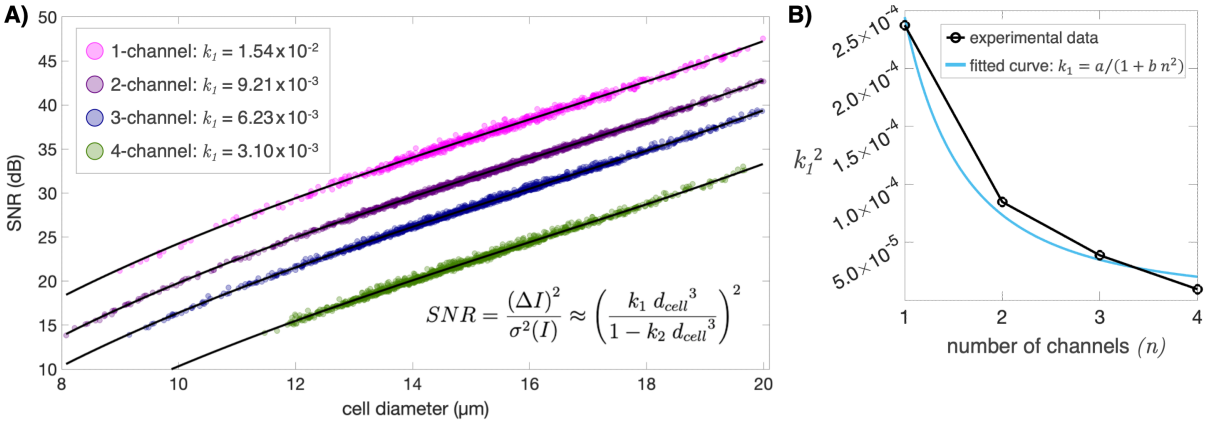

Figure 5.5: SNR experiment. Cells were measured on B7-reg devices with one or more parallel channels. A) Data (filled circles) were processed to calculate cell diameter and SNR (expressed in dB). A nonlinear fit (black curves) was performed using Eq. 5.1 to find k_1 for each device type. k_2 was fitted empirically to a single value (5.8257×10^{-5}) for all conditions. $n_1 = 754$; $n_2 = 1700$; $n_3 = 1657$; $n_4 = 1327$. B) The value of ${k_1}^2$ (which is modeled as proportional to SNR) decreases as the number of parallel channels increases. Experimental values are shown in black. A curve modeling k_1 as proportional to $1/(1 + b\,n^2)$ (where b is a constant) is shown in blue ($R^2 = 0.9536$).

5.6 Conclusions

We have demonstrated and validated a novel method for multiplexed RPS that enables automatic deconvolution of signals from parallel channels. Our strategy is based on encoding NPS channels with specific sequences that enable simultaneous measurements in multiple channels with a single measurement. We implemented this method in three novel device designs, demonstrating four-channel NPS measurements for the first time. We also quantified the tradeoff in SNR with increasing numbers of channels for this method.

Our approach is versatile because it requires no additional electrodes or acquisition hardware, unlike other RPS multiplexing strategies, and it can be used with any existing RPS data acquisition platform. Our B7-reg and B7-inv designs are best when it is not important to distinguish exactly which channel each cell passed through, while our four-codes design is best suited for applications when it is important to distinguish the cells' channel of origin (*e.g.*, if the channels have different properties or if the cells were sorted beforehand). Any of these designs can be scaled up to higher numbers of channels, as long as the SNR and sensitivity remain sufficient for the application.

These new multichannel designs can be readily adapted to measure cell surface markers or mechanical properties as previously demonstrated in single-channel NPS devices [17,20,90]. Adding multiplexing capability to this platform not only increases the throughput, but also opens up the possibility of a variety of integrated device designs. For example, a mixed sample could be sorted based on size, and then each cell type could be measured for the

relevant surface biomarkers. In mechanical phenotyping devices, sorting cells by size before performing the measurement would enable the channel width to be scaled to the cell size, equalizing the strain applied to all cells in a mixed population.

Overall, this novel method of multiplexing enables any researcher to immediately increase their RPS device's throughput by measuring two or more channels in parallel. This method could even be applied to platforms that already employ multiplexing through separate electrical measurements, further multiplying their throughput. The flexibility of our technique, along with the overall versatility of NPS, could enable the next generation of electrical cell sensing platforms with a wide variety of applications.

5.7 Supplemental Information

5.7.1 Combinatorial Optimization of Four-Codes Design

The example provided here generates the optimal set of codes for a four-channel device with code sequence length 7. However, this method is applicable to any desired number of channels or code length.

1. For a code of length 7, generate all 2^7 binary codes.
2. Convert all binary codes into unipolar codes through Manchester encoding.
3. Choose two codes and compute the zero-mean aperiodic cross-correlation between them. Record the maximum side-lobe value in a matrix (of size $2^7 \times 2^7$).
4. Repeat step 3 for all $(2^7)^2 = 2{,}097{,}152$ code pairs to fill in the matrix.
5. For a code set of size 4, iteratively prune away the row and column containing the largest maximum side-lobe value until only a 4×4 sub-matrix remains. The remaining indices represent the optimal size-4 code set.

We utilized this method to generate four identical codes ("codes A–D") that we applied to the four-codes device design. The codes themselves are listed in Fig. 5.1C, along with the "MB7" and "MB7inv" codes applied to the B7-reg and B7-inv designs.

5.7.2 Event Detection and Parameter Estimation Algorithm

Baseline Fitting and Envelope Estimator

The time-varying baseline resistance was estimated using a weighted least-squares method with a second-difference smoothing penalty, adapted from [70]. Weights were determined using an envelope estimator consisting of a sliding window max-hold filter and a sliding window min-hold filter. Sections of data in which the difference between the max-hold and min-hold exceeded a threshold were identified as potentially containing cell transit events ("possible-cells"); all other sections were identified as "noise-only." "Possible-cells" sections were excluded from the baseline estimation by setting their weights to zero. The threshold

for the signal envelope was automatically determined using the Kneedle algorithm [91] to find the positive "elbow" in its quantile-quantile plot against the standard normal distribution.

Automatic, Safe Frame Partitioning

Using outputs from the envelope estimator applied during baseline fitting, the data was dynamically partitioned to ensure that (1) all divisions between frames occurred within "noise-only" sections, and (2) all frames containing "possible-cells" sections exceeded the minimum duration required to perform MFD. All frames containing "possible-cells" sections were set to the minimum duration allowable according to these constraints to ensure reasonable computation time for cell event detection.

Pulse Detection Through Modified Successive Interference Cancellation

1. The frame's baseline-subtracted resistance data is passed through the filter bank. Both the ordinary cross-correlation and normalized cross-correlation [92,93] values are computed, which populate two cross-correlation maps: one ordinary and one normalized. The two axes of each map represent the signal template index from the filter bank (corresponding to code identity and transit time) and the timestamp within the frame.
2. The peak value of the ordinary cross-correlation map is selected as a candidate detection.
3. The PSLR of the candidate detection is estimated from the peak value and its surrounding values and compared to a user-defined threshold. If the estimated PSLR is below the threshold, the peak and its immediate neighbors (main lobe) are disqualified as candidate detections, and the next-largest peak value is selected as the next candidate.
4. If the PSLR threshold is exceeded, then the normalized cross-correlation value is compared to a user-defined threshold. If this threshold is also exceeded, then the candidate is marked as a detected event.
5. Following the overall SIC algorithm, the next step is to attempt to cancel the contribution of the detected event(s) from the remainder of the data frame. At this point, the approximate center time of the last detected transit event and a coarse estimate of its transit time are known. These two parameters (plus the parameters for all previously detected events in the frame) are used as a starting point in a model-based data fitting subroutine (described in the following section), which produces a higher-fidelity prediction of the contribution of the detected event(s) to the data frame.
6. The prediction is subtracted from the data frame, and the residual re-enters the filter bank. This SIC process (steps 1–5) repeats until the predicted amplitude of the latest candidate detection falls below a user-defined threshold or the number of SIC iterations exceeds a user-defined maximum.
7. After the iterative SIC process terminates, the model prediction undergoes a pruning step to remove false detections. Each detected event is removed one at a time and the

model parameters are refit. If the prediction error does not increase beyond a user-defined limit, the detected event that has the smallest contribution to the prediction is discarded. This process is repeated until removing any detected event would increase the prediction error beyond the limit.

Data Fitting Subroutine and Forward Model

The data fitting subroutine utilizes a nonlinear parametric forward model. The forward model takes a variable number of detection events, each with a code identity, a parallel channel number, and a set of continuous-valued parameters describing its precise signal shape. It then generates a continuous-time representation of every transit event (*i.e.*, the event's contribution to the time-varying single-channel resistance) and computes the overall device resistance from the individual resistance signals. Resistances in the same channel are electrically in series and thus, add together. Meanwhile, the channels themselves are electrically in parallel, so their resistances are combined using the parallel resistance equation.

When an event is detected within a frame using MFD, the location of the peak value in the cross-correlation map represents discretized estimates of the center time and transit time of the event. These two parameters are not adequate to make a high-fidelity prediction of the event's contribution to the observed data for two reasons: (1) in reality, the center time and transit time are continuous-valued, and (2) there is significant model mismatch between the idealized signal templates and the observed shape of a transit event in an NPS experiment. Therefore, additional shape parameters are introduced to the forward model as follows:

Besides code identity and channel number, each transit event has six parameters: (1) center time (the timestamp at the middle of the event), (2) transit time (the total duration of the event), (3) single-channel amplitude (the ΔR caused by the event within its own channel), (4) node amplitude factor (the ratio of ΔR when the cell occupies a node to ΔR when the cell occupies a pore), (5) node duration factor (the ratio of the duration that the cell occupies a node to the duration that the cell occupies a pore), and (6) acceleration factor (the ratio of the cell velocity exiting the channel to the cell velocity entering the channel).

The data fitting subroutine takes the parameters of all detected events, plus their code identities and channel locations, and inputs them into the forward model to produce a predicted data frame. An objective function is defined to quantify the error between the prediction and the observed data. In practice, this function is the mean absolute value of the residual (the difference between prediction and observation), plus a penalty function to promote non-negativity of the residual. In each instance of data fitting, the objective function is minimized using the Matlab function `lsqnonlin` to determine fitted parameters for each detected event. Upper and lower bounds on the fitted parameters are defined by the user.

Chapter 6

Toward Integrated Molecular & Mechanical Screening

In previous chapters, we discussed the work to date in applying NPS to label-free single-cell analysis. As discussed in Chapter 2, NPS has previously been applied to screen for cell surface markers without the need for exogenous fluorescent or magnetic labels. As described in detail in Chapter 3, mechano-NPS is another variation of NPS that measures the biophysical, rather than biomolecular, cell properties. In this chapter, we will describe work toward integrating the biomolecular and mechanical cell screening technologies into one device that can perform these two separate measurements at the single-cell level, in a uniquely label-free manner. We will discuss the motivation for developing this integrated NPS device with an eye toward clinical applications in breast cancer screening, and we will review the concepts and underlying technologies that enable this new platform. We will present a proof-of-concept device design, provide detailed methods, and demonstrate successful preliminary cell measurements. Finally, we will discuss remaining challenges and suggest next steps for improving this platform.

6.1 Motivation

6.1.1 Breast Cancer Screening

Breast cancer (BC) will affect 1 in 8 U.S. women and is the second-leading cause of cancer-related deaths in women [94]. Some women are at an increased risk of BC due to factors such as family history or radiologically dense breasts, which are associated with a 2–4 fold increase in risk [95]. Women with constitutive BRCA1/2 mutations are more likely than not to develop BC eventually [95]. Since early diagnosis of BC results in improved outcomes [96], these high-risk women may opt for supplemental screening methods with the goal of detecting the cancer earlier.

Common screening methods utilize imaging technologies such as mammography, magnetic resonance imaging, or ultrasound to detect an existing tumor [95]. However, another type of supplemental screening strategy directly samples cells from the breast tissue and assesses the cells through cytology [97–100]. Rather than scanning for a carcinoma that has already developed, the cells are evaluated for precancerous changes that could develop into BC in the future. If a concerning result is found, the patient may consider more frequent screenings, chemoprevention, or prophylactic surgery. Additionally, direct tissue sampling strategies are often used to monitor patient response to prophylactic drugs in clinical trials, and there is hope that these methods might help predict which patients are most likely to benefit from specific treatments [101]. As discussed by Hoffman [102], breast tissue cytology may offer a fundamentally different type of biomarker than imaging because cells can be tested directly for precancerous properties.

6.1.2 Random Periareolar Fine-Needle Aspiration

Random periareolar fine-needle aspiration (RPFNA) [97] is one such tissue sampling strategy that is used to assess short-term risk of BC. A fine-gauge needle is used to collect cells from several sites on each breast. The needle is able to access cells from the terminal duct lobular units (TDLUs), where most BCs are thought to originate [101]. Cells are then fixed, stained, and examined by a pathologist. Clusters of epithelial cells are usually examined for the presence of hyperplasia (high growth rate) with or without atypia (abnormal morphology and/or organization). In a study of almost 500 high-risk women, Fabian *et al.* [101] demonstrated that women who showed hyperplasia with atypia in their RPFNA samples were more likely to develop cancer in both the short and long term (Fig. 6.1). This study supported the hypothesis that cellular morphological changes throughout the breast—which are observed in RPFNA samples—could indicate the risk of developing breast cancer in the future. As reviewed by Chai *et al.* [103], evidence of this "field effect" has been seen in many cancers, and it may be explained by genetic alterations that occur in a stepwise manner as cells progress from normal to malignant.

Today, RPFNA is used as the tissue sampling method for many Phase II trials in the U.S. [100]. It is considered a "surrogate endpoint biomarker" because it is strongly associated with cancer and is modulated by known prevention drugs. RPFNA has largely replaced nipple aspiration (NA) and ductal lavage (DL) in clinical trials because it is much more likely to yield a sufficient sample of cells (∼95 % for RPFNA vs. 30–60 % for NA/DL) [98,100,102]. Additionally, RPFNA is often preferred over repeated random core biopsy because it causes less patient discomfort and is more likely to contain cells from the TDLUs [99,101,102]. Furthermore, RPFNA has been shown to produce highly reproducible results in a multi-institutional trial [104].

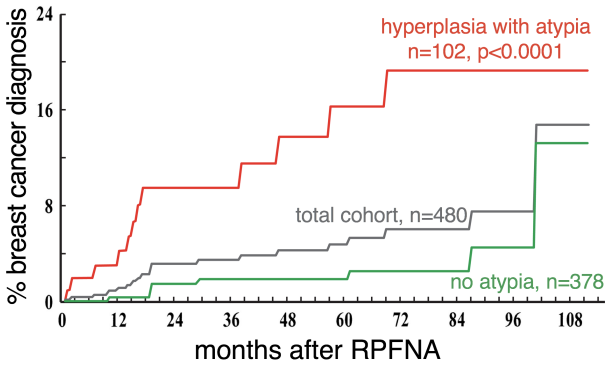

Figure 6.1: Longitudinal study of a cohort of 480 high-risk women who received RPFNA that was evaluated by cytology. Women whose RPFNA samples exhibited hyperplasia with atypia were five times more likely to have a later positive diagnosis of breast cancer. Adapted with permission from Fabian *et al.* [101].

6.1.3 Clinical Challenge

Although RPFNA is a promising method of sampling mammary tissue, challenges remain in improving the analysis of the collected cells. A quantitative method of evaluating the samples is desired, especially when RPFNA is used as a surrogate biomarker to monitor or predict the response to prophylactic drugs [102]. Masood developed a semi-quantitative scale for evaluating cytomorphology [105], but as discussed by Ljung *et al.* [106], the accuracy of pathological assessments may vary by the physician's training. Molecular biomarkers such as estrogen receptor (ER) and human epidermal growth factor receptor 2 (HER2) have been used to grade RPFNA specimens [101], but as Hoffman *et al.* discussed [102], the key challenge in this approach is cellular heterogeneity within the sample. Furthermore, current techniques fail to identify precancerous changes in women who go on to develop highly aggressive triple-negative BC, in which the most common molecular biomarkers are not present. New analysis methods are needed that can detect precancerous cellular changes in RPFNA samples in a quantitative way that is predictive for all types of BC.

6.2 Our Approach

6.2.1 Platform Requirements

Here, we propose a microfluidic device that can perform quantitative single-cell analysis of RPFNA samples. As discussed in Chapter 2, microfluidics provides the single-cell resolution that is needed to capture the heterogeneity of patient samples and identify subpopulations such as precancerous cells. Key to RPFNA analysis, our microfluidic platform must distinguish precancerous epithelial cells from normal ones against a background of other cell types present in a sample. Although the number of cells in RPFNA cytology samples has not

been explicitly determined, Fabian *et al.* [101] reported that most samples yielded ∼1000 epithelial cells. Therefore, our platform must be able to measure hundreds to thousands of cells.

In addition to epithelial cells, RPFNA samples contain stromal cells (fibroblasts), immune cells (leukocytes), and fat cells (adipocytes) [102]. Thus, our platform needs to distinguish between these major cell types. Furthermore, since mammary epithelial cells include three major sub-lineages (myoepithelial cells (MEPs), luminal epithelial cells (LEPs), and bipotential epithelial progenitors (MPPs)), our device must identify the sub-lineage before assessing whether an epithelial cell is normal or pre-cancerous. Since cell types and sub-lineages are classically defined by surface marker (SM) profiles, our proposed platform will need to perform SM screening to distinguish cell types.

Most importantly, our platform must be able to distinguish precancerous epithelial cells from normal ones. As discussed in Section 3.1, mechanical properties of cells have been implicated in the malignant progression for multiple cancers, including BC and triple-negative BC; in particular, more invasive cells are usually softer than their benign counterparts [42,46,59,60]. Thus, our proposed device will utilize mechanical phenotyping as an alternate biomarker for invasive potential. In addition to stiffness (elastic modulus), viscoelastic and mechanical recovery properties have been implicated in cancer migration and malignant progression [61,62]. Therefore, our platform should probe both elastic and viscoelastic/recovery properties.

6.2.2 Prior Work

Mechanical Phenotyping

AFM and micropipette aspiration are gold-standard methods for analyzing mechanical properties of cells. However, the throughput of these techniques is too low to be practical for analyzing hundreds of epithelial cells found in RPFNA samples (typical AFM sample sizes are $n \sim 30$ or fewer [42,61,63], and micropipette aspirations may take 10 min/cell [64]). As discussed in Section 2.3, recent microfluidic methods such as optical stretching [43,49] and hydrodynamic deformation [48,53] have much higher throughput, but are limited to measuring only the cell's elastic properties. As discussed in Section 6.2.1, our platform should assess cellular viscoelastic/recovery characteristics in addition to elastic properties; therefore, these methods are not sufficient for our application.

Surface Marker Screening

Image-based methods to detect molecular biomarkers, including immunofluorescence (IF) and immunohistochemistry (IHC), are not compatible with integrated mechanical phenotyping. When cells must be fixed as in IHC or intracellular IF, downstream mechanical analysis cannot be performed. IF can be performed on live cells, but it relies on fluorescent probes and antibodies (Abs) that target surface receptors, which have been shown to alter

cell mechanics as well as a variety of signaling pathways [107–109]. Moreover, using imaging to assess the SM profile of a cell prior to performing mechanical measurements would require a system to identify the particular cell of interest based on the image and then transfer it for mechanical analysis. Such a system would most likely suffer from very low throughput, on the order of tens of cells rather than the hundreds required here.

Fluorescence-activated cell sorting (FACS) is a common high-throughput method that screens and sorts cells based on SMs. In theory, FACS could be applied to RPFNA samples to separate cell populations and sub-lineages, which could then be analyzed separately by mechanical phenotyping. However, FACS has been shown to alter cell biology in several ways, including by inducing oxidative stress, affecting metabolic pathways, and altering gene expression [110,111]. These changes may be due to the high shear stress imposed by FACS machines, which can affect cell signaling pathways [112,113] as well as mechanical properties [114]. Additionally, FACS relies on fluorescent probes and thus suffers from the same disadvantages as IF. Therefore, FACS is not ideal for our application because the sorting process itself may induce changes that affect downstream measurements.

Fundamental Challenge

The main shortcoming in prior approaches to SM screening and mechanical phenotyping is the difficulty in combining the two measurements. The variety of cell types and sub-lineages in RPFNA samples calls for orthogonal measurements of SM profile and mechanical properties, but few technologies exist that accomplish this without using FACS. Bagnall *et al.* [115] reported a method for isolating specific cells based on their deformability as measured by surface microchannel resonators [116], followed by downstream IF imaging. However, the authors reported integrated mechanical and imaging data for <20 cells; thus, this method does not have sufficient throughput for RPFNA analysis.

We propose a new integrated microfluidic platform that will perform SM and mechanical measurements in series. This device is based on NPS, which has been previously applied to both SM screening [17,90] and mechanical phenotyping [2,20,58]. NPS has sufficient throughput for application to RPFNA, and it does not suffer from the disadvantages of FACS that arise from fluorescent labeling and high shear rates. Furthermore, as discussed in Section 3.1, NPS mechanical phenotyping is able to detect cellular changes associated with the malignant progression of breast cancer cells [20], including recovery from deformation. Thus, NPS is a promising method for RPFNA analysis, with the potential to distinguish and identify precancerous breast cells. The advantages of an NPS-based platform, as compared to prior work and alternate approaches, are summarized in Table 6.1.

6.2.3 Integrated Node-Pore Sensing

We present a novel microfluidic device design that can measure the SM profile as well as the mechanical properties of each cell. This device is based on NPS, the electronic cell sensing technology discussed in Chapters 3–5. We have designed an integrated, multi-parametric

surface marker (SM) screening		
technology	label-free?	cell viability
imaging	no	low
flow cytometry	no	medium
node-pore sensing	yes	high

mechanical phenotyping			
technology	sufficient throughput?	viscoelastic / recovery properties?	integration with SM?
AFM & micropipette	no	yes	no
hydrodynamic stretching	yes	no	no
surface microchannel resonators	no	no	yes
node-pore sensing	yes	yes	possible

Table 6.1: Comparison of techniques for SM screening and mechanical phenotyping.

platform by combining principles from prior NPS work [17,20] and applying new technological developments.

As discussed in Section 2.2.1, NPS [24] has previously been applied to create devices that either measure mechanical or biomolecular cell properties. Mechano-NPS [2,20,58], as discussed in Section 3.2, incorporates a contraction channel segment to enable measurements of cell deformability and recovery from deformation. Surface-marker NPS (sm-NPS) [17] accomplishes label-free SM screening by including channel sections patterned with Abs that target SMs of interest. Cells expressing a particular SM transit more slowly in the segment patterned with the corresponding Ab than in a reference segment coated with an IgG isotype control Ab (Fig. 6.2). This is due to transient binding between the cell's SM and the patterned Ab.

Our new NPS device combines sm-NPS and mechano-NPS in series. This integrated platform, called combo-NPS, enables independent label-free measurements of the SM profile and mechanical phenotype of each cell. One challenge in implementing such a platform was to develop an improved method of Ab surface patterning that could enable scalable and robust functionalization of the sm-NPS segments with multiple Abs. Another challenge was to maintain sufficient SNR despite the increased the channel length necessitated by including both sm-NPS and mechano-NPS segments.

To address these challenges, we took advantage of two recent technological developments. First, we applied DNA-directed patterning to perform highly multiplexed protein patterning on a glass substrate [117]. Second, we implemented a "multi-zone" NPS platform to perform multiple NPS measurements in series.

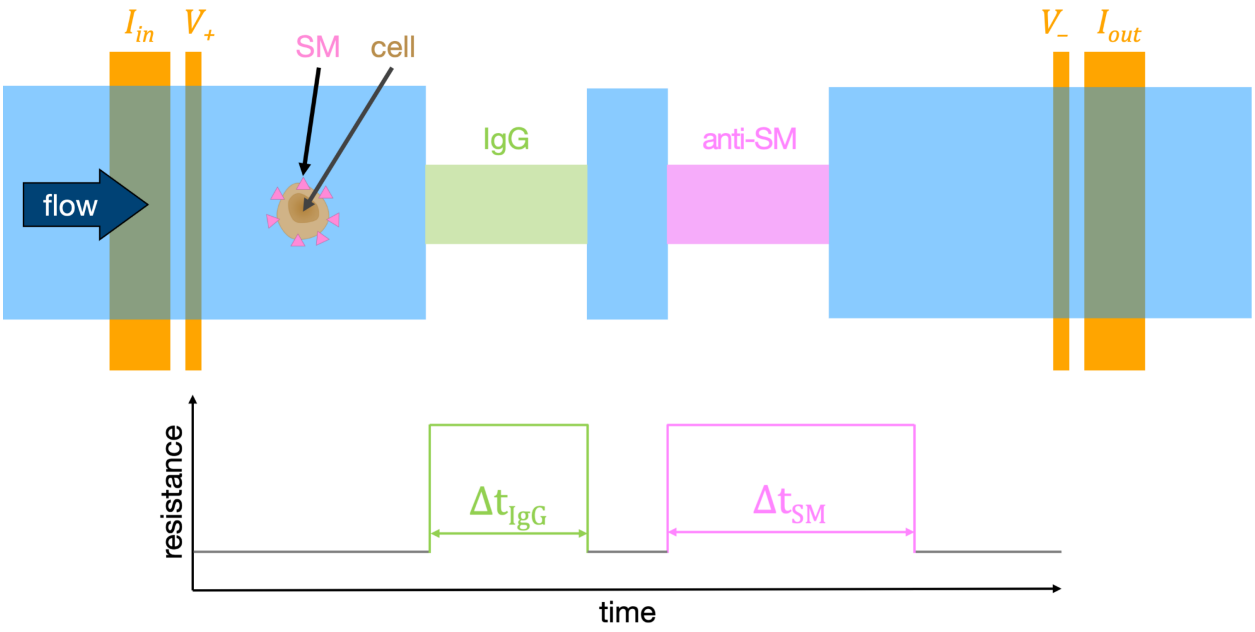

Figure 6.2: Operating principle of sm-NPS [17]. A cell expressing a molecular SM (pink triangles) traverses an NPS channel containing two segments. The first segment is patterned with an IgG control Ab (green); the second segment is patterned with an Ab (pink) that targets the SM. Due to transient interactions between the cell's SMs and the anti-SM Ab present in the second segment, the cell's transit time Δt is longer in the second segment than in the first.

DNA-Directed Patterning

In the original work describing sm-NPS [17], the Abs were conjugated to the glass substrate via Sulfo-EGS cross-linker and Protein G. Temporary channels fabricated from PDMS were aligned and clamped to the glass substrate such that each segment could be functionalized with a different Ab. Afterward, the temporary channels were replaced by the NPS channel, which was aligned and clamped without allowing the Ab to dry out and lose functionality. This process was difficult and time-consuming, especially as the number of Abs increased, and device production was difficult to scale up. Additionally, completed devices needed to be stored in a carefully controlled environment, and the functionalization process itself was found to lack robustness. Device leakage was also an issue, and high variability in driving pressure led to inconsistent transit times.

To address these issues, we adopted the DNA-directed patterning (DNA-dp) technique to pattern Abs [90,117] (Fig. 6.3). In DNA-dp, amine-terminated, single-stranded DNA oligonucleotides (oligos) are conjugated to an aldehyde-coated glass substrate through reductive amination [118]. Photolithography is used to serially pattern different oligos on each Ab target region [117]. Each Ab is conjugated to an azide-terminated complementary oligo using click chemistry [90,119], which hybridizes to the appropriate target region when incu-

bated with the DNA-patterned substrate. With this method, temporary channels are not needed, and multiple-Ab patterning can be performed immediately prior to NPS measurements, thus preserving Ab functionality. Particularly attractive to point-of-care applications such as RPFNA analysis, the oligo-patterned NPS devices have been demonstrated to have a shelf life of at least four weeks at room temperature [90].

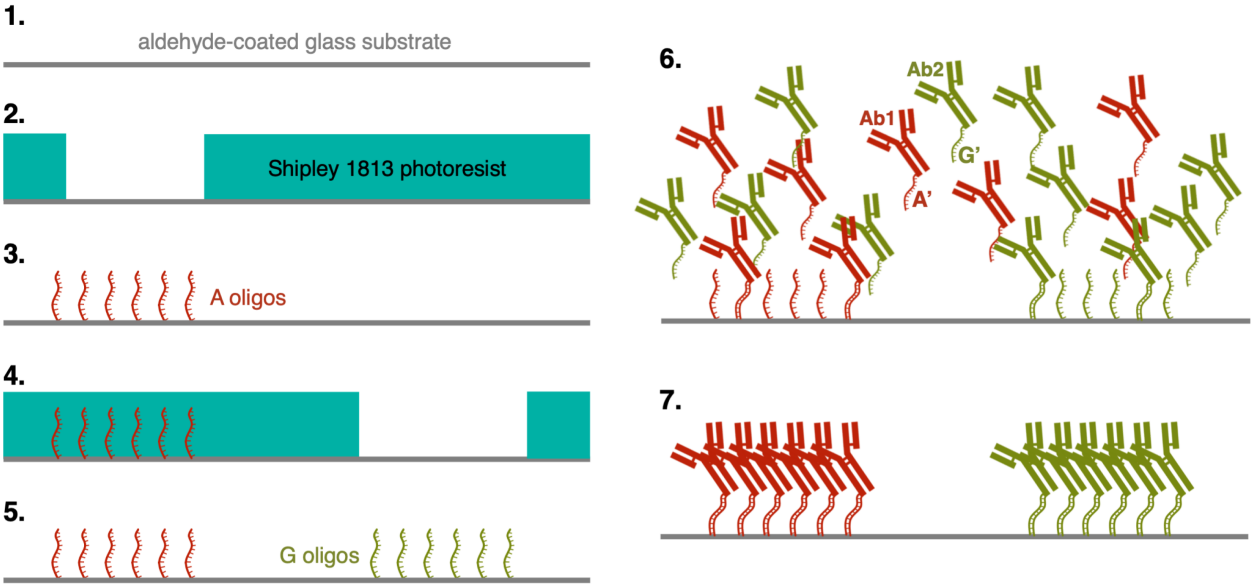

Figure 6.3: Multiplexed surface functionalization with Abs using DNA-dp [90,117]. An aldehyde-coated glass slide is photopatterned such that only the target region for oligo A is exposed (1–2), followed by reductive amination to conjugate oligo A onto the exposed target region of the surface (3). This process is repeated to conjugate oligo G onto its target region (4–5). Two different Abs, Ab1 (red) and Ab2 (green), are tagged with complementary oligos A' and G', respectively. The oligo-tagged Abs are incubated with the surface (6), and complementary hybridization ensures that each Ab binds to the region where the corresponding oligo was patterned (7).

In addition to applying DNA-dp for Ab patterning, Kozminsky *et al.* [90] modified the basic device design for sm-NPS to improve their results. Their device included flow-expansion chambers around the Ab-patterned regions to slow cells down, thereby ensuring sufficient Ab-antigen interaction. PDMS tapered "railings" were also included to confine cells to flow within the Ab-patterned regions, thus minimizing velocity variations due to cells flowing off-center within the channel. (An example of these expansion chambers and railings, as applied to combo-NPS, is shown in Fig. 6.4.) Finally, node-pore sequences were included before and after each Ab-patterned expansion region, such that a cell's subpulses could be measured before and after it entered the Ab regions. Thus, the cell's transit time in each Ab region was calculated by the elapsed time between the subpulses immediately before and after the Ab region.

Multi-Zone Node-Pore Sensing

While Kozminsky *et al.* were able to demonstrate screening of up to four SMs with their device design [90], SNR continued to be a limiting factor. In combo-NPS, the addition of the long segments required for mechano-NPS in series with the sm-NPS segments would reduce the SNR in the Ab-adjacent node-pores even further, because the overall channel volume would increase (see Chapter 4 for an in-depth discussion of SNR).

For this reason, we turned to multi-zone NPS (mz-NPS). In this technique, the channel is divided into separate "zones," which are electrically in series and are each measured separately. Dividing the long channel into these shorter zones improves SNR because each zone has a smaller volume than the overall device. A combo-NPS device design utilizing mz-NPS is shown in Fig. 6.4. The electrical current ($I_{in} = I_{out}$) through all zones is the same and is measured at the outer electrodes, while the voltage drop across each zone is measured at the inner electrodes (V_n). Thus, the resistance (R_z) is monitored separately in each zone; for example, in Fig. 6.4, $R_{zone3} = {}^{V_4 - V_5}/_{I_{in}}$.

Integrated Combo-NPS Platform Design

Our new, integrated NPS platform (combo-NPS) combines label-free SM screening with mechanical phenotyping at the single-cell level. As shown in Fig. 6.4, this device applies sm-NPS measurements to each cell, followed by mechano-NPS measurements. We take advantage of the developments in DNA-dp to facilitate robust multi-Ab functionalization for the sm-NPS segments, and we implement mz-NPS measurements to maintain good SNR throughout the long channel.

Our initial proof-of-concept (POC) design (Fig. 6.4) utilizes two Ab-patterned expansion regions to perform single-marker sm-NPS. One region is patterned with an Ab targeting the epithelial cell adhesion molecule (EpCAM) (CD326), while the other is patterned with the corresponding IgG isotype control Ab. Each expansion region is measured by its own electrical zone, which also encompasses a single pore before the expansion region and a two-pore/one-node sequence after the expansion region. The expansion regions also include the aforementioned PDMS "railings" that confine cells to flow within the Ab-patterned regions, similar to [90]. We employed computational simulation (Fig. 6.5) to confirm that the flow in these regions, even within our integrated combo-NPS design, maintains a slow velocity (to ensure sufficient cell exposure to patterned Abs) and uniform cross-section (to minimize velocity variations due to cells flowing off-center).

After the sm-NPS regions, our initial device design (Fig. 6.4) also includes a mechano-NPS sizing (reference) segment and a mechano-NPS contraction segment. Each of these segments is measured by its own electrical zone, for a total of four measurement zones. These mechano-NPS regions enable measurement of cell size, transverse deformation (δ_{deform}), and whole-cell deformability index ($wCDI$), as described in Section 3.2. Although this design does not include recovery segment(s), they could easily be added in future device designs.

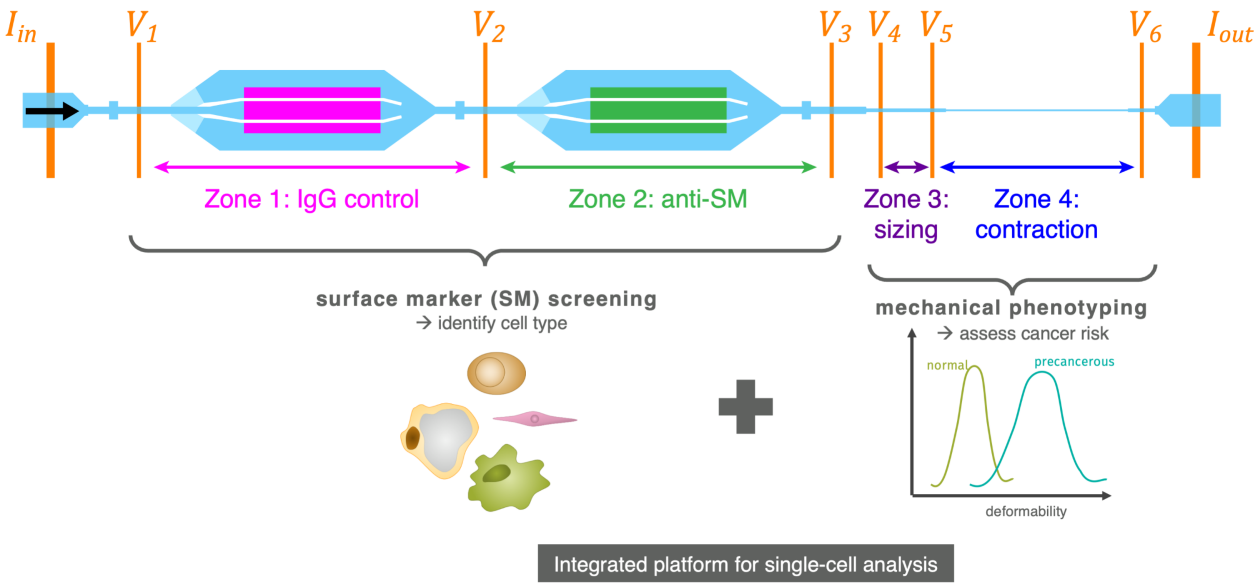

Figure 6.4: Combo-NPS for integrated single-cell SM screening and mechanical phenotyping. First, sm-NPS is performed as cells flow through expansion regions patterned with Abs using DNA-dp. Subsequently, mechano-NPS is performed as cells flow through sizing and contraction segments. Multiple electrical zones acquire separate NPS measurements in different regions of the channel, maintaining good SNR even in the long channel. Electrodes in orange; channels in blue; Abs in pink and green. White "railings" in the expansion regions confine cells within the Ab-patterned regions. Black arrow indicates flow.

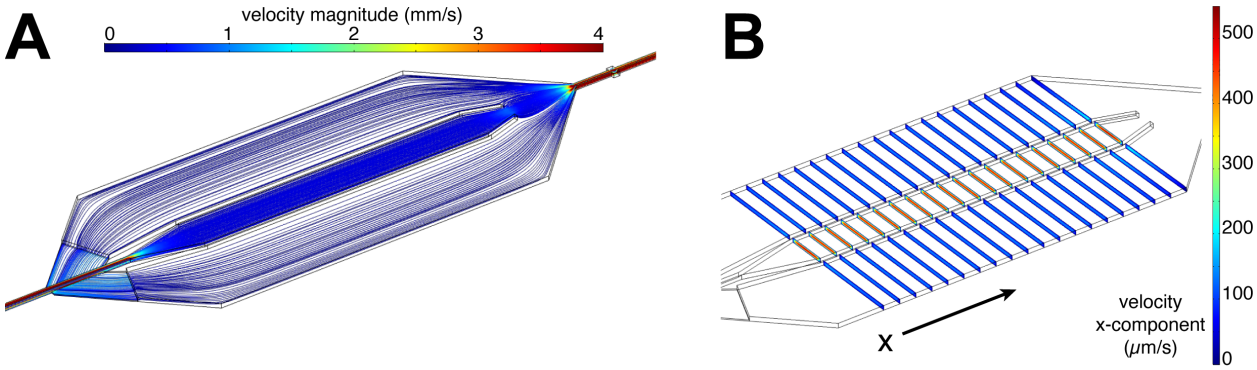

Figure 6.5: Finite-element simulations of the flow profile within combo-NPS expansion regions. Comsol Multiphysics was used to evaluate the flow profile within the Ab expansion regions of our POC design for integrated sm-NPS and mechano-NPS (Fig. 6.4). A) The model demonstrates that flow streamlines within the central Ab region are well-distributed and have very slow velocity magnitude, ensuring that cells have sufficient time to interact with the patterned Abs. B) The model demonstrates a consistent cross-sectional flow profile throughout the central Ab region, allowing for consistent effects to be observed in the cell transit time.

6.3 Methods

6.3.1 Device Design

We optimized our initial combo-NPS design (Fig. 6.4) for testing on well-characterized invasive MCF-7 breast epithelial cells that are EpCAM-positive. Based on an expected average cell diameter of ∼18 µm (data not shown), the width of the mechano-NPS sizing segment was 21 µm, and its length was 930 µm. The mechano-NPS contraction segment was 10.5 µm wide to target a strain value of ∼0.4, and its length was 3.38 mm. The channel height in the mechano-NPS segments was 23 µm.

The geometry of the sm-NPS regions was based on a modified version of the expansion region design used in [90]. The channel height and pore widths were 40 µm, and the pores were 350 µm long. The nodes were 100 µm wide and 60 µm long. The widest part of the expansion region was 2 mm wide and 3.16 mm long. PDMS railings confined cells to flow within a central region that was 360 µm wide and 2.75 mm long. A transition region with a 10 µm height allowed fluid but not cells to flow from the node-pore sections into the outer part of the expansion region. The Ab-patterned regions were 2.5 mm long and 1.08 mm wide, to allow for alignment tolerance with the central part of the expansion region.

6.3.2 Cell Culture

Cells were cultured according to standard methods. Cell culture was maintained at 37 °C in 5 % CO_2, and cells were routinely passaged once they reached 80 % confluence. MCF-7 cells were cultured in RPMI-1640 with 10 % FBS and 1X Penicillin-Streptomycin. To passage, cells were dissociated by incubation in 0.25 % trypsin/EDTA for 5–10 min at 37 °C, followed by trypsin neutralization with culture media at a ratio of 2:1 by volume. The cells were then centrifuged at 0.2 rcf for 5 min and re-seeded in culture media. All experiments were performed before passage 20.

6.3.3 Device Fabrication

The combo-NPS devices were fabricated in three stages: 1) NPS microchannels were fabricated in PDMS; 2) the glass substrate was patterned with electrodes and DNA oligos; and 3) the PDMS channels were bonded to the prepared substrate. This device was stored at room temperature until use. An overview of this process is shown in Fig. 6.6; details of the fabrication processes are provided below.

Microchannel Fabrication

PDMS microchannels were fabricated using soft lithography, generally following the process described in Section 3.3.1. Briefly, a negative-relief master mold for the microchannel structures was fabricated using SU-8 3010 epoxy photoresist and standard photolithogra-

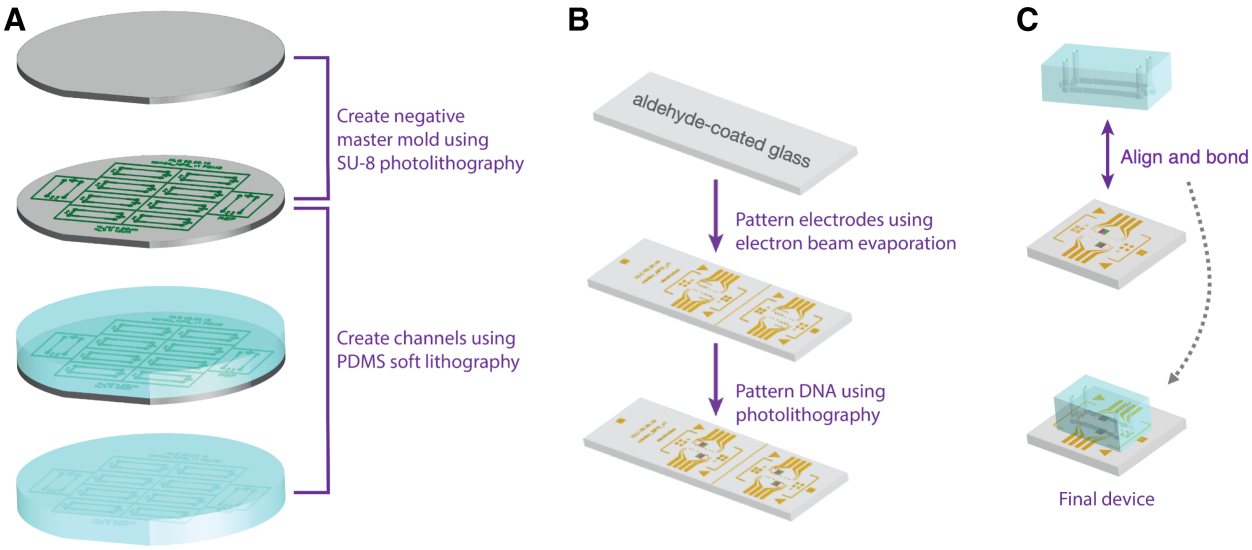

Figure 6.6: Fabrication process for integrated NPS. A) A negative SU-8 master mold is fabricated on a silicon wafer using photolithography, and the NPS channels are created from PDMS using soft lithography. B) Electrodes are patterned on an aldehyde-coated glass substrate using standard photolithography and electron-gun evaporation, followed by DNA surface patterning. C) Finally, the PDMS channels are aligned and bonded to the prepared substrate containing the DNA patterns and electrodes.

phy. PDMS was poured over the master mold and cured; then, PDMS slabs containing the embedded microchannel structures were excised.

To fabricate the master mold containing multiple feature heights, the SU-8 photolithography process was performed multiple times in series. For all layers, the pre-exposure bake was performed at 95 °C, the exposure energy was ∼280 mJ/cm^2, and post-exposure bakes were performed for 1 min at 65 °C followed by 3 min at 95 °C. All development steps were performed by incubation in SU-8 developer for 4 min, plus an additional 1–2 min incubation with agitation.

First, a 10 µm layer containing only SU-8 alignment marker features was fabricated (spin speed 4000 rpm, pre-exposure bake 8 min), and development was performed. The resulting feature height was 9.05 µm. For all subsequent layers, these alignment features were protected by applying Kapton tape before adding new SU-8; this tape was removed after the pre-exposure bake. Tape was only applied over the SU-8 alignment features, and was not applied over areas containing microchannel structures.

A 10 µm layer was fabricated to create the transition features of the expansion regions (spin speed 3500 rpm, pre-exposure bake 8 min). Next, a 13 µm layer was fabricated to create the mechano-NPS regions with a total height of 23 µm (spin speed 3000 rpm, pre-exposure bake 12 min). Finally, a 17 µm layer was fabricated to create the sm-NPS regions with a total height of 40 µm (spin speed 2000 rpm, pre-exposure bake 15 min).

After all layers were fabricated, a final development step was performed, followed by a hard-bake step for 30 min at 150 °C. The final feature heights were 9.93±0.44 µm for the transition layer, 23.68±0.22 µm for the mechano-NPS layer, and 41.46±1.81 µm for the sm-NPS layer.

Electrode Fabrication & DNA Patterning

Electrodes were patterned onto an aldehyde-coated glass substrate using electron-gun evaporation, which is described in detail in Section 3.3.1. The only modifications to this process for combo-NPS fabrication were that 1) the substrate was only immersed in acetone for ∼15–20 min during liftoff, and 2) the gold etch step was not performed due to concerns that the etchant could interfere with the aldehyde groups functionalized on the substrate.

Two orthogonal DNA oligos (oligos A and G; see Section 6.3.7) were patterned on the substrate with the prefabricated electrodes as described in [117] (Fig. 6.3). Briefly, amine-terminated, single-stranded DNA oligos were diluted to 40 µM in a solution of 50 mM sodium phosphate at pH 8.5. Shipley 1813 photoresist was patterned onto the aldehyde-coated glass substrate using the same photolithography process as that described in Section 3.3.1 for electrode fabrication. The pattern was defined such that the resist covered all areas of the device except for the target regions for the first oligo. The prepared solution containing the first oligo was drop-cast onto the exposed target regions, and the substrate was baked for 30 min in a 65 °C oven. The substrate was then immersed in a solution of 0.25 % sodium borohydride in PBS and incubated at room temperature for 10 min with frequent agitation to perform reductive amination [118]. Finally, the substrate was rinsed with DI water (18 MΩ), and liftoff was performed by rinsing with acetone and again with DI water. This process was repeated to pattern subsequent oligos in their respective target regions; the prefabricated electrode patterns served as alignment markers.

Bonding

An overview of the bonding process is shown in Fig. 6.7. As described by [90], the oligo-patterned regions of the glass substrate were protected with a sacrificial layer of Shipley 1813 resist, which was patterned using standard photolithography. The glass substrate (containing the prefabricated electrodes, DNA patterns, and protective photoresist) was then rinsed with DI water and dried with dry nitrogen gas. The PDMS slab was cleaned with adhesive tape, rinsed briefly with isopropanol and water, and dried with dry nitrogen gas. The glass substrate and PDMS were exposed to oxygen plasma treatment (60 Pa, 30 W, 2 min). The glass substrate was rinsed with acetone and DI water to remove the sacrificial resist and dried with dry nitrogen gas, and the PDMS slab was immediately mated to the substrate. Bonding was completed by baking the device for 10 min at 100 °C. The devices were stored at room temperature until use.

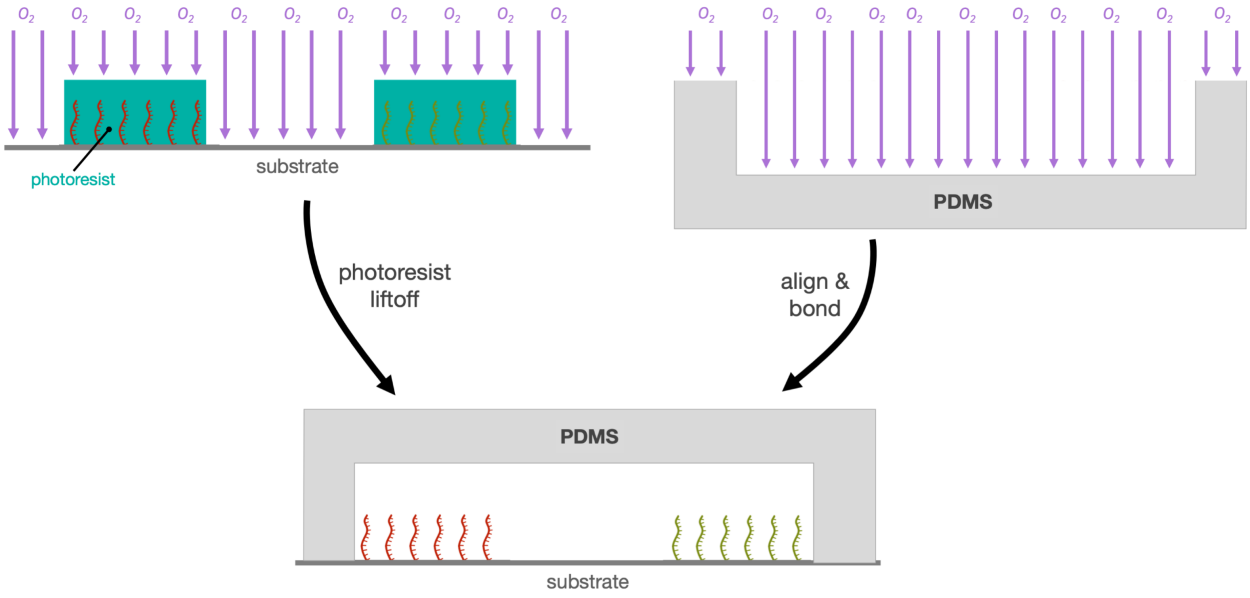

Figure 6.7: Bonding process for DNA-functionalized NPS devices. Patterned oligos (red and green) on the glass substrate are protected with a sacrificial layer of Shipley 1813 photoresist (teal). The substrate and the PDMS channels are exposed to oxygen plasma treatment. The photoresist is removed by rinsing with acetone and water, and the PDMS channels are immediately mated to the substrate.

6.3.4 Antibody-Oligonucleotide Conjugation

Mouse monoclonal Abs were conjugated to DNA oligos complementary to those patterned on the device substrate. The anti-EpCAM Ab (eBioscience, 1B7) and the IgG1κ control (eBioscience, P3.6.2.8.1) were conjugated to the G' and A' oligos, respectively. The conjugation was performed via click chemistry following the process described in [90]. Briefly, Amicon Ultra 100 kDa centrifugal filters were used to concentrate the Ab solution into a buffer of 200 mM sodium bicarbonate in DI water (pH 8.4). A 10 mM solution of the heterobifunctional cross-linker (DBCO−PEG_5−NHS) was prepared and added to the Ab in 32-fold molar excess. The mixture was incubated at room temperature for 2 h on a tube rotator. Invitrogen Centri-Spin 20 size-exclusion columns were used to remove the excess cross-linker. The azide-terminated oligo was then added to the solution in 2-fold molar excess and reacted at room temperature overnight on a tube rotator. Finally, Invitrogen Centri-Spin 40 size-exclusion columns were used to remove the excess free oligos.

6.3.5 Experimental Process

Antibody Patterning

Immediately prior to performing NPS experiments, the oligo-tagged Abs were introduced into the channel, where they hybridized to the corresponding DNA-patterned regions (Fig. 6.3). We implemented a streamlined process compared to prior protocols (*e.g.*, [90]). A solution of 2 % bovine serum albumin (BSA) in PBS was driven through the channel at 60 mbar until the entire channel was filled. (If necessary, the outlet could be temporarily closed to drive out any remaining air pockets.) The device was subsequently incubated with the BSA solution at room temperature for at least 1 h (up to overnight). The oligo-tagged Abs were diluted and mixed together to a final concentration of 0.2 µM in the 2 % BSA solution. The Ab mixture was driven through the channel at 60 mbar for 15 min, and the device was incubated at room temperature for 30 min. Finally, excess Abs were removed by flushing the channel with PBS at 60 mbar for 30 min.

Node-Pore Sensing Measurements

Cells were prepared for NPS measurements by passaging according to standard culture practice and diluting in PBS to a concentration of $\sim$200–500 $\times 10^3$ cells/mL. The cell suspension was filtered twice with a 20 µm strainer and kept on ice until NPS measurements were performed.

NPS measurements were performed in a similar method to that described in Section 3.3.2. The cell suspension was injected into the channel inlet with a driving pressure of 50–300 mbar. A constant voltage of 5 V was applied across the outer electrodes, and the resulting current through the outer electrodes was monitored along with the voltage at each of the inner electrodes. A custom printed circuit board was used to perform these measurements, along with a commercial USB data acquisition card from Measurement Computing Corporation. Custom MATLAB software was used to acquire and monitor the data.

6.3.6 Data Processing

The resistance across each zone was calculated according to Ohm's law as described in Section 6.2.3. Each zone's resistance signal was preprocessed by applying a low-pass filter, downsampling, and applying a moving-median filter. Each zone's baseline resistance was fitted using asymmetric least-squares [70].

6.3.7 Oligonucleotide Information

Oligos were purchased from Integrated DNA Technologies. Oligos A and G were 5'-amine-terminated and were conjugated to the aldehyde-functionalized glass substrate. Oligos A' and G' were 5'-azide-terminated and were conjugated to the Abs. Oligos A' and G' were also 3'-terminated with Cy5 and Cy3 fluorophores, respectively.

name	sequence (5'→3')
A	ACT GAC TGA CTG ACT GAC TG
G	AGC CAG AGA GAG AGA GAG AG
A'	CAG TCA GTC AGT CAG TCA GT
G'	CTC TCT CTC TCT CTC TGG CT

Table 6.2: Oligonucleotide sequences.

6.4 Preliminary Results & Discussion

6.4.1 Proof-of-Concept Design

Our preliminary results, based on measuring EpCAM+ MCF-7 cells, have been very promising. As shown in Fig. 6.8A, we demonstrated successful Ab patterning within the device. Moreover, Fig. 6.8B shows an example of a successfully measured cell pulse as it transits each zone. Preliminary analysis indicates that MCF-7 cells spend longer in the anti-EpCAM region than in the control region, as expected.

Although the results of these initial tests are promising, the quality of our measurements was hindered by very slow cell velocity in the SM zones, a problem that was compounded by relatively low SNR in these regions. While low flow velocity is desirable in the Ab-patterned regions to allow sufficient interaction between the cell SMs and the Abs, we observed cell transit times through the expansion zones that were an order of magnitude slower than those observed in previous successful sm-NPS experiments (*e.g.*, [90]). This is a result of the fact that mechano-NPS sizing and contraction segments were in series after the expansion regions, causing the pressure drop across the expansion regions to be dramatically reduced compared to an SM-only device. These extremely low sm-NPS flow speeds were problematic in multiple ways. Many cells settled and stuck to the bottom of the channel, and thus could not be measured. Moreover, the presence of these stuck cells altered the flow profile for subsequent cells transiting the channel. Additionally, tracking cell pulses in the data that took upwards of 30 sec each was extremely cumbersome, and the yield of good-quality pulses compared to the total number of cells that were measured in an experiment was very low.

We attempted to mitigate these issues by using a very high driving pressure of 300 mbar, but we still observed cell transit times of 8–9 sec in each sm-NPS zone. Moreover, as shown in Fig. 6.8B, this high pressure caused the measured cell subpulses in both the sm-NPS and mechano-NPS pores to be extremely short in duration. This time-compression of the subpulses results in less reliable cell measurements for two reasons: 1) fewer datapoints are sampled in each subpulse, so the estimates of subpulse width and average amplitude are less accurate; and 2) the signal for shorter-length pores (such as those used in the sm-NPS regions and the mechano-NPS sizing zone) is moved to a higher-frequency domain that has more

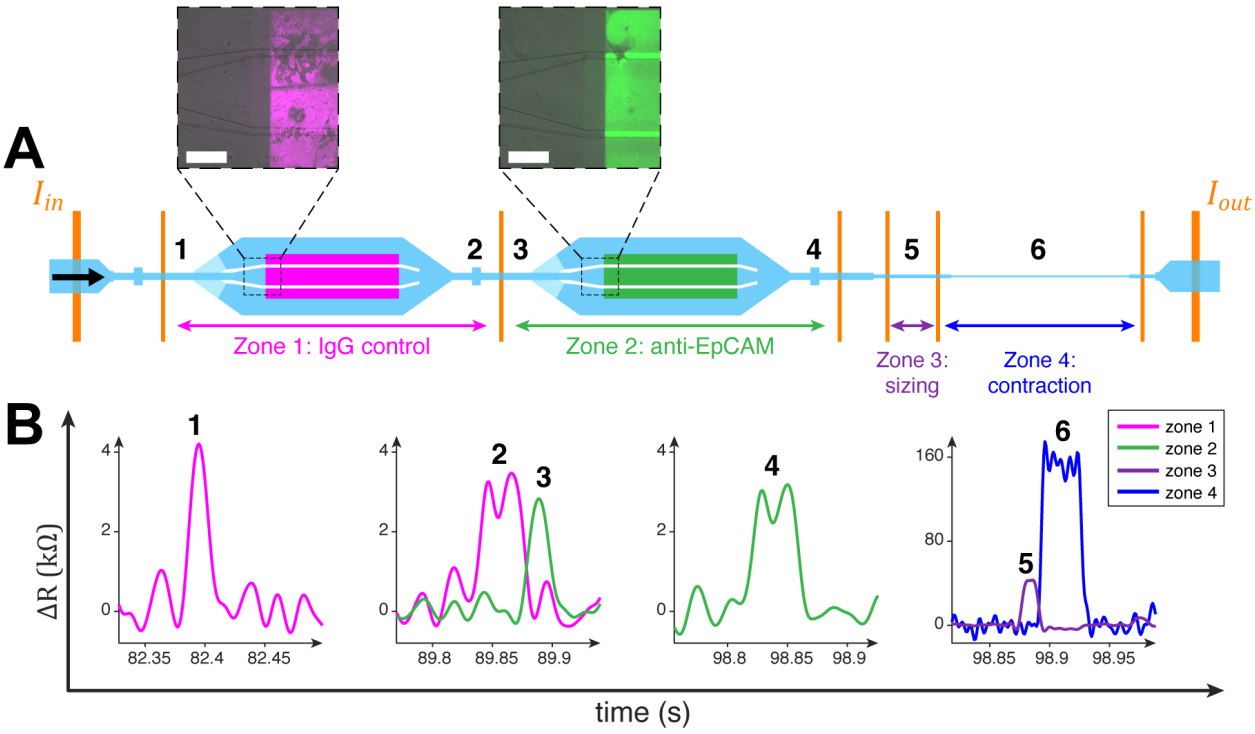

Figure 6.8: Integrated surface marker NPS and mechano-NPS. A) Electrodes (orange) define four zones whose electrical impedance is measured. Two Ab regions (pink and green) are patterned to perform surface marker screening, followed by sizing and contraction segments to perform mechano-NPS. Insets: successful Ab patterning of IgG (pink, visualized by Cy5 conjugate) and anti-EpCAM (green, visualized by Cy3 conjugate) within the integrated NPS device (scale bars $= 200\,\mu\text{m}$). B) Representative electrical resistance signals in the four zones caused by an MCF-7 cell transiting the integrated device. Signals are shown when the cell transits (1) and (3) the single pore before each Ab region; (2) and (4) the 2-pore/1-node sequence after each Ab region; (5) the sizing segment; and (6) the contraction segment. The cell whose data is shown spent $\sim 20\,\%$ longer in the anti-EpCAM region than in the IgG control region, consistent with the expected EpCAM+ phenotype.

overlap with the baseline measurement noise. This second challenge is especially evident in the sm-NPS zones, which have a lower SNR due to the much larger fluid volume than the mechano-NPS zones. In the example shown in Fig. 6.8B, signals from cells traversing single-pore expansion channel entrances (1 and 3) appear as narrow peaks of a similar frequency to the baseline noise rather than rectangular pulses, and signals from the two-pore/one-node expansion channel exits (2 and 4) are barely distinguishable as two peaks rather than a single peak.

6.4.2 Next-Generation Device Design

To address these issues, we conceived of a next-generation combo-NPS design (Fig. 6.9A) with several major changes. First, we increased the fluidic resistance of the sm-NPS regions to compensate for the added fluidic resistance of the downstream mechano-NPS regions. We designed much narrower expansion regions with the same channel height as the mechano-NPS regions and without the need for PDMS railings or a transition region. Second, we added a mechano-NPS recovery segment, which was not included in our original design. Finally, we employed a different sensing strategy for the SM regions, whereby we only apply NPS measurements in the regions *between* the expansion regions, instead of designing mz-NPS measurement zones that each span an entire expansion region. We made this change in order to maximize SNR even more, given that the cell does not need to be measured when it is in the middle of an expansion region.

We utilized finite-element simulations to fine-tune the design of this new concept. First, we validated that the flow profile was still slow and uniform in the expansion regions (Fig. 6.9B,C). We then performed a particle tracing simulation to estimate the flow velocity as a cell would transit each region (Fig. 6.9). Based on the relative velocities of the simulated particle in each region, we adjusted the relative lengths of each region in the design until we achieved a simulation that was well-matched with our target transit times of ∼1.0–1.4 sec in each Ab region, ∼110 ms in the reference zone, ∼170–180 ms in the contraction zone, and ∼5000 ms in the recovery zone. These target times were based on past successful experiments in both sm-NPS and mechano-NPS (*e.g.*, [58,90]).

Using this updated device design, we performed preliminary experiments with MCF-7 cells. With a driving pressure of 80 mbar, the cell velocity and resulting signals were much improved (Fig. 6.10). The cells spent under 5 sec to transit the whole channel, and the cells spent ∼1 sec in each Ab region. The subpulses in all zones took on the desired rectangular pulse shape rather than a peak shape, and SNR in all zones was very good. However, we did not observe consistently longer transit times in the anti-EpCAM region than in the IgG region. We speculate that several factors may have been at play: 1) the cell velocity in the Ab regions may have been too fast to allow interaction between the cell SM and the Abs, 2) the cell was not allowed to spend enough time in the Ab-patterned region to observe a consistent effect, and/or 3) cells sticking to the bottom of the Ab regions (which we did still observe in this design) may have disrupted the flow, making cell transit times between the anti-EpCAM region and IgG control region not comparable.

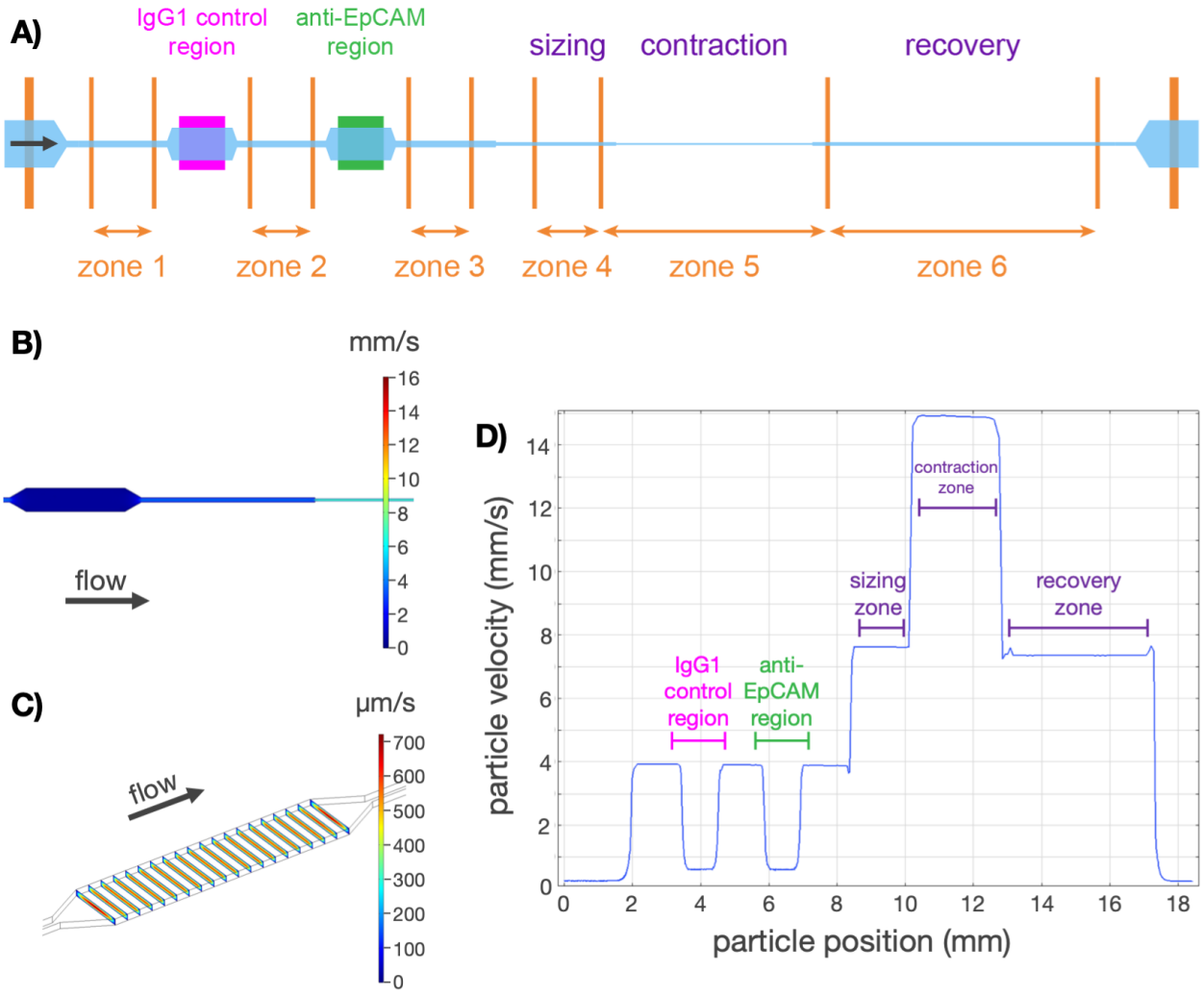

Figure 6.9: The next-generation integrated NPS design. A) Schematic of the device. Electrodes are shown in orange; the PDMS channel is shown in blue; and the Ab-patterned regions are shown in pink and green. NPS measurements are taken at the indicated zones between the electrodes. B) Simulated flow velocity in the center plane of the design, demonstrating uniformity throughout the Ab region. C) Simulated cross-sectional flow profile in the expansion region, demonstrating that uniformity is maintained. D) Simulated particle velocity in each region of the design.

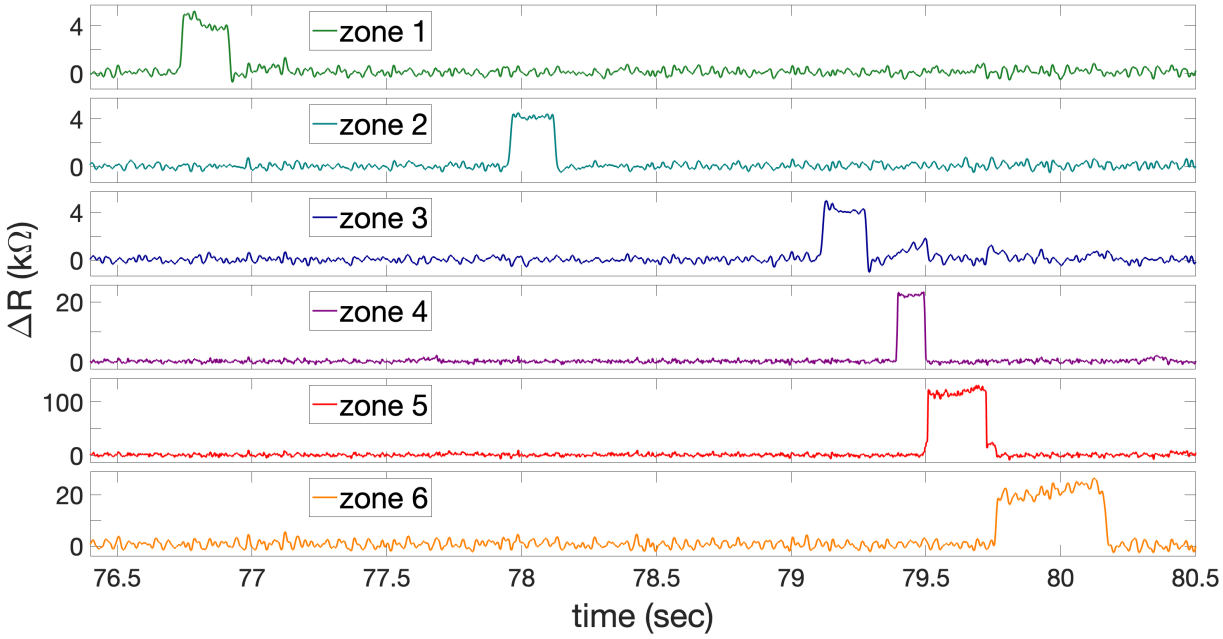

Figure 6.10: Preliminary results with the next-generation integrated NPS design. Representative electrical resistance signals from each of the six zones caused by an MCF-7 cell transiting the integrated device (with updated design as shown in Fig. 6.9).

6.5 Next Steps

One major challenge we observed is that cells often adhered to the bottom of the Ab-patterned expansion regions in both device designs. This could be especially problematic because the presence of stationary cells on the channel floor may disrupt the measurement of SMs. Not only do stuck cells block other cells from reaching that portion of the Ab-patterned substrate, but their presence also blocks part of the flow in the channel, leading to a flow profile that differs between the test Ab region and the IgG control region. We hypothesize that multi-cell clusters are the most likely to sink and adhere to the channel floor, so reducing cell clumping (and/or cell-cell interactions) could help mitigate this issue. One option would be to add EDTA or a surfactant such as Tween-20 to the cell suspension. In either case, these additives should first be tested to confirm that they do not interfere with the Ab-surface conjugation or with the Ab functionality. Additionally, optimization (through simulation and/or experimentation) may be needed to find an appropriate target cell velocity that allows for SM-Ab interaction while minimizing the chance of cells adhering to the bottom.

Another potential issue is that the cross-linker used to label Abs with oligos may react with free amino groups that are present in multiple locations on the Ab molecule. If any cross-linkers are conjugated too close to the antigen-binding domain, reduced Ab activity

and/or high device-device variability may be a factor. We could address this issue by using a commercial cross-linker that selectively targets sites that are far from the antigen-binding domain, *e.g.*, oYo-Link DBCO [120]. Alternately, we propose a reaction scheme based on avidin-biotin interaction as shown in Fig. 6.11. This method takes advantage of commercially available biotinylated Abs, which place the biotin group far from the antigen-binding domain and have verified Ab functionality. This method has the additional advantage that stocks of oligo-tagged neutravidin could be prepared in advance and mixed with different biotinylated Abs as needed.

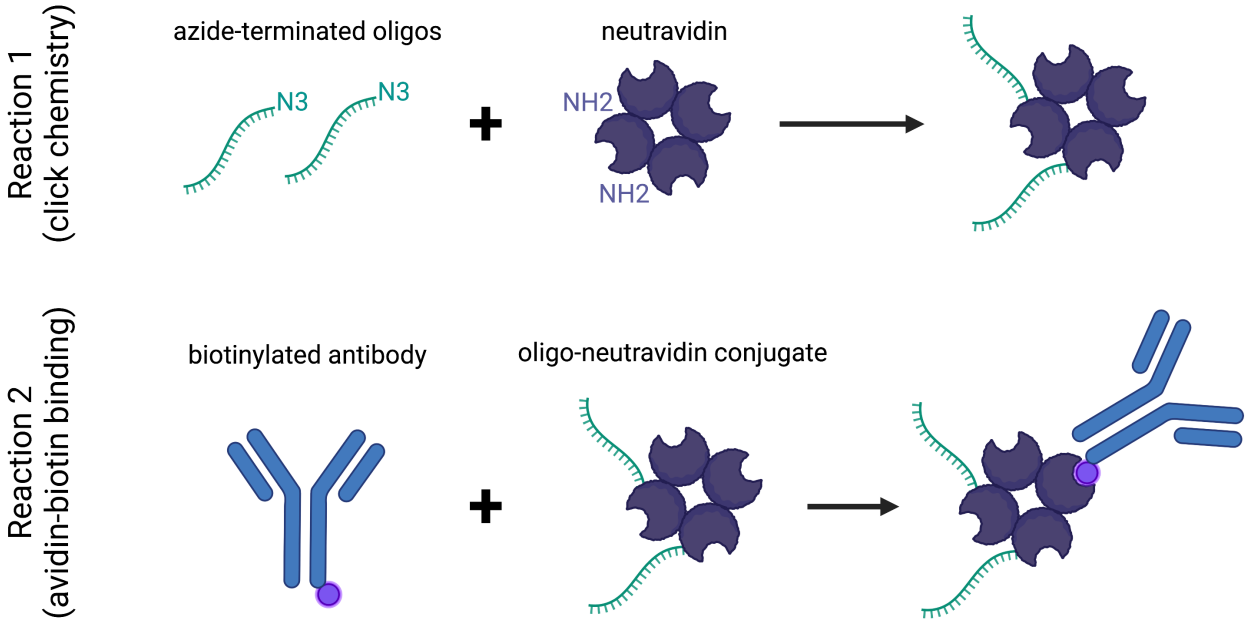

Figure 6.11: Ab-oligonucleotide conjugation through click chemistry and avidin-biotin interaction. First, azide-terminated oligos are conjugated to neutravidin through click chemistry (targeting free amine groups). Then, biotinylated Abs are mixed with the oligo-neutravidin conjugate, and binding takes place through the avidin-biotin interaction. Created with BioRender.com.

Our updated design includes six mz-NPS measurement zones, which is the maximum that our data acquisition system can read simultaneously. However, to screen for additional SMs with this design would require additional zones. In future iterations, we believe the mechano-NPS sizing and recovery segments could be measured in the same zone as the contraction segment, since these zones have the highest SNR. Alternatively, the sizing segment could be measured in the same zone as the final SM segment, and the mechano-NPS contraction and recovery zones could be combined. Additionally, the number of measurement zones required for SM screening could be reduced by one by returning to a device design where each sm-NPS measurement zones spans an entire expansion region, as in our initial device design. We believe that SNR in this case could be sufficient with a design more like our next-generation

combo-NPS device, which involves much lower fluid volume in the expansion region and allows for longer cell transit times in the pores before and after the expansion.

One final issue is whether the presence of a cell in the contraction segment would interfere with SM screening of another cell that is in an expansion region at the same time. While a cell is being deformed in the contraction segment, the overall device fluidic resistance is increased, and fluid velocity in the expansion regions would decrease. We believe the effect of this phenomenon on the ability to discern cell SM phenotype by transit times in the expansion region depends on the exact design geometry, and how long a cell spends in the contraction segment compared to the overall transit time in the expansion region. It would be helpful to conduct experiments and/or simulations to confirm this, because measurement yield would be much improved if SM measurements do not have to be discarded when another cell is present in the contraction segment.

6.6 Conclusions

Our integrated combo-NPS platform is a flexible tool that can be applied to many different systems. This device has the potential to be immediately useful in our current research projects on the mechanobiology of leukemia and on evaluating chondrocytes for tissue engineering. In the future, our goal is to apply this platform to RPFNA sample analysis, where it could change the paradigm for early breast cancer screening by providing a highly quantitative detection method for precancerous cells. Combo-NPS could also be readily adaptable to other cancer applications, such as detecting circulating tumor cells from blood. We plan to implement additional engineering features to extend the platform's capabilities, particularly on-chip size sorting with deterministic lateral displacement [121] and multiplexing using parallel coded channels (Chapters 4–5). Ultimately, the ability to measure the surface marker profile and mechanical properties of the same cell could open up many new possibilities for answering biological questions and improving patient outcomes.

Chapter 7

Summary & Future Work

This dissertation comprises a body of work focused on the NPS platform for label-free, single-cell sensing. As an electronic-based platform capable of measuring multiple cellular properties at high throughput, NPS is a flexible and powerful technology that has already led to new discoveries in breast cancer biology and drug resistance in leukemia [20,58]. In this work, we have characterized the NPS platform's reproducibility and added new technological capabilities that will further expand the platform's potential applications.

7.1 Prior Work

In Chapter 2, we reviewed the state of the field in label-free microfluidic tools for single-cell analysis. The disadvantages of cell measurement techniques that rely on exogenous labels include time-consuming and costly sample preparation, limited multiplexing of fluorescent labels, and the influence of the labels themselves on the cell's biology—which could potentially confound experimental results. There are also major advantages to performing single-cell measurements as opposed to bulk measurements, especially when rare subpopulations such as cancerous cells are of interest. For these reasons, a number of microfluidic label-free, single-cell measurement technologies have been developed in recent years.

Electronic sensors are a popular type of label-free cellular analysis. We discussed a number of recent electronic-based platforms, including those based on both resistive-pulse sensing and cellular impedance analysis. These technologies are popular because of the accessibility and low cost of electronic components, and have already seen commercial adoption in several products on the market today. Another class of label-free cellular measurements involves deformation analysis, in which cells are deformed by applying a force while their response is measured by optical imaging. This technique reveals information about the cells' mechanical phenotype, which is an important alternative biomarker in studying many cancers. We reviewed several such platforms that accomplish high-throughput microfluidic mechanical phenotyping, including devices that employ optical trapping as well as those that rely on hydrodynamic deformation. Many of these techniques enable very high throughputs, and

multiple companies have emerged that focus on commercializing this type of platform for both research and clinical use.

Overall, there have been many exciting developments in microfluidic label-free tools for single-cell measurement and analysis. NPS is a unique and powerful platform within this space because of its demonstrated capability to measure both mechanical and molecular properties of cells at high throughput. Furthermore, NPS benefits from the robustness and accessibility of electronic sensing.

7.2 New Findings

In Chapter 3, we focused on the mechano-NPS platform for cellular mechanical phenotyping. We reviewed the theory underpinning this technology and provided detailed methods for device fabrication, experimental process, and data analysis. We then conducted a systematic study to quantify the reliability of mechano-NPS data processing using our semi-automatic command-line interface software [71], which improves data processing efficiency ten-fold [2]. We showed that this data processing method results in very high intra- and inter-user reproducibility, even for novice users. In combination with the technical variability due to device and hardware variation quantified in [2], our results demonstrate that mechano-NPS is a highly robust mechanical phenotyping platform. We can be confident that mechano-NPS produces reliable measurements across different users, devices, and laboratories, which is critical for wider adoption of this technology in both research and clinical applications.

In Chapters 4 and 5, we developed, implemented, and characterized a novel method to enable multiplexed NPS measurements for the first time. The added capability to perform multichannel NPS measurements, in which cells flow through multiple channels in parallel, increases the throughput and flexibility of the NPS platform. Our method is unique among other techniques for multichannel electronic-based measurements because it does not require additional microfabricated electrodes nor modifications to the data acquisition hardware or software. This is advantageous because it enables immediate implementation by any laboratory with the capability to perform single-channel resistive-pulse sensing measurements, thereby increasing the technique's accessibility and versatility.

Our multiplexing method takes advantage of the spatiotemporal encoding in NPS, in which the sequence of nodes and pores in the channel geometry produces a unique coded pulse in the resulting signal. We encode each parallel channel with a specific sequence, and then apply a single electrical resistance measurement across all channels. By applying matched-filter detection and successive interference cancellation techniques in the data processing stage, we can deconvolve the signals from each channel and automatically detect cell pulses. In Chapter 4, we developed a mathematical model for calculating cell size based on multichannel measurements with this system, and we validated this model through computational modeling. We also described the theoretical considerations for the tradeoff between number of parallel channels and signal–noise ratio for this new multiplexing strategy. In Chapter 5, we designed three new multichannel NPS devices using this method, and we

demonstrated successful multiplexed NPS measurements in all three. We also developed and implemented a new data processing pipeline that deconvolves the multichannel measurements, automatically detects cells, and resolves coincidence events [89]. We applied the mathematical model developed in Chapter 4 to enable accurate cell size calculation based on the detected cell pulses. Additionally, we experimentally characterized the relationship between signal–noise ratio and number of parallel channels, and we compared these results with our theoretical predictions from Chapter 4.

In Chapter 6, we presented a new NPS platform, called combo-NPS, that combines mechanical and molecular single-cell measurements for the first time. We described the motivation for developing this platform as a tool for detecting precancerous cells in tissue samples from women at high risk for breast cancer, and we reviewed previous work in both mechanical and molecular cell phenotyping. Our new platform combines two new developments in NPS technology: DNA-directed antibody patterning [90,117], which enables reliable fabrication of devices with different antibodies in different regions of the channel; and multi-zone NPS, which improves signal–noise ratio by dividing the channel into multiple regions that are each measured separately. We applied computational modeling to test multiple device designs and optimize the fluidic coupling between the molecular screening section and the mechanical phenotyping section. We provided detailed methods for device fabrication, experimental process, and data processing, and we also demonstrated preliminary results with two different combo-NPS device designs using an immortalized breast epithelial cell line. Although we encountered several challenges in implementing this novel integrated platform, we discussed the underlying issues in-depth and provided suggestions for improvements going forward.

In summary, we have improved our understanding of the NPS platform's reliability by showing that the data processing software produces highly consistent results between users. We have also added the capability to perform multichannel NPS measurements for the first time using an entirely new method of multiplexing, which increases the platform's throughput and versatility. Finally, we have demonstrated preliminary work toward combining biomolecular and mechanical cell screening with a novel, integrated NPS platform.

7.3 Future Work

NPS is a flexible platform that can be applied to many different systems. With our new capabilities for multichannel measurements and integrated molecular and mechanical phenotyping, additional engineering features can be added that extend the platform's abilities even further. For example, on-chip size sorting could be implemented with a method such as deterministic lateral displacement [121], and the sorted populations could be measured with parallel NPS channels optimized for specific cell types.

Taking together the exciting developments in Chapters 4–6, we envision a multichannel, multi-zone, fully integrated NPS platform capable of measuring multiple cell properties in multiple channels simultaneously (Fig. 7.1). Because our novel method for multichannel NPS does not require any modifications to the electrode configuration or data acquisition

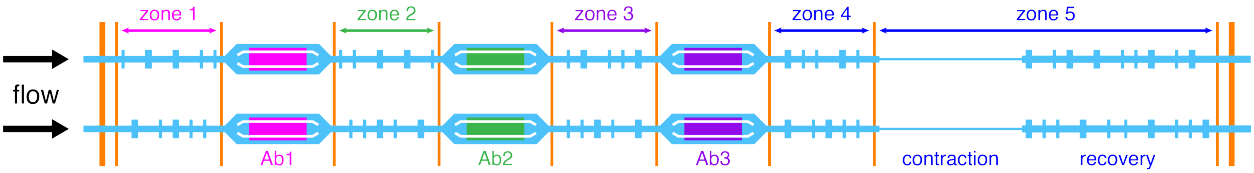

Figure 7.1: Concept of integrated, multichannel, multi-zone device combining mechano-NPS with surface marker screening. Electrodes (orange) measure the electrical resistance across five consecutive zones and are shared across two parallel channels (blue). Antibodies (Abs) (pink, green, and purple) are patterned in expansion regions with encoded zones in between, which allow measurement of the cell transit time (*e.g.*, ΔT_{Ab1} is the elapsed time between zones 1–2). Cell diameter is calculated by the pulse amplitude in Zone 4, while Zone 5 contains a contraction segment followed by an encoded recovery section, thus measuring cell deformability and recovery time. More zones (corresponding to more antibody regions) and more parallel channels (to increase throughput) can easily be added to this modular platform.

hardware, it is readily integrated with the multi-zone NPS measurements utilized in combo-NPS. As shown in Fig. 7.1, we could use our coding strategy to multiplex the platform by encoding parallel channels with specific sequences of nodes and pores. To apply this strategy to NPS-based molecular biomarker screening, we would encode the zones between antibody-patterned regions with these codes and compute the elapsed time between zones to measure the molecular phenotype. For mechano-NPS, we envision encoding the reference and recovery sections immediately before and after the contraction segment. Then, we would compute the elapsed time between a cell exiting the encoded reference section and entering the encoded recovery section in order to calculate the whole-cell deformability index.

As exemplified by this next-generation design, the body of work presented in this dissertation unlocks future NPS applications in both the research and clinical domains.

References

[1] T. R. Carey*, K. L. Cotner*, B. Li*, and L. L. Sohn, "Developments in label-free microfluidic methods for single-cell analysis and sorting", *Wiley Interdisciplinary Reviews: Nanomedicine and Nanobiotechnology*, no. March, e1529, 2018, ISSN: 19390041. DOI: 10.1002/wnan.1529. [Online]. Available: https://onlinelibrary.wiley.com/doi/full/10.1002/wnan.1529, *Equal contribution.

[2] B. Li*, K. L. Cotner*, N. K. Liu, S. Hinz, M. A. LaBarge, and L. L. Sohn, "Evaluating sources of technical variability in the mechano-node-pore sensing pipeline and their effect on the reproducibility of single-cell mechanical phenotyping", *PLOS ONE*, vol. 16, A. Han, Ed., e0258982, 10 Oct. 2021, ISSN: 1932-6203. DOI: 10.1371/JOURNAL.PONE.0258982. [Online]. Available: https://journals.plos.org/plosone/article?id=10.1371/journal.pone.0258982, *Equal contribution.

[3] K. T. Kim, H. W. Lee, H. O. Lee, H. J. Song, D. E. Jeong, S. Shin, H. Kim, Y. Shin, D. H. Nam, B. C. Jeong, D. G. Kirsch, K. M. Joo, and W. Y. Park, "Application of single-cell rna sequencing in optimizing a combinatorial therapeutic strategy in metastatic renal cell carcinoma", *Genome biology*, vol. 17, p. 80, Apr. 2016, ISSN: 1474760X. DOI: 10.1186/S13059-016-0945-9.

[4] M. C. Miller, G. V. Doyle, and L. W. M. M. Terstappen, "Significance of circulating tumor cells detected by the cellsearch system in patients with metastatic breast colorectal and prostate cancer", *Journal of Oncology*, vol. 2010, pp. 1–8, 2010, ISSN: 1687-8450. DOI: 10.1155/2010/617421.

[5] B. Xi, N. Yu, X. Wang, X. Xu, and Y. A. Abassi, "The application of cell-based label-free technology in drug discovery", *Biotechnology Journal*, vol. 3, pp. 484–495, 4 2008, ISSN: 18606768. DOI: 10.1002/BIOT.200800020.

[6] K. C. Cheung, M. D. Berardino, G. Schade-Kampmann, M. Hebeisen, A. Pierzchalski, J. Bocsi, A. Mittag, and A. Tárnok, "Microfluidic impedance-based flow cytometry", *Cytometry Part A*, vol. 77, pp. 648–666, 7 Jul. 2010, ISSN: 15524922. DOI: 10.1002/CYTO.A.20910.

[7] H. Morgan, T. Sun, D. Holmes, S. Gawad, and N. G. Green, "Single cell dielectric spectroscopy", *Journal of Physics D: Applied Physics*, vol. 40, pp. 61–70, 1 Jan. 2007, ISSN: 00223727. DOI: 10.1088/0022-3727/40/1/S10.

[8] A. Valero, T. Braschler, and P. Renaud, "A unified approach to dielectric single cell analysis: Impedance and dielectrophoretic force spectroscopy", *Lab on a Chip*, vol. 10, pp. 2216–2225, 17 Sep. 2010, ISSN: 14730189. DOI: 10.1039/C003982A.

[9] P. R. Gascoyne, S. Shim, J. Noshari, F. F. Becker, and K. Stemke-Hale, "Correlations between the dielectric properties and exterior morphology of cells revealed by dielectrophoretic field-flow fractionation", *Electrophoresis*, vol. 34, pp. 1042–1050, 7 Apr. 2013, ISSN: 01730835. DOI: 10.1002/ELPS.201200496.

[10] K. H. Han, A. Han, and A. B. Frazier, "Microsystems for isolation and electrophysiological analysis of breast cancer cells from blood", *Biosensors and Bioelectronics*, vol. 21, pp. 1907–1914, 10 Apr. 2006, ISSN: 09565663. DOI: 10.1016/J.BIOS.2006.01.024.

[11] G. Kang, S. K. Yoo, H. I. Kim, and J. H. Lee, "Differentiation between normal and cancerous cells at the single cell level using 3-d electrode electrical impedance spectroscopy", *IEEE Sensors Journal*, vol. 12, pp. 1084–1089, 5 2012, ISSN: 1530437X. DOI: 10.1109/JSEN.2011.2167227.

[12] Y. Zhao, X. T. Zhao, D. Y. Chen, Y. N. Luo, M. Jiang, C. Wei, R. Long, W. T. Yue, J. B. Wang, and J. Chen, "Tumor cell characterization and classification based on cellular specific membrane capacitance and cytoplasm conductivity", *Biosensors and Bioelectronics*, vol. 57, pp. 245–253, Jul. 2014, ISSN: 09565663. DOI: 10.1016/J.BIOS.2014.02.026.

[13] W. H. Coulter, *Means for counting particles suspended in a fluid*, 1953. [Online]. Available: https://patents.google.com/patent/US2656508A/en.

[14] O. A. Saleh, "A Novel Resistive Pulse Sensor for Biological Measurements", Ph.D. dissertation, Princeton University, 2003. [Online]. Available: http://www.materials.ucsb.edu/%7B~%7Dsaleh/Research/Saleh%7B%5C_%7DOmar%7B%5C_%7DThesis.pdf.

[15] F. F. Becker, X. B. Wang, Y. Huang, R. Pethig, J. Vykoukal, and P. R. Gascoyne, "Separation of human breast cancer cells from blood by differential dielectric affinity", *Proceedings of the National Academy of Sciences of the United States of America*, vol. 92, pp. 860–864, 3 Jan. 1995, ISSN: 00278424. DOI: 10.1073/PNAS.92.3.860.

[16] N. N. Watkins, U. Hassan, G. Damhorst, H. Ni, A. Vaid, W. Rodriguez, and R. Bashir, "Microfluidic cd4⁺ and cd8⁺ t lymphocyte counters for point-of-care hiv diagnostics using whole blood", *Science Translational Medicine*, vol. 5, no. 214, 214ra170–214ra170, 2013. DOI: 10.1126/scitranslmed.3006870. [Online]. Available: https://www.science.org/doi/abs/10.1126/scitranslmed.3006870.

[17] K. R. Balakrishnan, J. C. Whang, R. Hwang, J. H. Hack, L. A. Godley, and L. L. Sohn, "Node-Pore Sensing Enables Label-Free Surface-Marker Profiling of Single Cells", *Analytical Chemistry*, vol. 87, no. 5, pp. 2988–2995, Mar. 2015, ISSN: 0003-2700. DOI: 10.1021/ac504613b. [Online]. Available: https://pubs.acs.org/doi/full/10.1021/ac504613b.

[18] Y. Zhao, D. Chen, H. Li, Y. Luo, B. Deng, S.-B. Huang, T.-K. Chiu, M.-H. Wu, R. Long, H. Hu, J. Wang, and J. Chen, "A microfluidic system enabling continuous characterization of specific membrane capacitance and cytoplasm conductivity of single cells in suspension", *Biosensors and Bioelectronics*, vol. 43, pp. 304–307, 2013, ISSN: 0956-5663. DOI: 10.1016/j.bios.2012.12.035. [Online]. Available: https://www.sciencedirect.com/science/article/pii/S0956566312008913.

[19] Originally published in: Y. Zhao, D. Chen, H. Li, Y. Luo, B. Deng, S.-B. Huang, T.-K. Chiu, M.-H. Wu, R. Long, H. Hu, J. Wang, and J. Chen, "A microfluidic system enabling continuous characterization of specific membrane capacitance and cytoplasm conductivity of single cells in suspension", *Biosensors and Bioelectronics*, vol. 43, pp. 304–307, 2013, ISSN: 0956-5663. DOI: 10.1016/j.bios.2012.12.035. [Online]. Available: https://www.sciencedirect.com/science/article/pii/S0956566312008913, Copyright Elsevier (2012).

[20] J. Kim, S. Han, A. Lei, M. Miyano, J. Bloom, V. Srivastava, M. R. Stampfer, Z. J. Gartner, M. A. LaBarge, and L. L. Sohn, "Characterizing cellular mechanical phenotypes with mechano-node-pore sensing", *Microsystems & Nanoengineering Nanoengineering*, vol. 4, p. 17 091, Mar. 2018. [Online]. Available: http://dx.doi.org/10.1038/micronano.2017.91%20http://10.0.4.14/micronano.2017.91%20https://www.nature.com/articles/micronano201791%7B%5C#%7Dsupplementary-information.

[21] A. V. Jagtiani, J. Carletta, and J. Zhe, "A microfluidic multichannel resistive pulse sensor using frequency division multiplexing for high throughput counting of micro particles", *Journal of Micromechanics and Microengineering*, vol. 21, 6 2011. DOI: 10.1088/0960-1317/21/6/065004. [Online]. Available: http://iopscience.iop.org/0960-1317/21/6/065004.

[22] A. V. Jagtiani, J. Zhe, J. Hu, and J. Carletta, "Detection and counting of micro-scale particles and pollen using a multi-aperture coulter counter", *Measurement Science and Technology*, vol. 17, pp. 1706–1714, 7 Jul. 2006, ISSN: 13616501. DOI: 10.1088/0957-0233/17/7/008.

[23] J. Zhe, A. Jagtiani, P. Dutta, J. Hu, and J. Carletta, "A micromachined high throughput coulter counter for bioparticle detection and counting", *Journal of Micromechanics and Microengineering*, vol. 17, pp. 304–313, 2 Feb. 2007, ISSN: 09601317. DOI: 10.1088/0960-1317/17/2/017.

[24] K. R. Balakrishnan, G. Anwar, M. R. Chapman, T. Nguyen, A. Kesavaraju, and L. L. Sohn, "Node-pore sensing: a robust, high-dynamic range method for detecting biological species", *Lab on a Chip*, vol. 13, no. 7, p. 1302, 2013, ISSN: 1473-0197. DOI: 10.1039/c3lc41286e. [Online]. Available: http://xlink.rsc.org/?DOI=c3lc41286e.

[25] F. R. Rivest, A. P. Pechacek, R. Park, K. Goodman, N. Cho, M. Lustig, and L. L. Sohn, "Toward real-time cell detection and characterization using Barker-coded node-pore sensing (NPS)", in *microTAS 2015 Conference Proceedings*, Gyeongju, Korea: Chemical and Biological Microsystems Society, 2015, pp. 47–50. [Online]. Available: http://www.rsc.org/images/LOC/2015/PDFs/Papers/0047%7B%5C_%7D1C2-1.pdf.

[26] M. R. Kellman, F. R. Rivest, A. Pechacek, L. L. Sohn, and M. Lustig, "Node-pore coded coincidence correction: Coulter counters, code design, and sparse deconvolution", *IEEE Sensors Journal*, vol. 18, pp. 3068–3079, 8 Apr. 2018, ISSN: 1530437X. DOI: 10.1109/JSEN.2018.2805865.

[27] M. Javanmard and R. W. Davis, "Coded corrugated microfluidic sidewalls for code division multiplexing", *IEEE Sensors Journal*, vol. 13, pp. 1399–1400, 5 2013. DOI: 10.1109/JSEN.2013.2242396. [Online]. Available: http://ieeexplore.ieee.org/document/6417941/.

[28] L. L. Sohn, O. A. Saleh, G. R. Facer, A. J. Beavis, R. S. Allan, and D. A. Notterman, "Capacitance cytometry: Measuring biological cells one by one", *Proceedings of the National Academy of Sciences of the United States of America*, vol. 97, pp. 10 687–10 690, 20 Sep. 2000, ISSN: 00278424. DOI: 10.1073/PNAS.200361297.

[29] S. Gawad, L. Schild, and P. Renaud, "Micromachined impedance spectroscopy flow cytometer for cell analysis and particle sizing", *Lab on a Chip*, vol. 1, pp. 76–82, 1 Sep. 2001, ISSN: 14730197. DOI: 10.1039/B103933B.

[30] S. Gawad, K. Cheung, U. Seger, A. Bertsch, and P. Renaud, "Dielectric spectroscopy in a micromachined flow cytometer: Theoretical and practical considerations", *Lab on a Chip*, vol. 4, pp. 241–251, 3 2004, ISSN: 14730197. DOI: 10.1039/B313761A.

[31] X. Han, C. V. Berkel, J. Gwyer, L. Capretto, and H. Morgan, "Microfluidic lysis of human blood for leukocyte analysis using single cell impedance cytometry", *Analytical Chemistry*, vol. 84, pp. 1070–1075, 2 Jan. 2012, ISSN: 00032700. DOI: 10.1021/AC202700X.

[32] D. Holmes, D. Pettigrew, C. H. Reccius, J. D. Gwyer, C. V. Berkel, J. Holloway, D. E. Davies, and H. Morgan, "Leukocyte analysis and differentiation using high speed microfluidic single cell impedance cytometry", *Lab on a Chip*, vol. 9, pp. 2881–2889, 20 2009, ISSN: 14730189. DOI: 10.1039/B910053A.

[33] C. V. Berkel, J. D. Gwyer, S. Deane, N. Green, J. Holloway, V. Hollis, and H. Morgan, "Integrated systems for rapid point of care (poc) blood cell analysis", *Lab on a Chip*, vol. 11, pp. 1249–1255, 7 Apr. 2011, ISSN: 14730189. DOI: 10.1039/C0LC00587H.

[34] H. Song, Y. Wang, J. M. Rosano, B. Prabhakarpandian, C. Garson, K. Pant, and E. Lai, "A microfluidic impedance flow cytometer for identification of differentiation state of stem cells", *Lab on a Chip*, vol. 13, pp. 2300–2310, 12 Jun. 2013, ISSN: 14730189. DOI: 10.1039/C3LC41321G.

[35] E. Du, S. Ha, M. Diez-Silva, M. Dao, S. Suresh, and A. P. Chandrakasan, "Electric impedance microflow cytometry for characterization of cell disease states", *Lab Chip*, vol. 13, pp. 3903–3909, 19 2013. DOI: 10.1039/C3LC50540E. [Online]. Available: http://dx.doi.org/10.1039/C3LC50540E.

[36] C. Küttel, E. Nascimento, N. Demierre, T. Silva, T. Braschler, P. Renaud, and A. G. Oliva, "Label-free detection of babesia bovis infected red blood cells using impedance spectroscopy on a microfabricated flow cytometer", *Acta Tropica*, vol. 102, no. 1, pp. 63–68, 2007, ISSN: 0001-706X. DOI: 10.1016/j.actatropica.2007.03.002. [Online]. Available: https://www.sciencedirect.com/science/article/pii/S0001706X07000794.

[37] N. Haandbæk, S. C. Bürgel, F. Heer, and A. Hierlemann, "Characterization of subcellular morphology of single yeast cells using high frequency microfluidic impedance cytometer", *Lab on a Chip*, vol. 14, pp. 369–377, 2 Jan. 2014, ISSN: 14730189. DOI: 10.1039/C3LC50866H.

[38] N. Haandbæk, O. With, S. C. Bürgel, F. Heer, and A. Hierlemann, "Resonance-enhanced microfluidic impedance cytometer for detection of single bacteria", *Lab on a Chip*, vol. 14, pp. 3313–3324, 17 Sep. 2014, ISSN: 14730189. DOI: 10.1039/C4LC00576G.

[39] T. Sun, S. Gawad, C. Bernabini, N. G. Green, and H. Morgan, "Broadband single cell impedance spectroscopy using maximum length sequences: Theoretical analysis and practical considerations", *Measurement Science and Technology*, vol. 18, pp. 2859–2868, 9 Sep. 2007, ISSN: 13616501. DOI: 10.1088/0957-0233/18/9/015.

[40] W. D. Foulkes, I. E. Smith, and J. S. Reis-Filho, "Triple-negative breast cancer", *New England Journal of Medicine*, vol. 363, pp. 1938–1948, 20 Nov. 2010, ISSN: 0028-4793. DOI: 10.1056/NEJMRA1001389. [Online]. Available: http://www.nejm.org/doi/abs/10.1056/NEJMra1001389.

[41] C. A. Hudis and L. Gianni, "Triple-negative breast cancer: An unmet medical need", *The Oncologist*, vol. 16, pp. 1–11, S1 Jan. 2011, ISSN: 1083-7159. DOI: 10.1634/THEONCOLOGIST.2011-S1-01.

[42] M. Lekka, P. Paidler, D. Gil, J. Lekki, Z. Stachura, and A. Hrynkiewicz, "Elasticity of normal and cancerous human bladder cells studied by scanning force microscopy", *European Biohysics*, vol. 28, pp. 312–316, 1999.

[43] B. Lincoln, H. M. Erickson, S. Schinkinger, F. Wottawah, D. Mitchell, S. Ulvick, C. Bilby, and J. Guck, "Deformability-based flow cytometry", *Cytometry*, vol. 59A, no. 2, pp. 203–209, Jun. 2004, ISSN: 0196-4763. DOI: 10.1002/cyto.a.20050. [Online]. Available: http://doi.wiley.com/10.1002/cyto.a.20050.

[44] G. Binnig, C. F. Quate, and C. Gerber, "Atomic force microscope", *Physical Review Letters*, vol. 56, pp. 930–933, 9 1986, ISSN: 00319007. DOI: 10.1103/PHYSREVLETT.56.930.

[45] R. M. Hochmuth, "Micropipette aspiration of living cells", *Journal of Biomechanics*, vol. 33, no. 1, pp. 15–22, Jan. 2000, ISSN: 0021-9290. DOI: 10.1016/S0021-9290(99)00175-X. [Online]. Available: https://www.sciencedirect.com/science/article/pii/S002192909900175X?via%7B%5C%%7D3Dihub.

[46] J. Guck, S. Schinkinger, B. Lincoln, F. Wottawah, S. Ebert, M. Romeyke, D. Lenz, H. M. Erickson, R. Ananthakrishnan, D. Mitchell, J. Käs, S. Ulvick, and C. Bilby, "Optical Deformability as an Inherent Cell Marker for Testing Malignant Transformation and Metastatic Competence", *Biophysical Journal*, vol. 88, no. 5, pp. 3689–3698, May 2005, ISSN: 0006-3495. DOI: 10.1529/BIOPHYSJ.104.045476. [Online]. Available: https://www.sciencedirect.com/science/article/pii/S0006349505734172.

[47] E. M. Darling and D. D. Carlo, "High-throughput assessment of cellular mechanical properties", *Annual Review of Biomedical Engineering*, vol. 17, no. 1, pp. 35–62, Dec. 2015, PMID: 26194428, ISSN: 15454274. DOI: 10.1146/annurev-bioeng-071114-040545. [Online]. Available: https://doi.org/10.1146/annurev-bioeng-071114-040545.

[48] O. Otto, P. Rosendahl, A. Mietke, S. Golfier, C. Herold, D. Klaue, S. Girardo, S. Pagliara, A. Ekpenyong, A. Jacobi, M. Wobus, N. Töpfner, U. F. Keyser, J. Mansfeld, E. Fischer-Friedrich, and J. Guck, "Real-time deformability cytometry: On-the-fly cell mechanical phenotyping", *Nature Methods*, vol. 12, pp. 199–202, 3 Feb. 2015, ISSN: 15487105. DOI: 10.1038/NMETH.3281.

[49] T. Kolb, S. Albert, M. Haug, and G. Whyte, "Optofluidic rotation of living cells for single-cell tomography", *Journal of Biophotonics*, vol. 8, no. 3, pp. 239–246, Mar. 2015, ISSN: 1864063X. DOI: 10.1002/jbio.201300196. [Online]. Available: http://doi.wiley.com/10.1002/jbio.201300196.

[50] T. Imasaka, Y. Kawabata, T. Kaneta, and Y. Ishidzu, "Optical chromatography", *Analytical Chemistry*, vol. 67, pp. 1763–1765, 11 1995, ISSN: 15206882. DOI: 10.1021/AC00107A003.

[51] T. Kaneta, J. Makihara, and T. Imasaka, "An "optical channel": A technique for the evaluation of biological cell elasticity", *Analytical Chemistry*, vol. 73, pp. 5791–5795, 24 Dec. 2001, ISSN: 00032700. DOI: 10.1021/AC010441G.

[52] C. G. Hebert, S. Hart, T. A. Leski, A. Terray, and Q. Lu, "Label-free detection of bacillus anthracis spore uptake in macrophage cells using analytical optical force measurements", *Analytical Chemistry*, vol. 89, pp. 10 296–10 302, 19 Oct. 2017, ISSN: 15206882. DOI: 10.1021/ACS.ANALCHEM.7B01983.

[53] D. R. Gossett, H. T. K. Tse, S. A. Lee, Y. Ying, A. G. Lindgren, O. O. Yang, J. Rao, A. T. Clark, and D. Di Carlo, "Hydrodynamic stretching of single cells for large population mechanical phenotyping.", *Proceedings of the National Academy of Sciences of the United States of America*, vol. 109, no. 20, pp. 7630–5, May 2012, ISSN: 1091-6490. DOI: 10.1073/pnas.1200107109. [Online]. Available: http://www.ncbi.nlm.nih.gov/pubmed/22547795%20http://www.pubmedcentral.nih.gov/articlerender.fcgi?artid=PMC3356639.

[54] A. Mietke, O. Otto, S. Girardo, P. Rosendahl, A. Taubenberger, S. Golfier, E. Ulbricht, S. Aland, J. Guck, and E. Fischer-Friedrich, "Extracting cell stiffness from real-time deformability cytometry: Theory and experiment", *Biophysical Journal*, vol. 109, pp. 2023–2036, 10 Nov. 2015, ISSN: 15420086. DOI: 10.1016/J.BPJ.2015.09.006.

[55] M. Xavier, P. Rosendahl, M. Herbig, M. Kräter, D. Spencer, M. Bornhäuser, R. O. Oreffo, H. Morgan, J. Guck, and O. Otto, "Mechanical phenotyping of primary human skeletal stem cells in heterogeneous populations by real-time deformability cytometry", *Integrative Biology (United Kingdom)*, vol. 8, pp. 616–623, 5 May 2016, ISSN: 17579708. DOI: 10.1039/C5IB00304K.

[56] A. E. Ekpenyong, G. Whyte, K. Chalut, S. Pagliara, F. Lautenschläger, C. Fiddler, S. Paschke, U. F. Keyser, E. R. Chilvers, and J. Guck, "Viscoelastic properties of differentiating blood cells are fate- and function-dependent", *PLoS ONE*, vol. 7, 9 Sep. 2012, ISSN: 19326203. DOI: 10.1371/JOURNAL.PONE.0045237.

[57] C. S. Hourigan, R. P. Gale, N. J. Gormley, G. J. Ossenkoppele, and R. B. Walter, "Measurable residual disease testing in acute myeloid leukaemia", *Leukemia*, vol. 31, pp. 1482–1490, 7 Jul. 2017, ISSN: 14765551. DOI: 10.1038/LEU.2017.113.

[58] B. Li, A. Maslan, S. E. Kitayama, C. Pierce, A. M. Streets, and L. L. Sohn, "Mechanical phenotyping reveals unique biomechanical responses in retinoic acid-resistant acute promyelocytic leukemia", *iScience*, vol. 25, p. 103 772, 2 Feb. 2022, ISSN: 2589-0042. DOI: 10.1016/J.ISCI.2022.103772.

[59] Q. Li, G. Lee, C. Ong, and C. Lim, "AFM indentation study of breast cancer cells", *Biochemical and Biophysical Research Communications*, vol. 374, no. 4, pp. 609–613, Oct. 2008, ISSN: 0006-291X. DOI: 10.1016/J.BBRC.2008.07.078. [Online]. Available: https://www.sciencedirect.com/science/article/pii/S0006291X08013624?via%7B%5C%%7D3Dihub.

[60] V. Swaminathan, K. Mythreye, E. T. O'Brien, A. Berchuck, G. C. Blobe, and R. Superfine, "Mechanical stiffness grades metastatic potential in patient tumor cells and in cancer cell lines.", *Cancer research*, vol. 71, no. 15, pp. 5075–5080, Aug. 2011, ISSN: 1538-7445. DOI: 10.1158/0008-5472.CAN-11-0247. [Online]. Available: http://www.ncbi.nlm.nih.gov/pubmed/21642375%20http://www.pubmedcentral.nih.gov/articlerender.fcgi?artid=PMC3220953.

[61] J. Rother, H. Nöding, I. Mey, and A. Janshoff, "Atomic force microscopy-based microrheology reveals significant differences in the viscoelastic response between malign and benign cell lines", *Open Biology*, vol. 4, no. 5, p. 140 046, 2014. DOI: 10.1098/RSOB.140046. [Online]. Available: https://www.ncbi.nlm.nih.gov/pmc/articles/PMC4042852/.

[62] D. Wirtz, K. Konstantopoulos, and P. C. Searson, "The physics of cancer: the role of physical interactions and mechanical forces in metastasis.", *Nature reviews. Cancer*, vol. 11, no. 7, pp. 512–522, Jun. 2011, ISSN: 1474-1768. DOI: 10.1038/nrc3080. [Online]. Available: http://www.ncbi.nlm.nih.gov/pubmed/21701513%20http://www.pubmedcentral.nih.gov/articlerender.fcgi?artid=PMC3262453.

[63] M. E. Dokukin, N. V. Guz, and I. Sokolov, "Quantitative Study of the Elastic Modulus of Loosely Attached Cells in AFM Indentation Experiments", *Biophysical Journal*, vol. 104, no. 10, pp. 2123–2131, May 2013, ISSN: 0006-3495. DOI: 10.1016/J.BPJ.2013.04.019. [Online]. Available: https://www.sciencedirect.com/science/article/pii/S0006349513004499.

[64] L. M. Lee and A. P. Liu, "The Application of Micropipette Aspiration in Molecular Mechanics of Single Cells.", *Journal of nanotechnology in engineering and medicine*, vol. 5, no. 4, pp. 0 408 011–408 016, Nov. 2014, ISSN: 1949-2944. DOI: 10.1115/1.4029936. [Online]. Available: http://www.ncbi.nlm.nih.gov/pubmed/26155329%20http://www.pubmedcentral.nih.gov/articlerender.fcgi?artid=PMC4476029.

[65] S. Hinz, M. Miyano, L. L. Sohn, and M. A. LaBarge, *Unpublished data*, 2022.

[66] R. W. DeBlois and C. P. Bean, "Counting and Sizing of Submicron Particles by the Resistive Pulse Technique", *Review of Scientific Instruments*, vol. 41, no. 7, pp. 909–916, Jul. 1970, ISSN: 0034-6748. DOI: 10.1063/1.1684724. [Online]. Available: http://aip.scitation.org/doi/10.1063/1.1684724.

[67] O. A. Saleh and L. L. Sohn, "Quantitative sensing of nanoscale colloids using a microchip coulter counter", *Review of Scientific Instruments*, vol. 72, pp. 4449–4451, 12 Dec. 2001, ISSN: 00346748. DOI: 10.1063/1.1419224. [Online]. Available: http://aip.scitation.org/doi/10.1063/1.1419224.

[68] A. Lai, R. Rex, K. L. Cotner, A. Dong, M. Lustig, and L. L. Sohn, "Mechano-node-pore sensing: A rapid, label-free platform for multi-parameter single-cell viscoelastic measurements", *Journal of Visualized Experiments*, e64665, 190 Dec. 2022, ISSN: 1940-087X. DOI: 10.3791/64665. [Online]. Available: https://www.jove.com/64665.

[69] B. Li, M. Kellman, and T. Carey, *node-pore-sensing-public*, "MATLAB-based data collection and analysis scripts for Node-Pore Sensing devices", 2022. [Online]. Available: https://github.com/sohnlab/node-pore-sensing-public.

[70] Z. M. Zhang, S. Chen, and Y. Z. Liang, "Baseline correction using adaptive iteratively reweighted penalized least squares", *Analyst*, vol. 135, pp. 1138–1146, 5 Apr. 2010, ISSN: 1364-5528. DOI: 10.1039/B922045C. [Online]. Available: https://pubs.rsc.org/en/content/articlehtml/2010/an/b922045c%20https://pubs.rsc.org/en/content/articlelanding/2010/an/b922045c.

[71] B. Li, J. Kim, M. Kellman, and K. L. Cotner, *mechanoNPS_Li-et-al-2020*, "Public repository of MATLAB code used to analyze mechano-NPS data in Li et al, 2020", 2020. [Online]. Available: https://github.com/sohnlab/mechanoNPS_Li-et-al-2020.

[72] K. L. Cotner, B. Li, and A. Dong, *NPS-analysis-JOVE*, "Mechano-NPS data analysis for the JOVE protocol paper", 2022. [Online]. Available: https://github.com/sohnlab/NPS-analysis-JOVE.

[73] J. R. Landis and G. G. Koch, "The measurement of observer agreement for categorical data", *Biometrics*, vol. 33, p. 159, 1 Mar. 1977, ISSN: 0006341X. DOI: 10.2307/2529310.

[74] J. L. Fleiss and J. Cohen, "The equivalence of weighted kappa and the intraclass correlation coefficient as measures of reliability", *Educational and Psychological Measurement*, vol. 33, pp. 613–619, 3 1973, ISSN: 15523888. DOI: 10.1177/001316447303300309.

[75] J. Shah, *Fleiss kappa calculator & visualisation of video annotations*, version 1.1.0, Jul. 8, 2020. [Online]. Available: https://github.com/jenilshah990/FleissKappaCalculator/releases/tag/1.1.0.

[76] K. McGraw and S. Wong, "Forming inferences about some intraclass correlation coefficients", *Psychol Methods*, vol. 1, 1 1996.

[77] M. Kendall and B. Smith, "The problem of m rankings", *Ann Math Stat*, vol. 10, 3 1939.

[78] J. Kim, B. Li, O. J. Scheideler, Y. Kim, and L. L. Sohn, "Visco-node-pore sensing: A microfluidic rheology platform to characterize viscoelastic properties of epithelial cells", *iScience*, vol. 13, pp. 214–228, Mar. 2019, ISSN: 25890042. DOI: 10.1016/j.isci.2019.02.021.

[79] A. V. Jagtiani, J. Zhe, J. Hu, and J. Carletta, "Detection and counting of micro-scale particles and pollen using a multi-aperture coulter counter", *Measurement Science and Technology*, vol. 17, pp. 1706–1714, 2006, ISSN: 0957-0233. DOI: 10.1088/0957-0233/17/7/008. [Online]. Available: http://iopscience.iop.org/0957-0233/17/7/008%20http://stacks.iop.org/0957-0233/17/i=7/a=008.

[80] J. Zhe, A. Jagtiani, P. Dutta, J. Hu, and J. Carletta, "A micromachined high throughput coulter counter for bioparticle detection and counting", *Journal of Micromechanics and Microengineering*, vol. 17, pp. 304–313, 2 2007. DOI: 10.1088/0960-1317/17/2/017. [Online]. Available: http://www.mstf.wsu.edu/articles/pros_JMM2.pdf.

[81] R. Liu, N. Wang, F. Kamili, and A. F. Sarioglu, "Microfluidic codes: A scalable multiplexed electronic sensor for orthogonal detection of particles in microfluidic channels", *Lab on a Chip*, vol. 16, pp. 1350–1357, 2016. DOI: 10.1039/C6LC00209A. [Online]. Available: http://xlink.rsc.org/?DOI=C6LC00209A.

[82] R. Liu, W. Waheed, N. Wang, O. Civelekoglu, M. Boya, C.-H. Chu, and A. F. Sarioglu, "Design and modeling of electrode networks for code-division multiplexed resistive pulse sensing in microfluidic devices", *Lab on a Chip*, vol. 17, pp. 2650–2666, 2017, ISSN: 1473-0197. DOI: 10.1039/C7LC00545H. [Online]. Available: http://pubs.rsc.org/en/Content/ArticleLanding/2017/LC/C7LC00545H.

[83] R. Liu, N. Wang, N. Asmere, and A. Fatih Sarioglu, "Scaling Code-Multiplexed Electrode Networks for Distributed Coulter Detection in Microfluidics", *Biosensors and Bioelectronics*, Aug. 2018, ISSN: 0956-5663. DOI: 10.1016/J.BIOS.2018.07.075. [Online]. Available: https://www.sciencedirect.com/science/article/pii/S0956566318305852.

[84] R. Barker, *Group synchronizing of binary digital systems in communication theory*, editor Jackson, W, 1953.

[85] R. Gold, "Optimal binary sequences for spread spectrum multiplexing (corresp.)", *IEEE Transactions on Information Theory*, vol. 13, no. 4, pp. 619–621, 1967. DOI: 10.1109/TIT.1967.1054048.

[86] T. Kasami, *Weight distribution formula for some class of cyclic codes*, Apr. 1996. [Online]. Available: https://cir.nii.ac.jp/crid/1571417126015823488.

[87] E. Dinan and B. Jabbari, "Spreading codes for direct sequence cdma and wideband cdma cellular networks", *IEEE Communications Magazine*, vol. 36, no. 9, pp. 48–54, 1998. DOI: 10.1109/35.714616.

[88] W. Stallings, *Data & Computer Communications*. Delhi, India: Pearson Education, 2007.

[89] K. L. Cotner and A. Dong, *multichannel-NPS-analysis*, "Automatic data analysis for multichannel NPS based on matched-filter detection and successive interference cancellation", 2022. [Online]. Available: https://github.com/klcotner/multichannel-NPS-analysis.

[90] M. Kozminsky, O. J. Scheideler, B. Li, N. K. Liu, and L. L. Sohn, "Multiplexed dna-directed patterning of antibodies for applications in cell subpopulation analysis", *ACS Applied Materials and Interfaces*, vol. 13, pp. 46 421–46 430, 39 Oct. 2021, ISSN: 19448252. DOI: 10.1021/ACSAMI.1C15047. [Online]. Available: https://pubs.acs.org/doi/full/10.1021/acsami.1c15047.

[91] V. Satopää, J. Albrecht, D. Irwin, and B. Raghavan, "Finding a "kneedle" in a haystack: Detecting knee points in system behavior", in *2011 31st international conference on distributed computing systems workshops*, IEEE, 2011, pp. 166–171.

[92] J. P. Lewis, "Fast normalized cross-correlation", *Industrial Light & Magic*, 1995. [Online]. Available: http://scribblethink.org/Work/nvisionInterface/nip.pdf.

[93] R. M. Haralick and L. G. Shapiro, *Computer and Robot Vision*, 1st. Addison-Wesley Longman Publishing Co., Inc., 1992, vol. 2, pp. 316–317, ISBN: 0201569434.

[94] R. L. Siegel, K. D. Miller, and A. Jemal, "Cancer statistics, 2018", *CA: A Cancer Journal for Clinicians*, vol. 68, no. 1, pp. 7–30, Jan. 2018, ISSN: 00079235. DOI: 10.3322/caac.21442. [Online]. Available: http://doi.wiley.com/10.3322/caac.21442.

[95] American Cancer Society, "Breast Cancer Facts & Figures 2018", American Cancer Society, Inc., Atlanta, Tech. Rep., 2017. [Online]. Available: https://www.cancer.org/content/dam/cancer-org/research/cancer-facts-and-statistics/breast-cancer-facts-and-figures/breast-cancer-facts-and-figures-2017-2018.pdf.

[96] A. Noone, N. Howlader, M. Krapcho, D. Miller, A. Brest, M. Yu, J. Ruhl, Z. Tatalovich, A. Mariotto, D. Lewis, H. Chen, E. Feuer, and K. Cronin, *SEER Cancer Statistics Review, 1975-2015*, 2018. [Online]. Available: https://seer.cancer.gov/csr/1975%7B%5C_%7D2015/ (visited on 10/06/2018).

[97] C. J. Fabian, C. Zalles, S. Kamel, S. Zeiger, C. Simon, and B. F. Kimler, "Breast cytology and biomarkers obtained by random fine needle aspiration: Use in risk assessment and early chemoprevention trials", *Journal of Cellular Biochemistry*, vol. 67, no. SUPPL. 28/29, pp. 101–110, 1997, ISSN: 07302312. DOI: 10.1002/(SICI)1097-4644(1997)28/29+<101::AID-JCB11>3.0.CO;2-K.

[98] E. R. Sauter, E. Ross, M. Daly, A. Klein-Szanto, P. F. Engstrom, A. Sorling, J. Malick, and H. Ehya, "Nipple aspirate fluid: a promising non-invasive method to identify cellular markers of breast cancer risk.", *British Journal of Cancer*, vol. 76, no. 4, pp. 494–501, 1997. [Online]. Available: http://www.ncbi.nlm.nih.gov/pubmed/9275027.

[99] S. Mansoor, C. Ip, and P. C. Stomper, "Yield of Terminal Duct Lobule Units in Normal Breast Stereotactic Core Biopsy Specimens: Implications for Biomarker Studies", *The Breast Journal*, vol. 6, no. 4, pp. 220–224, Jul. 2000. DOI: 10.1046/j.1524-4741.2000.99043.x. [Online]. Available: http://doi.wiley.com/10.1046/j.1524-4741.2000.99043.x.

[100] C. J. Fabian and B. F. Kimler, "Incorporating Biomarkers in Studies of Chemoprevention", in *Novel Biomarkers in the Continuum of Breast Cancer*, Springer, Cham, 2016, pp. 69–94. DOI: 10.1007/978-3-319-22909-6_3. [Online]. Available: http://link.springer.com/10.1007/978-3-319-22909-6%7B%5C_%7D3.

[101] C. J. Fabian, B. F. Kimler, C. M. Zalles, J. R. Klemp, S. Kamel, S. Zeiger, and M. S. Mayo, "Short-Term Breast Cancer Prediction by Random Periareolar Fine-Needle Aspiration Cytology and the Gail Risk Model", *Journal of the National Cancer Institute*, vol. 92, no. 15, pp. 1217–1227, Aug. 2000, ISSN: 0027-8874. DOI: 10.1093/jnci/92.15.1217. [Online]. Available: https://academic.oup.com/jnci/article-lookup/doi/10.1093/jnci/92.15.1217.

[102] A. Hoffman, R. Pellenberg, C. I. Drendall, and V. Seewaldt, "Comparison of Random Periareolar Fine Needle Aspirate versus Ductal Lavage for Risk Assessment and Prevention of Breast Cancer", *Current Breast Cancer Reports*, vol. 4, no. 3, pp. 180–187, Jun. 2012, ISSN: 1943-4588. DOI: 10.1007/s12609-012-0081-9. [Online]. Available: http://www.ncbi.nlm.nih.gov/pubmed/22924092%20http://www.pubmedcentral.nih.gov/articlerender.fcgi?artid=PMC3410022.

[103] H. Chai and R. E. Brown, "Field effect in cancer-an update.", *Annals of clinical and laboratory science*, vol. 39, no. 4, pp. 331–7, Sep. 2009, ISSN: 1550-8080. [Online]. Available: http://www.ncbi.nlm.nih.gov/pubmed/19880759.

[104] C. Ibarra-Drendall, L. G. Wilke, C. Zalles, V. Scott, L. E. Archer, S. Lem, L. D. Yee, J. Lester, S. Kulkarni, C. Murekeyisoni, M. Wood, K. Wilson, J. Garber, C. Gentry, A. Stouder, G. Broadwater, J. C. Baker, S. N. Vasilatos, E. Owens, S. Rabiner, A. C. Barron, and V. L. Seewaldt, "Reproducibility of Random Periareolar Fine Needle Aspiration in a Multi-Institutional Cancer and Leukemia Group B (CALGB) Cross-Sectional Study", *Cancer Epidemiology, Biomarkers, & Prevention*, vol. 18, no. 5, pp. 1379–1385, May 2009, ISSN: 1055-9965. DOI: 10.1158/1055-9965.EPI-08-1210. [Online]. Available: http://www.ncbi.nlm.nih.gov/pubmed/19383884%20http://www.pubmedcentral.nih.gov/articlerender.fcgi?artid=PMC3640981%20http://cebp.aacrjournals.org/cgi/doi/10.1158/1055-9965.EPI-08-1210.

[105] S. Masood, "Cytomorphology of Fibrocystic Change, High-Risk, and Premalignant Breast Lesions", *The Breast Journal*, vol. 1, no. 4, pp. 210–221, 1995. DOI: 10.1111/j.1524-4741.1995.tb00242.x. [Online]. Available: https://onlinelibrary.wiley.com/doi/abs/10.1111/j.1524-4741.1995.tb00242.x.

[106] B. M. Ljung, A. Drejet, N. Chiampi, J. Jeffrey, W. H. Goodson, K. Chew, D. H. Moore, and T. R. Miller, "Diagnostic accuracy of fine-needle aspiration biopsy is determined by physician training in sampling technique", *Cancer*, vol. 93, no. 4, pp. 263–268, 2001, ISSN: 0008543X. DOI: 10.1002/cncr.9040.

[107] J. A. Ledbetter, C. H. June, L. S. Grosmaire, and P. S. Rabinovitch, "Crosslinking of surface antigens causes mobilization of intracellular ionized calcium in T lymphocytes.", *Proceedings of the National Academy of Sciences of the United States of America*, vol. 84, no. 5, pp. 1384–8, Mar. 1987, ISSN: 0027-8424. [Online]. Available: http://www.ncbi.nlm.nih.gov/pubmed/3103134%20http://www.pubmedcentral.nih.gov/articlerender.fcgi?artid=PMC304434.

[108] V. Lulevich, Y.-P. Shih, S. H. Lo, and G.-Y. Liu, "Cell tracing dyes significantly change single cell mechanics.", *The journal of physical chemistry. B*, vol. 113, no. 18, pp. 6511–9, May 2009, ISSN: 1520-6106. DOI: 10.1021/jp8103358. [Online]. Available: http://www.ncbi.nlm.nih.gov/pubmed/19366241%20http://www.pubmedcentral.nih.gov/articlerender.fcgi?artid=PMC2698996.

[109] S. L. Fanning, T. C. George, D. Feng, S. B. Feldman, N. J. Megjugorac, A. G. Izaguirre, and P. Fitzgerald-Bocarsly, "Receptor cross-linking on human plasmacytoid dendritic cells leads to the regulation of IFN-alpha production.", *Journal of immunology*, vol. 177, no. 9, pp. 5829–39, Nov. 2006, ISSN: 0022-1767. [Online]. Available: http://www.ncbi.nlm.nih.gov/pubmed/17056507.

[110] E. M. Llufrio, L. Wang, F. J. Naser, and G. J. Patti, "Sorting cells alters their redox state and cellular metabolome", *Redox Biology*, vol. 16, pp. 381–387, Jun. 2018, ISSN: 2213-2317. DOI: 10.1016/J.REDOX.2018.03.004. [Online]. Available: https://www.sciencedirect.com/science/article/pii/S2213231718301058.

[111] N. Beliakova-Bethell, M. Massanella, C. White, S. Lada, P. Du, F. Vaida, J. Blanco, C. A. Spina, and C. H. Woelk, "The effect of cell subset isolation method on gene expression in leukocytes.", *Cytometry. Part A : the journal of the International Society for Analytical Cytology*, vol. 85, no. 1, pp. 94–104, Jan. 2014, ISSN: 1552-4930. DOI: 10.1002/cyto.a.22352. [Online]. Available: http://www.ncbi.nlm.nih.gov/pubmed/24115734%20http://www.pubmedcentral.nih.gov/articlerender.fcgi?artid=PMC3975050.

[112] C. R. White and J. A. Frangos, "The shear stress of it all: the cell membrane and mechanochemical transduction.", *Philosophical transactions of the Royal Society of London. Series B, Biological sciences*, vol. 362, no. 1484, pp. 1459–67, Aug. 2007, ISSN: 0962-8436. DOI: 10.1098/rstb.2007.2128. [Online]. Available: http://www.ncbi.nlm.nih.gov/pubmed/17569643%20http://www.pubmedcentral.nih.gov/articlerender.fcgi?artid=PMC2440408.

[113] S. Varma and J. Voldman, "A cell-based sensor of fluid shear stress for microfluidics.", *Lab on a chip*, vol. 15, no. 6, pp. 1563–73, Mar. 2015, ISSN: 1473-0189. DOI: 10.1039/c4lc01369g. [Online]. Available: http://www.ncbi.nlm.nih.gov/pubmed/25648195%20http://www.pubmedcentral.nih.gov/articlerender.fcgi?artid=PMC4443851.

[114] E. W. Flitney, E. R. Kuczmarski, S. A. Adam, and R. D. Goldman, "Insights into the mechanical properties of epithelial cells: the effects of shear stress on the assembly and remodeling of keratin intermediate filaments.", *The Journal of the Federation of American Societies for Experimental Biology*, vol. 23, no. 7, pp. 2110–2119, 2009. DOI: 10.1096/fj.08-124453. [Online]. Available: http://www.ncbi.nlm.nih.gov/pubmed/19246484%20http://www.ncbi.nlm.nih.gov/pubmed/19246484.

[115] J. Shaw Bagnall, S. Byun, S. Begum, D. T. Miyamoto, V. C. Hecht, S. Maheswaran, S. L. Stott, M. Toner, R. O. Hynes, and S. R. Manalis, "Deformability of Tumor Cells versus Blood Cells", *Scientific Reports*, vol. 5, Dec. 2015, ISSN: 2045-2322. DOI: 10.1038/srep18542. [Online]. Available: http://www.nature.com/articles/srep18542%20http://dx.doi.org/10.1038/srep18542%20http://10.0.4.14/srep18542%20http://dharmasastra.live.cf.private.springer.com/articles/srep18542%7B%5C#%7Dsupplementary-information.

[116] S. Byun, S. Son, D. Amodei, N. Cermak, J. Shaw, J. H. Kang, V. C. Hecht, M. M. Winslow, T. Jacks, P. Mallick, and S. R. Manalis, "Characterizing deformability and surface friction of cancer cells", *Proceedings of the National Academy of Sciences of the United States of America*, vol. 110, no. 19, pp. 7580–7585, 2013. DOI: 10.1073/pnas.1218806110. [Online]. Available: http://www.ncbi.nlm.nih.gov/pubmed/23610435.

[117] O. J. Scheideler, C. Yang, M. Kozminsky, K. I. Mosher, R. Falcón-Banchs, E. C. Ciminelli, A. W. Bremer, S. A. Chern, D. V. Schaffer, and L. L. Sohn, "Recapitulating complex biological signaling environments using a multiplexed, dna-patterning approach", *Science Advances*, vol. 6, eaay5696, 12 Mar. 2020, ISSN: 2375-2548. DOI: 10.1126/sciadv.aay5696. [Online]. Available: https://advances.sciencemag.org/lookup/doi/10.1126/sciadv.aay5696.

[118] S. Chen, A. W. Bremer, O. J. Scheideler, Y. S. Na, M. E. Todhunter, S. Hsiao, P. R. Bomdica, M. M. Maharbiz, Z. J. Gartner, and D. V. Schaffer, "Interrogating cellular fate decisions with high-throughput arrays of multiplexed cellular communities", *Nature Communications*, vol. 7, p. 10 309, Jan. 2016, ISSN: 2041-1723. DOI: 10.1038/ncomms10309. [Online]. Available: http://www.nature.com/doifinder/10.1038/ncomms10309.

[119] H. Gong, I. Holcomb, A. Ooi, X. Wang, D. Majonis, M. A. Unger, and R. Ramakrishnan, "Simple Method To Prepare Oligonucleotide-Conjugated Antibodies and Its Application in Multiplex Protein Detection in Single Cells", *Bioconjugate Chemistry*, vol. 27, no. 1, pp. 217–225, Jan. 2016, ISSN: 1043-1802. DOI: 10.1021/acs.

bioconjchem.5b00613. [Online]. Available: http://pubs.acs.org/doi/10.1021/acs.bioconjchem.5b00613.

[120] AlphaThera, *oYo-Link DBCO*. [Online]. Available: https://alphathera.com/click-chemistry/p/dbco (visited on 04/25/2022).

[121] L. R. Huang, E. C. Cox, R. H. Austin, and J. C. Sturm, "Continuous particle separation through deterministic lateral displacement", *Science*, vol. 304, pp. 987–990, 5673 May 2004, ISSN: 00368075. DOI: 10.1126/SCIENCE.1094567/SUPPL_FILE/HUANG.SOM.PDF. [Online]. Available: https://www.science.org/doi/10.1126/science.1094567.